Abstract:

Liu, Dong. Numerical simulation of UV disinfection reactors: impact of fluence rate distribution and turbulence modeling. (Under the direction of Joel. J. Ducoste.)

This study investigated two most important parts for numerical simulation of UV disinfection reactors: fluence rate distribution and turbulence modeling. In the first part, the evaluation of alternative fluence rate distribution models, including Multiple Point Source Summation (MPSS), Multiple Segment Source Summation (MSSS), Line Source Integration (LSI), Modified LSI (RAD-LSI), Discrete Ordinate (DO) and View Factor models, has been performed. As part of the evaluation, a complete MSSS model, which accounts for the quartz sleeve thickness while calculating refraction angles, was developed. In addition, a simple attenuation factor approach was introduced to integrate the physics of reflection, refraction, and absorption effects into the LSI model. In the second part, six turbulence models, including standard k-ε, k-ε RNG, k-ω(88), revised k-ω (98), Reynolds Stress Transport (RST), and Two-Fluid (TF), were investigated and applied to the flow field simulation of a closed conduit polychromatic UV reactor. Predicted flow field, kinetic turbulence energy, and turbulence energy dissipation rate were compared with the experimental data from a Particle Image Velocimetry (PIV) analysis at four locations close to the UV lamps. All of the predicted flow fields were combined with a MSSS fluence rate model and three different microbial inactivation kinetic models to simulate the disinfection process at two UV lamp power conditions. Microbial transport was simulated using the Lagrangian based particle tracking method. As part of the turbulence model analysis, the fluence distribution and the effluent microbial inactivation predicted by all turbulence models were reported.

In the fluence rate distribution study, the results showed that models, neglecting the effects of refraction, deviated significantly from the experimental data. In addition, the MSSS approach or models that incorporated the MSSS concept were found to agree well with the experimentally measured fluence rate distribution. Moreover, little difference was found between the results of the MSSS model with quartz sleeve thickness and UVCalc3D, which does not model the quartz sleeve thickness in the refraction angle calculation but uses a factor to account for the effects of the quartz sleeve on the fluence rate. The attenuation factor combined with LSI model was found to match the MSSS model predictions, while reducing the computational cost. In the turbulence model study, the results show that the fluence distributions and the effluent inactivation level were sensitive to the turbulence model selection. The level of sensitivity was a function of the operating conditions and the UV response kinetics of the microorganisms. In addition, the results show that operating conditions that produce higher log inactivation or microorganisms with higher sensitivity to UV will show greater sensitivity to the turbulence model selection. Further more, a broader fluence distribution was found with turbulence models that predicted a larger wake region behind the lamps and greater turbulent mixing characteristics. Overall, the results of this study suggest that numerical simulations of UV processes using CFD should be initially validated with experimental bioassay tests prior to its use as a tool for understanding and evaluating the UV disinfection performance for a specific reactor design and target microorganism.

NUMERICAL SIMULATION OF UV DISINFECTION REACTORS: IMPACT OF FLUENCE RATE DISTRIBUTION AND TURBULENCE MODELING

by

DONG LIU

A dissertation submitted to the Graduate Faculty of
North Carolina State University
In partial fulfillment of the
Requirements for the degree of
Doctor of Philosophy

Department of Civil, Construction, and Environmental Engineering

Raleigh, NC

2004

APPROVED BY:

Joel. J. Ducoste (committee chair) _____

Detlef Knappe _____

Francis de los Reyes III _____

David Ollis _____

Biography

Dong Liu was born at Chong Qing city in P. R. China. He took his undergraduate study at Tsinghua University in Beijing from Aug. 1993 to Jun. 1998 and received his Bachelor of Engineering degree in Hydraulic Engineering Department from Tsinghua University in 1998. From Aug. 1998 to Jun. 2001, he studied in the graduate school of Tsinghua University, and received his Master of Engineering degree in Hydraulic Engineering Department from Tsinghua University in 2001. From Aug. 2001 to Dec. 2004, he studied in Environmental Engineering Department at North Carolina State University for the Doctor of Philosophy and passed the final defense for his dissertation on Dec. 15. 2004.

Table of content

List of Figures

List of Tables

1. Background

Water treatment plants (WTP) are constantly being challenged to ensure appropriate levels of disinfection for the removal of pathogenic microorganisms while minimizing the prodution of disinfection by-products (DBP). The inefficacy of chlorine for inactivation of protozoan pathogens such as *Cryptosporidium* and *Giardia* and the production of harmful THMs have led WTPs to look for alternative disinfection methods. A promising alternative to chlorine is the utilization of ultraviolet (UV) irradiation, proven to photochemically inactivate microorganisms including *Cryptosporidium* and *Giardia*, without the production of DBPs.

Because different UV reactor design configurations can greatly impact the WTPs' level of disinfection as well as operation and maintenance cost, determining the optimum process and design parameters is especially significant. This becomes even more challenging when there are several design configuration options. Although conventional experimental bioassay tests could be done to evaluate the disinfection process, their expenses and convenience of implementation are always a concern for large scale UV systems. With the fast development of computer technology, numerical simulation, as an alternative to experimental method, is becoming a cost-effective approach for analyzing different design configurations. A robust UV disinfection process model that identifies how design variables and process control parameters can be adjusted as water quality changes, could greatly aid WTP professionals in consistently producing safe potable water.

Numerical models that simulate the disinfection process of UV system involve fluence rate models for UV light intensity distribution, turbulence models for flow field prediction, and microbial inactivation kinetic models to represent the fluence response of the target microorganisms. Among these models, fluence rate distribution and flow field simulation are the most challenging component of the UV numerical models. Their accurate calculation could greatly improve the final UV simulation results.

Over the last 20 years, several fluence rate models, including Line Source Integration (LSI), Multiple Points Source Summation (MPSS), Multiple Segment Source Summation (MSSS), UVCalc3D, View Factor, and Discrete Ordinate (DO), have been developed to calculate the light intensity distribution inside the UV system. These models are based on different physical representation of light and take into account different optical characteristics such as reflection, refraction, and absorption. While there are several potential methods for modeling the fluence rate distribution, no prior study has performed a detailed side-by-side evaluation of these models. One of the objectives of this research is to perform a detail evaluation of these models. All UV models will be compared with experimental measurements of the fluence rate distribution at different distances from the UV lamp surface. The current commercially available MSSS approach (UVCal3D) does not include refraction effects in the computation of the path length through the quartz sleeve. As part of this research, a complete MSSS model that includes reflection and refraction effects at the air/quartz/water interfaces and the absorption effects within the quartz sleeve and water will be developed. In addition, a new approach utilizing an

attenuation factor will be developed to reduce the computational cost of the MPSS or MSSS based approach. This attenuation factor will also help improve the performance of some models, such as the LSI and View Factor, which were originally designed to predict the fluence rate in the absence of reflection, refraction, and absorption effects.

Turbulence models are used as closure relationships to solve the Reynolds averaged Navier-Stokes differential equations that describe the mass and momentum transport in turbulent flow fields. A sensitivity analysis done by Buffle et al. (2000) showed that the choice of the appropriate turbulence model and boundary condition assumptions could severely impact the accuracy of the predicted results. However, Buffle (2000) only performed a limited evaluation of this parameter on the UV simulation performance. To date, no research has been performed that evaluates the sensitivity of the model selection while evaluating the accuracy of the turbulence on the simulated log inactivation and fluence distribution. In this study, six different turbulence models, including standard k-ε, RNG k-ε, k-ω(88), k-ω(98), Reynolds Stress Transport (RST), and Two-Fluid (TF) models, were used to predict the flow field inside a UV reactor. A commercially available Computational Fluid Dynamics (CFD) software Phoenics (CHAM) was used to numerically solve the differential equations of these turbulence models with the finite-volume technique. The modeling results were directly compared with experimental fluid mechanics measurement inside the UV reactor. In addition, to investigate the impact of the turbulence model selection on the simulation of the effluent inactivation and fluence distribution, all of the predicted flow fields were combined with

a Multiple Segment Source Summation (MSSS) based fluence rate model and three different microbial inactivation kinetic models to predict the disinfection process at two UV lamp power conditions. The Lagrangian particle tracking method was used to simulate the transport of microorganisms inside the UV reactors.

2. Fluence rate distribution simulation

2.1 Introduction

Characterizing the fluence rate from the lamp requires incorporating the principles of optics to the specific configuration of the reactor. Jacob and Dranoff (1970) developed the MPSS approach, which is based on dividing the linear lamp into a series of n equally-spaced point sources in an absorbing media. Blatchley (1997) introduced the LSI model in which the MPSS model is integrated over an infinite number of point sources, producing a closed form solution when the absorbance of the medium is zero. The LSI and MPSS models are mathematically identical in the limit as the number of point sources, n, approaches ∞. However, in the case of an absorbing media, the LSI model is inappropriate and deviates from the MPSS model with decreasing UV transmittance. In addition, neither Jacob and Dranoff nor Blatchley incorporated reflection and refraction effects, which take place at the air/quartz/water interfaces.

Bolton (2000) improved the MPSS approach by developing a full version that accounts for reflection, refraction as well as absorption effects. Bolton showed that when

the transmittance of water ($T_{10}^{'}$) is much larger than 70 percent, the error associated with neglecting refraction and reflection can be as large as 25 percent. Bolton further showed that the number of point sources should be greater than 1000 to produce an accurate representation of the lamp physics. As a result, the MPSS with refraction, reflection, and absorption can be computationally intensive, especially when the UV system consists of several lamps or when a medium-pressure mercury lamp is used since it emits a broad range of wavelengths in the germicidial 200-300 nm band.

Bolton (2002) further improved the MPSS model and introduced the MSSS method. The MSSS method incorporated much of the MPSS model including reflection, refraction, and absorption described in a previous article (Bolton, 2000). However, Bolton discovered that reflection, refraction, and absorption did not completely correct for the over-prediction caused by modeling a lamp with a series of linear point sources as one approaches the lamp surface. The MSSS approach corrected for this over-prediction by modeling the lamp as a series of differential cylindrical segments, where light is emitted normal to the cylinder surface and decreases with the cosine of the angle between the unit normal vector and the direction vector. Based on the MSSS method, Bolton developed a commercially available software for UV light intensity simulation, known as UVCalc3D. Bolton (2002) reduced the computational requirement of the MSSS approach in UVCalc3D by developing a look up table where the information for multiple lamps can be obtained from applying the MSSS approach for one lamp. However, UVCalc3D can still be computationally costly for multiple medium pressure lamps.

Another fluence rate distribution approach is the Discrete Ordinate (DO) method. DO is one of 5 methods for solving the radiative heat transfer equation that accounts for absorption and scattering effects when heat passes through a homogeneous and isotropic medium. Fiveland (1984) applied the DO approach to find numerical solutions in a two dimensional rectangular enclosure with a gray absorbing, emitting, and isotropically scattering medium. Stamnes et al. (1988) incorporated reflection, which takes place at the interface of the layers into the DO method. Liou et al. (1996) extended the DO method to the simulation of radiative transfer in a multi-layer medium with Fresnel interfaces, where the reflectivity is determined by Fresnel's equation. The model emphasized the importance of the angular dependence of reflectivity at the multi-layer interfaces and incorporated the effect of refraction.

Also based on heat transfer, the view factor method was originally presented by Hamilton and Morgan (1952) in order to calculate the radiative heat transfer between two surfaces. Hsu (1967) derived a closed-form solution of the view factor for the general case of two arbitrary parallel rectangles. Modest (1993) demonstrated the use of view factor algebra for heat transfer between two co-axial cylinder surfaces and between surfaces of different shapes. Kowalski et al. (2000) calculated the UV irradiation intensity distribution in a chamber filled with air by using Modest's view factor algebra and considered the reflection effect of the chamber wall. However, the method was never demonstrated for use in an absorbing media.

In evaluating fluence rate models, it is important that an appropriate experimental

method be used that can measure the fluence rate received at any point in space. Blatchley (1997) demonstrated an experimental method of measuring the UV fluence rate through a collimator, which allows the radiometer detector surface to be struck by photons normal to it. Recent research by Rahn (1997), Linden and Mofidi (1999), and Rahn et al. (2000) have demonstrated the application of spherical actinometry for the measurement of germicidal radiation from monochromatic (low pressure) and polychromatic (medium pressure) UV sources. Because spherical actinometers act as 360 degree sensors, picking up photons from all angles, the number of photons incident on each sphere will be recorded inclusive of reflected and refracted radiation. As such, the spherical actinometry would better represent the fluence rate exposed by microorganisms. In this study, spherical actinometric experiments were performed and used to validate the fluence rate predictions at specific coordinates within the UV reactor.

All models were applied in two testing lamp arrangements: one with air and one with water. Tests in water were performed at two UVT values: 77 and 88 percent. A detailed description of the fluence rate models as well as the experimental setup will be described in the following section.

2.2 Fluence rate distribution models

2.2.1 Optic laws

Before providing a detailed description of the fluence rate models, it is important to understand some principles of optics used in these models.

Refraction (Snell's Law):

Snell's Law provides the relationship between incident angle, refractive angle, and the refractive indices of two media. When the radiant energy passes through an interface of two media with different refractive indices (Figure 2.1), Snell's Law is described as:

$$n_1 \sin\theta_1 = n_2 \sin\theta_2 \qquad (2.1)$$

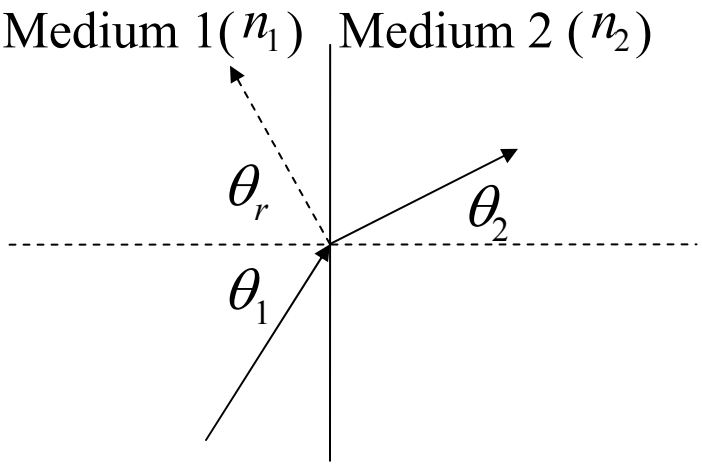

Figure 2.1 Refraction and reflection at the interface of two media with different refractive indices

Reflection (Fresnel's Law):

During the passage of radiant energy through an interface between two media of different refractive indices, a portion of the incident energy is reflected while the rest passes through the interface into the second medium (Figure 2.1). Based on the Fresnel Law (Meyer-Arendt, 1984), the Reflectance (R) for unpolarized incident energy is:

$$R = \frac{1}{2}\left[r_{II}^2 + r_{\perp}^2\right] \tag{2.2}$$

where, r_{II} is the amplitude of the radiant energy parallel to the plane of incidence and $r_{\perp}$ is the amplitude of radiant energy perpendicular to the plane of incidence. Fresnel Law define these two amplitudes as

$$r_{II} = \frac{n_2 \cos\theta_1 - n_1 \cos\theta_2}{n_1 \cos\theta_2 + n_2 \cos\theta_1} \tag{2.3a}$$

$$r_{\perp} = \frac{n_1 \cos\theta_1 - n_2 \cos\theta_2}{n_1 \cos\theta_1 + n_2 \cos\theta_2} \tag{2.3b}$$

Inverse Square Law:

At a distance r from a point source in a non-absorbing medium, the irradiance is given by the inverse square law as:

$$E = \frac{P}{4\pi r^2} \tag{2.4}$$

where, P is the radiant power emitted in all directions by the point source.

Absorption (Beer-Lambert Law):

The irradiance in an absorbing medium can be calculated as:

$$E = E_0 U \tag{2.5}$$

where E and E_0 are the irradiances with and without absorption, respectively, and U is the attenuation factor due to absorption. If $\alpha(\lambda)$ is the (napierian) absorption coefficient at wavelength λ, and l is the path length (cm), based on the Beer-Lambert law, the absorption attenuation factor U can be written as:

$$U = \exp[-\alpha(\lambda)l] \tag{2.6}$$

In Equation (2.6), $\alpha(\lambda)$ is related to the absorbance. For a given wavelength λ, $A(\lambda)$ is described as:

$$A(\lambda) = \frac{\alpha(\lambda)l}{\ln(10)} \tag{2.7}$$

The transmittance, $T(\lambda)$, over the path length, l, is defined by

$$T(\lambda) = 10^{-A(\lambda)} \tag{2.8}$$

In practice, the transmittance is often measured using a 10 mm path length, and is designated by the symbol $T_{10}^{'}$. From Equations 2.6 to 2.8, the relationship between attenuation factor U and the measured $T_{10}^{'}$ is computed as:

$$U = T_{10}^{'}(\lambda)^{\frac{l}{l_{10}}} \tag{2.9}$$

where $l_{10} = 10mm$.

2.2.2 MPSS model

Figure 2.2 is a schematic of a simplified UV disinfection reactor, consisting of a UV lamp inside a quartz sleeve mounted along the center line of the reactor. Although the models presented here are for a one lamp system, the fluence rates are spatially additive.

Therefore, multiple lamp UV systems can easily be developed based on the formulations provided for 1 lamp.

The MPSS approach is based on the assumption that the emission of a linear lamp is equivalent to that of n point sources spaced equally along the axis of the lamp. As shown in Figure 2.3 (a), point A is one of the n point sources of the lamp, and point B is exposed to the UV light that comes from point A and passes through the air/quartz/water interfaces. The power output for each point source is P/n, where P is the total UV power output of the lamp in the wavelength band of interest. The overall value of the fluence rate at point B is then the sum of the values of the fluence rate calculated for each of the n point sources.

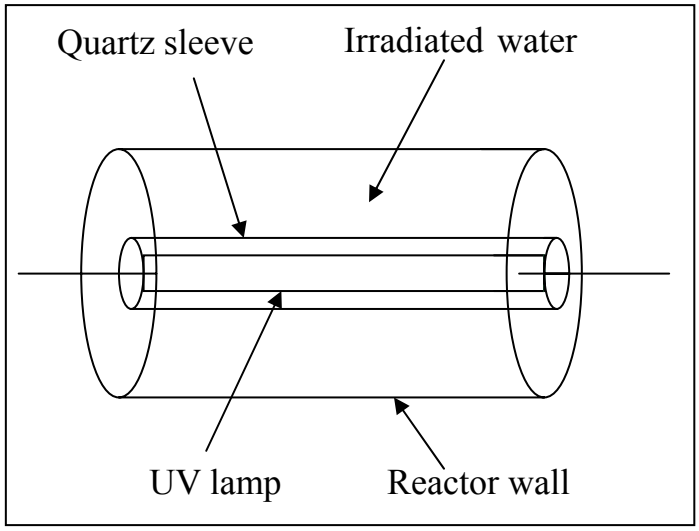

Figure 2.2. Schematic illustration of the UV disinfection system

Figure 2.3 (a) also illustrates the calculation of refraction angle for the fluence rate from point A to point B. h and r (Figure 2.3 (a)) are the longitudinal and normal distance from B to A, respectively. r_1 is the normal distance from the axis line of the lamp to the

inner surface of the quartz sleeve. r_2 is the thickness of the quartz sleeve, and r_3 is the perpendicular distance from point B to the outer surface of the quartz sleeve. $\theta_1, \theta_2,$ and θ_3 are the refraction angles in the air, quartz, water, respectively and $d_1, d_2,$ and d_3 are the path length of the UV light inside these media, respectively.

The three refraction angles are related by Snell's Law as:

$$\sin(\theta_1)n_a = \sin(\theta_2)n_q = \sin(\theta_3)n_w \quad (2.10)$$

where, $n_a, n_q,$ and n_w are the refractive indices of the air, quartz, water, respectively.

The refraction angles, r_i distances, and h, are related through the following equation:

$$\tan(\theta_1)r_1 + \tan(\theta_2)r_2 + \tan(\theta_3)r_3 = \mathrm{h} \quad (2.11)$$

Refraction angles $\theta_1, \theta_2,$ and θ_3 can be solved by combining Equations (2.10) and (2.11). The path lengths $d_1, d_2,$ and d_3, of UV light in the different media are related to the refraction angles by:

$$d_1 = r_1 / \cos(\theta_1) \quad (2.12a)$$

$$d_2 = r_2 / \cos(\theta_2) \quad (2.12b)$$

$$d_3 = r_3 / \cos(\theta_3) \quad (2.12c)$$

After considering reflection at the air/quartz/water interfaces and absorption through the different media, the calculation of fluence rate from point source A to point B can be written as:

$$I_A = (1 - R_1)(1 - R_2)\frac{P/n}{4\pi(d_1 + d_2 + d_3)^2} T_w^{d_3/0.01} T_q^{d_2/0.01} \ (\mathrm{W/m^2}) \quad (2.13)$$

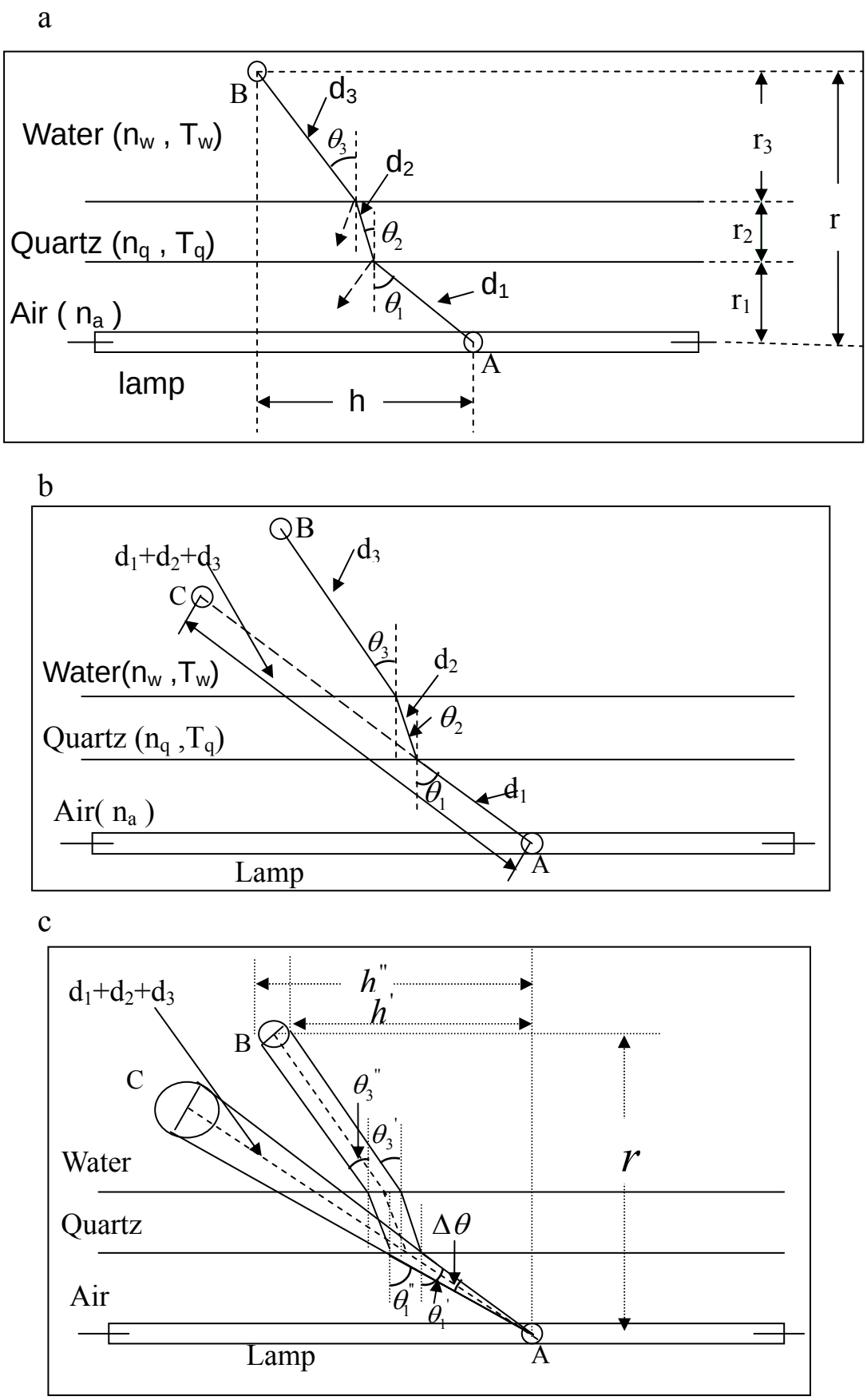

Figure 2.3. Components of refraction: a) refraction angle calculation, b) bending effect, c) focus effect

In Equation 2.13, R_1 and R_2 are the reflectance factors for the air/quartz and quartz/water interfaces, respectively, and can be derived from the Fresnel's Law (Equations 2.2 and 2.3). T_w and T_q are the 10 mm path length transmittance of the water and quartz, respectively. In Equation 2.13, the unit of the path length $d_1, d_2,$ and d_3 must be in meters. Equation (2.13) incorporates the bending effect for refraction, which is shown in Figure 2.3 (b). The refraction effect, taking place at the air/quartz/water interfaces, shifts point C to point B. Therefore, the bending effect changes the fluence rate spatial distribution significantly when compared to conditions without refraction.

In addition to the bending effect, another refraction component is the focus effect, which is illustrated in Figure 2.3 (c). The output power emitted from point A within the finite difference angle, $\Delta\theta$, would normally reach point C with a different cross-sectional area exposed to the UV light, when refraction is not considered. In other words, the focus effect of refraction concentrates the light power from a larger cross sectional area at point C to a smaller one at point B. In this research, we introduce a new parameter called the focus factor (*Focus*), which is used to represent the concentrating effect caused by refraction.

In Figure 2.3 (c), the dash lines represent the path of UV light coming from point A to point B and point C with and without refraction, respectively. The finite difference angle, $\Delta\theta$, is related to the refraction angle $\theta_1, \theta_2,$ and θ_3 by:

$$\theta_1 = \theta_1'' - \frac{\Delta\theta}{2} = \theta_1' + \frac{\Delta\theta}{2} \tag{2.14}$$

Based on cylindrical symmetry to the axis of the lamp, the focus factor can be obtained

by dividing the cross-sectional area of a circular segment between the finite difference angle ($\Delta\theta$) without refraction by the circular segment with refraction. For the case without refraction, the cross-sectional area of the circular segment is:

$$A_{wo} = 2\pi(d_1 + d_2 + d_3)^2 \Delta\theta \cos\theta_1 \tag{2.15}$$

The cross-sectional area with refraction can be expressed as:

$$A_w = 2\pi r(h'' - h') \cos\theta_3 \tag{2.16}$$

where, h'' and h' are given by Equations (2.10) and (2.11).

The focus factor is then calculated as:

$$Focus = \frac{A_{wo}}{A_w} = \frac{(d_1 + d_2 + d_3)^2 \Delta\theta \cos\theta_3}{r(h'' - h') \cos\theta_3} \tag{2.17}$$

The fluence rate at point B that arises from point source A taking into account reflection, absorption, as well as bending and focus effects of refraction is:

$$I_A = (1 - R_1)(1 - R_2) \frac{P/n}{4\pi(d_1 + d_2 + d_3)^2} T_w^{d_3/0.01} T_q^{d_2/0.01} Focus \ \ (\mathrm{W/m^2}) \tag{2.18}$$

2.2.3 MSSS model

The MSSS model incorporates much of the MPSS model including reflection, refraction, and absorption as described in Equation (2.18). In the MSSS approach, light is emitted normal to the cylinder surface and decreases with the cosine of the refraction angle θ_1. Based on the configuration shown in Figure 2.3, the MSSS fluence rate at point B caused by the UV light emitted from segment source A can be written as:

$$I_A = (1-R_1)(1-R_2)\frac{P/n}{4\pi(d_1+d_2+d_3)^2} T_w^{d_3/0.01} T_q^{d_2/0.01} Focus\cos\theta_1 \ (\mathrm{W/m^2}) \qquad (2.19)$$

Bolton (2002) has incorporated the MSSS approach into a commercially available software, known as UVCalc3D. The main difference between UVCalc3D and Equation (2.19) is the inclusion of the quartz sleeve in calculating the refraction effects and the corresponding change in the path length of light. UVCalc3D omitted the thickness of the quartz sleeve while calculating the refraction angles, and uses a simple factor to describe the effect of quartz sleeve on the fluence rate distribution. In this study, both Equation (2.19) and UVCalc3D were used to model the fluence rate distribution inside a test reactor filled with water to investigate the significance of the quartz sleeve in the refraction angle calculations.

2.2.4 LSI model

The LSI model is the continuous (integral) version of the MPSS model (Blatchley, 1997). The LSI and MPSS models are mathematically identical in the limit as the number of point sources, n approaches ∞. LSI is an efficient approach to the MPSS method in that a closed-form solution exist and that there is no need for a numerical routine. However, the closed form solution only exists in the absence of absorption, reflection, and refraction. The LSI fluence rate at a point with a normal distance, R, from the lamp and a longitudinal distance, H, from the center of the lamp with length, L, is given as:

$$I = \frac{P}{4\pi LR}\left[\arctan\left(\frac{L/2+H}{R}\right)+\arctan\left(\frac{L/2-H}{R}\right)\right] \qquad (2.20)$$

In this study, Equation (2.20) was used to model the fluence rate distribution inside a reactor filled with air, where absorption, reflection, and refraction can be omitted.

2.2.5 Attenuation factor approach

Although Equation (2.20) does not include absorption, reflection, and refraction effects, it is much simpler than the MPSS model and significantly less computationally intensive. Unfortunately, it was not designed to include the important physics of reflection, absorption, and refraction (i.e., bending and focus) of light. In this study, a simplified version of the MPSS was developed by multiplying Equation (2.20) with an attenuation factor. The attenuation factor was calculated by dividing an n points MPSS model (or MSSS model) that accounts for reflection, refraction, and absorption by an n points MPSS model without any of these effects. The use of the attenuation factor is shown in Equation 2.21 along with Equation 2.22:

$$I = \frac{P}{4\pi LR}\left[\arctan\left(\frac{L/2+H}{R}\right)+\arctan\left(\frac{L/2-H}{R}\right)\right]\times(\textit{atten factor}) \qquad (2.21)$$

where:

$$(atten\ factor)_{b,f} = \frac{\sum_{k=1}^{n}(1-R_{1,k})(1-R_{2,k})\dfrac{P/n}{4\pi(d_{1,k}+d_{2,k}+d_{3,k})^2}T_w^{d_{3,k}/0.01}T_q^{d_{2,k}/0.01}Focus_k}{\sum_{k=1}^{n}\dfrac{P/n}{4\pi(r_k^{\,2}+h_k^{\,2})}} \quad (2.22a)$$

$$(atten\ factor)_b = \frac{\sum_{k=1}^{n}(1-R_{1,k})(1-R_{2,k})\dfrac{P/n}{4\pi(d_{1,k}+d_{2,k}+d_{3,k})^2}T_w^{d_{3,k}/0.01}T_q^{d_{2,k}/0.01}}{\sum_{k=1}^{n}\dfrac{P/n}{4\pi(r_k^{\,2}+h_k^{\,2})}} \quad (2.22b)$$

$$(atten\ factor)_{b,f,c} = \frac{\sum_{k=1}^{n}(1-R_{1,k})(1-R_{2,k})\dfrac{P/n}{4\pi(d_{1,k}+d_{2,k}+d_{3,k})^2}T_w^{d_{3,k}/0.01}T_q^{d_{2,k}/0.01}Focus_k\cos\theta_{1,k}}{\sum_{k=1}^{n}\dfrac{P/n}{4\pi(r_k^{\,2}+h_k^{\,2})}} \quad (2.22c)$$

The variables used in the attenuation factor are shown in Figure 2.4. The ratio in Equation (2.22) describes the amount of light reduction due to reflection, refraction, and absorption. In Equation (2.22a), both the bending and focus effects of refraction are included. However, the numerator of the attenuation factor can be derived from Equation (2.13), which corresponds to the MPSS model without the focus effect of the refraction, and from Equation (2.19), which represents the MSSS model. Equations (2.22b) and (22c) are the calculations for attenuation factor that are based on these two methods.

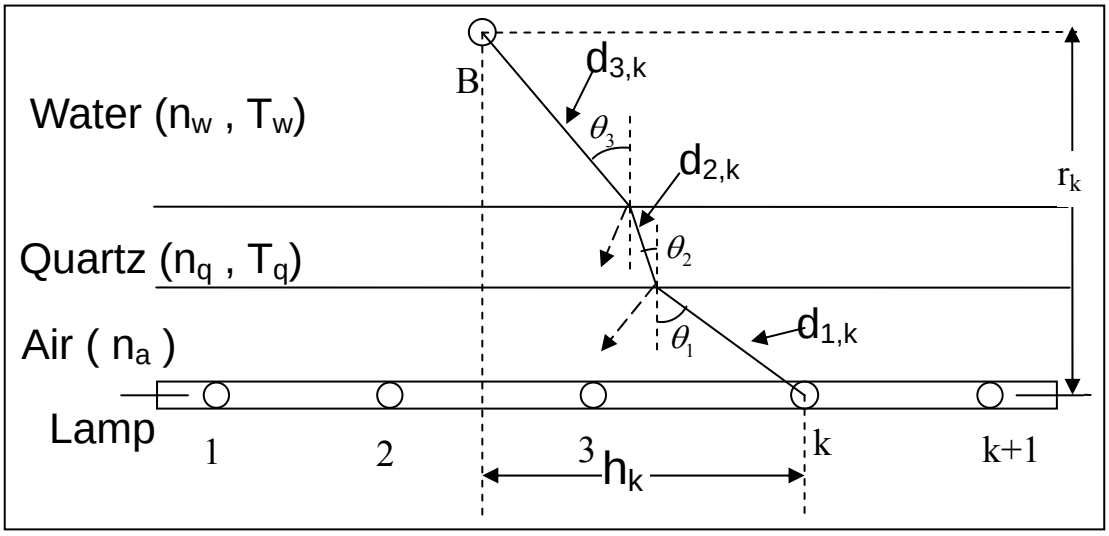

Figure 2.4. Illustration of the attenuation factor calculatio

Equation (2.22b) can be combined with fluence rate distribution models (i.e., RAD-LSI and View Factor) where the addition of the focus effect will incorrectly describe the longitudinal profiles near the quartz sleeve surface with these models. In this study, three values of n: 3, 5 and 10 were used to determine the resolution for the attenuation factor in Equation (2.22). The fluence rate computed using Equation (2.21) and (2.22c) using n=3,5,and 10 was compared with the full MSSS model, which used 1000 segment sources.

2.2.6 Modified LSI (RAD-LSI)

The closed-form of the LSI model has been shown to be effective for simulating far-field fluence rate distribution (Blatchley, 1997). However, the disagreement between the experimental measurements and model predictions will increase as the probe approaches the quartz sleeve surface. Since Bolton (2002) realized that a portion of the fluence rate was emitted in the radial direction for linear lamps, a model for the radial intensity calculation was incorporated into the LSI as a simple modification to account for the radial direction of the fluence rate as one approaches the lamp surface. Equation (2.23) displays the modified LSI, known as RAD-LSI.

$$I = \underbrace{\text{minimum}\left\{\frac{P}{2\pi LR}, \frac{P}{4\pi LR}\left[\arctan\left(\frac{L/2+H}{R}\right)+\arctan\left(\frac{L/2-H}{R}\right)\right]\right\}}_{\text{I}} * (\textit{atten factor})_b \quad (2.23)$$

(A: $\frac{P}{2\pi LR}$; B: $\frac{P}{4\pi LR}\left[\arctan\left(\frac{L/2+H}{R}\right)+\arctan\left(\frac{L/2-H}{R}\right)\right]$)

The first part of the minimum function in Equation (2.23) (I A) is the calculation for the fluence rate based on the radial intensity model. Part (I B) is the original LSI model. In order to include the absorption, reflection, and refraction effects, Equation (2.23) (part I A and B) was multiplied by the attenuation factor based on Equation (2.22b) (defined here as $(\textit{atten factor})_b$).

2.2.7 DO model

The DO (Discrete Ordinate) method is one of 5 numerical approaches for solving the

radiative transfer equation (Equation 2.24), which accounts for radiation in an absorbing and scattering media.

$$(\Omega \bullet \nabla) I(r,\Omega) = -(k_a + k_s) I(r,\Omega) + k_a I_b(r) + \frac{k_s}{4\pi} \int_{\Omega'=4\pi} I(r,\Omega') \phi(\Omega' \to \Omega) d\Omega' \quad (2.24)$$

I II III IV V

where, Ω - direction of propagation of radiation beam

k_a, k_s - absorption and scattering coefficients (1/m)

I_b - intensity of black body radiation

ϕ - scattering phase function

As shown in Equation (2.24), part I of the radiative transfer equation is the gradient of intensity along propagation direction, part II is the loss due to absorption, part III is the loss due to out-scattering, part IV is the gain due to black-body emission, and part V is the gain due to in-scattering. Although Equation (2.24) was originally proposed for the heat transfer in one medium, several researchers (Knut et al. 1988, Liou et al. 1996) have improved it to model radiative transfer in the multi-layer medium with fresnel interfaces. In this study, a commercially available computational fluid dynamics software, known as FLUENT (Lebanon, New Hampshire), which has a built-in version of the DO model to solve the radiative transfer equation, was used to predict the fluence rate distribution inside a reactor filled with water. FLUENT's version of the DO model did not include refraction effect of light.

2.2.8 View factor model

The view factor approach was primarily used to determine the radiant heat transfer between two arbitrarily sized parallel rectangles. Based on the idea of the view factor algebra, Modest (1993) developed a model to calculate the irradiance intensity from a cylindrical surface to a differential element in space. Kowalski et al. (2000) applied the view factor approach to simulate the light intensity field for the prediction of disinfection in air streams. The basic theory underlying the view factor approach is that a cylindrical lamp can be divided into two parts according to the location of the point of interest. For each lamp section, the view factor method predicts the fraction of radiation emitted from the surface of the lamp section that directly strikes a differential element. The intensity at any point is the product of the view factor and the surface intensity of the lamp. The surface intensity is simply the UV power output in watts divided by the surface area of the lamp. As illustrated in Figure 2.5, the view factor approach is calculated as:

$$F_i = \frac{L_i}{\pi H}\left[\frac{1}{L_i} ATAN\left(\frac{L_i}{\sqrt{H^2-1}}\right) + \frac{X_i - 2H}{\sqrt{X_i Y_i}} ATAN\left(\sqrt{\frac{X_i(H-1)}{Y_i(H+1)}}\right) - ATAN\left(\sqrt{\frac{H-1}{H+1}}\right)\right] \quad (2.25)$$

where, $H = x/r$, $L_i = l_i/r$

$X_i = (1+H)^2 + L_i^2$, $Y_i = (1-H)^2 + L_i^2$, $i = 1,2$

The light intensity is then determined by:

$$I = I'(F_1 + F_2) \quad (2.26)$$

In Equation (2.26), I' is the surface intensity of the lamp, and is calculated as:

$$I' = \frac{P}{2\pi r l} \tag{2.27}$$

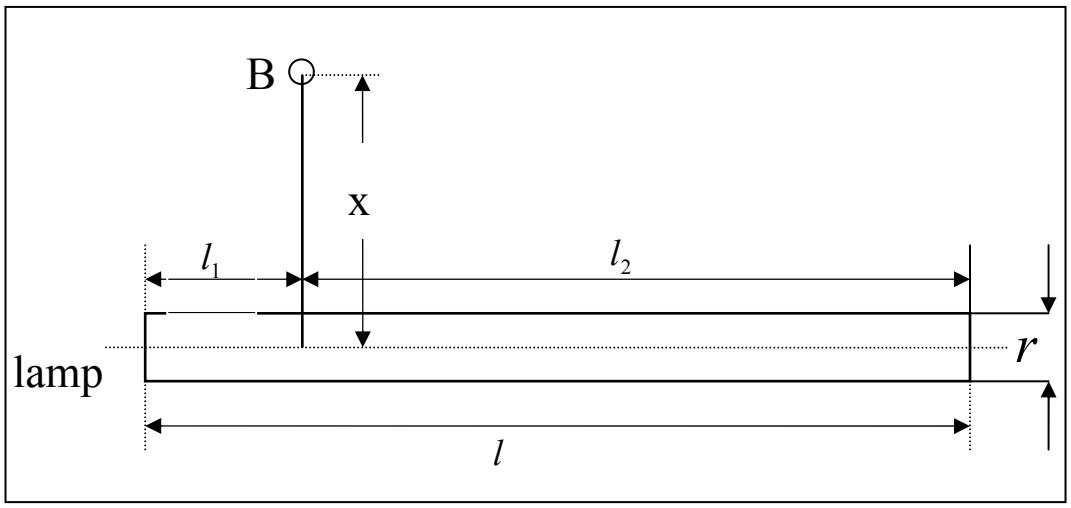

Figure 2.5. Illustration for view factor method

Equations (2.25)-(2.27) do not account for absorption, reflection, and refraction effects. These effects were included in the view factor approach by multiplying Equation (2.26) with Equation (2.22b) to simulate the fluence rate distribution inside a reactor filled with water. With the exception of the DO method and UVCalc3D, all other fluence rate models were incorporated in the computational fluid dynamics software, PHOENICS (CHAM, UK).

2.3 Experimental methods

Experimental validation of the mathematical models is an important part of evaluating different fluence rate distribution models. Spherical actinometry has been proposed recently as a novel technique for determining the UV fluence using spherical

quartz vessels containing a chemical actinometer (i.e., potassium iodide/potassium iodate (KI/KIO_3)) (Rahn et al.,2000). Within this setting, actinometers should be able to receive photons from all directions. The number of photons incident on each vessel will be recorded including reflected and refracted radiation, to approximate the photon energy received by an exposed microorganism at an identical position. Spherical actinometry has great advantages over the conventional radiometer measurement, which cannot pick up the radiation coming from all angles as with reflected light or light from multiple sources in a reactor (Rahn et al.,2000). This method was first used in solar UV radiation measurements (Sommer et al., 1999). It has also been applied in dosimetry measurements of room-air germicidal radiation (Rahn, 1999 and 2003, Rudnick, 2001). In these studies, it has been demonstrated that the spherical vessels can simultaneously measure the UV fluence at a number of points in space, subject to the combined output of an array of germicidal lamps positioned to disinfect the upper room air. The method has also been used in water disinfection UV system. Rahn et al. (2000) applied spherical actinometry to determine the fluence rate distribution in a single lamp low pressure UV reactor system and Stefan et al. (2001) used it in a single lamp medium pressure (MP) UV reactor system.

In this research, spherical actinometry measurements inside two testing reactors were performed to validate different mathematical models. A 0.1M KIO_3/0.6M KI in 0.01M $Na_2B_4O_7.10H_2O$ (Fisher scientific) solutions was freshly made as the KI/KIO_3 actinometer. Fluence rates [mW cm^{-2}] were calculated using the following equation

(Rahn, 1997):

$$\text{Fluence rate} = \frac{\Delta a_{352} V}{\Phi_{\lambda} \varepsilon A_{cs} t (1 - R)} \times U \qquad (2.28)$$

where:

Φ_{λ} = quantum yield for generation of I_3^- at average light emission.

$(0.64 \times [1 + 0.02 \times (T - 20.7)]$ moles/Einstein)

T = actinometer temperature during irradiation (°C)

Δa_{352} = change of absorption coefficient at 352nm (cm^{-1})

ε = molar absorption coefficient at 352 nm (26400 M^{-1} cm^{-1})

V = volume of irradiated actinometer solution (L)

A_{cs} = cross sectional area of the spherical vessels (cm^2)

U = constant used to convert einstein into conventional UV fluence units

(4.7153×10^8 mJ $einstein^{-1}$ for LP based on 253.7 nm emission)

t = UV exposure time (s)

R = reflection of quartz sleeve surface

Note that in the calculated fluence value, the molar absorption coefficient of 26,400 M^{-1} cm^{-1} was obtained from Rahn (1997). However, a recent study determined the molar absorption coefficient of I_3^- in the actinometer solution to be 27,636 M^{-1} cm^{-1} (Stefan et al., 2001). The differences in the data presented when evaluated using these two approaches results in a 5% overestimation using the Rahn (1997) values. In Equation 2.28, the reflection of light by the quartz is also included in the computation of the

experimental fluence rate. The reflection was calculated based on the approach developed by Bolton (2000). For this study, the reflection of light by the quartz vessel was calculated as 8.9% and 0.4% in air and water, respectively (Bolton, 2003). These tests were performed by researchers at Duke university (Professor Karl Linden, Department of Civil and Environmental Engineering)

2.4 Evaluation of fluence rate models

In this study, actinometry measurements and numerical simulation of the fluence rate inside two test reactors were performed to validate these different mathematical models. One reactor contained air with 100 percent transmissivity. The second reactor was filled with water with two transmissivity values: 78 percent and 88 percent. All numerical simulation results from different fluence rate models were compared with the spherical actinometry measurements.

2.4.1 Air test

2.4.1.1 Air test reactor configuration

Figure 2.6 displays the reactor configuration for tests conducted in air. Solutions of the potassium iodide/iodate (KI) actinometer (Rahn, 1997) were housed in spherical quartz containers and suspended parallel to a low pressure (LP) mercury UV lamp at three specific positions with radial distances of 5, 10, and 15 cm from the lamp. The arc length of the LP lamp used in this study was 28 cm and the total output power at 254 nm wavelength band was 16 watts with a measured UVC efficiency of 41 percent.

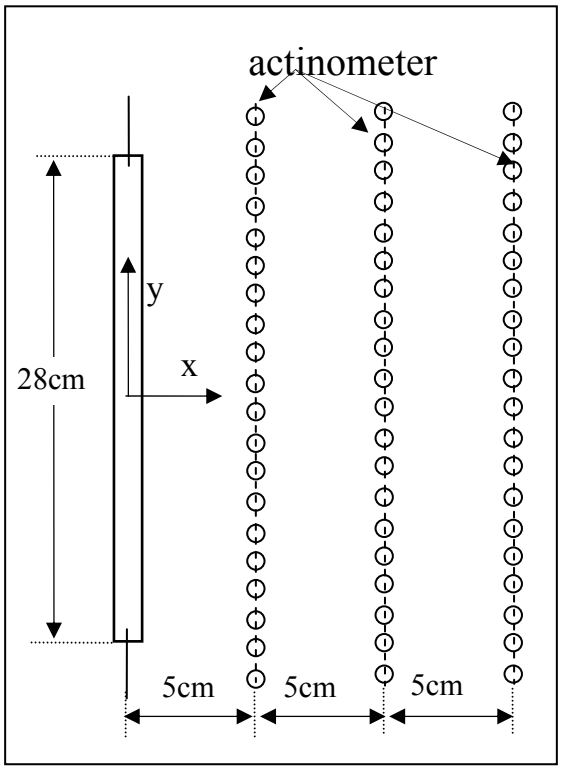

Figure 2.6. Schematic illustration of test reactor in the air

2.4.1.2 Air test results and analysis

Figure 2.7 and 2.8 display the fluence rate distribution in the air box. The error bar on KI/KIO_3 actinometer test data curve represents the experimental standard deviation.

In Figure 2.7 (a), the results show that the LSI model predicted a higher fluence rate than both the experimental measurements and UVCalc3D model at a radial distance of 5 cm. Far from the lamp (x = 10 and 15 cm), both of these mathematical models agreed well with the experimental data. Modifications made to the original LSI model, RAD-LSI, were found to improve the fluence rate distribution predictions at x = 5 cm (Figure 2.7 (b)), while maintaining the same level of accuracy far from the lamp. As discussed earlier,

the LSI model displays a higher fluence rate distribution in the region close to lamp center. This higher fluence rate is due to the point source assumption, which does not consider the cylindrical geometry of the UV lamp. The RADIAL portion of the RAD-LSI seems to provide a simple correction for the fluence rate around the lamp central region.

Figure 2.8 clearly shows the improvement of the RAD-LSI model as one approach the lamp surface. RAD-LSI selects either RADIAL model or LSI model to determine the fluence rate based on the location of the point of interest. Near the lamp surface, the RADIAL model predicts a lower fluence rate than the LSI model. However, near the lamp ends and at radial distances further from the lamp surface, the LSI model predicts a lower fluence rate than the RADIAL model. Unfortunately, the RAD-LSI still has problems predicting the fluence rate near the lamp ends due to the point source approximation of the LSI portion. UVCalc3D's ability to better predict experimental fluence rate results suggests that the cosine angle effect is important to characterizing the fluence rate near the lamp.

a

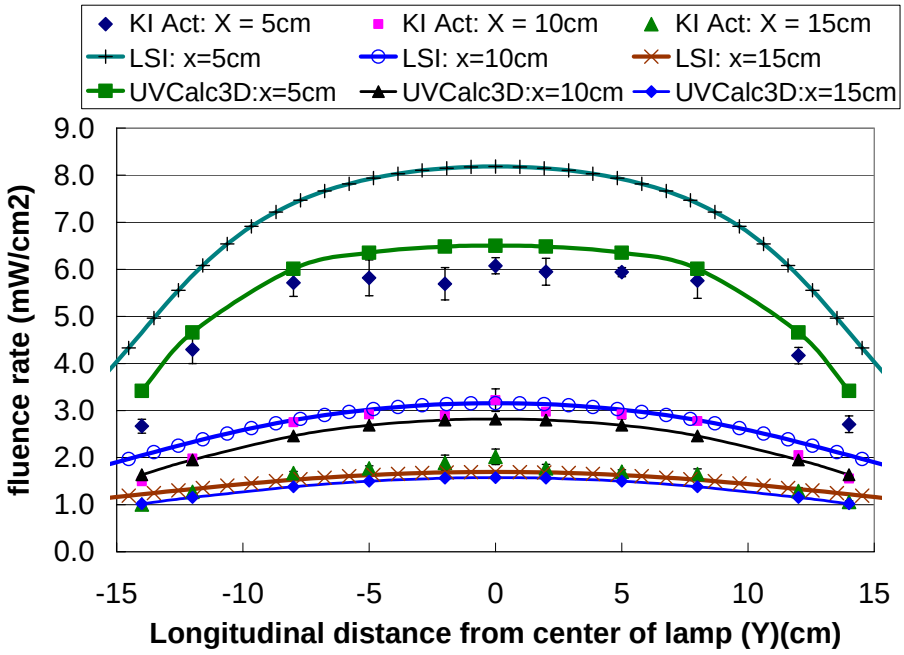

b

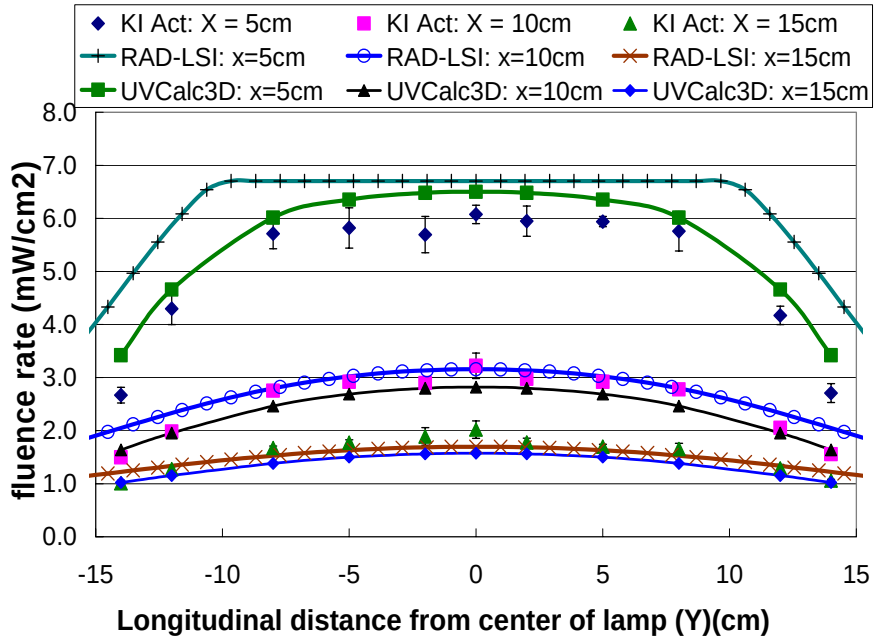

Figure 2.7. Fluence rate distribution along the lamp at different normal distance to the lamp (x=5, 10, 15 cm) a) Impact of LSI, b) Impact of RAD-LSI

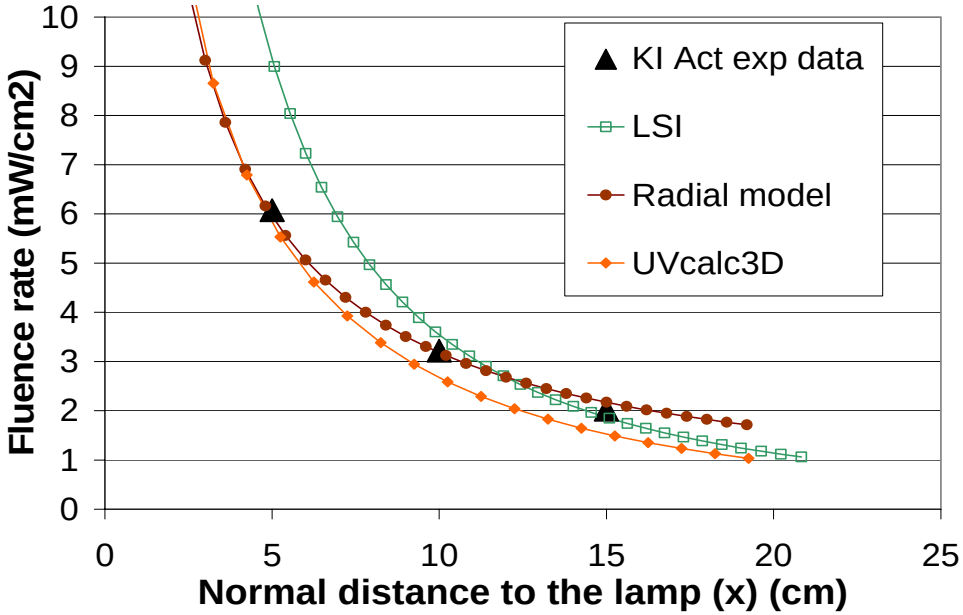

Figure 2.8. Fluence rate radial distribution on the profile of center point of the lamp

Although not reported in the figures, the view factor approach was found to produce similar results to RAD-LSI with the exception of near the lamp ends. In that region, the view factor model was closer to the experimental results but still above the UVCalc3D predictions. Overall, the fluence rate results in air suggest that the lamp is best approximated by using the MSSS concept.

2.4.2 Transmissivity test

2.4.2.1 Transmissivity test reactor configuration

Transmissivity tests were performed inside a reactor filled with water as shown in Figure 2.9. KI actinometer was housed in spherical quartz vessels and suspended at 18 locations in water with 77 and 88 percent UV Transmittance (UVT). A detailed description of these testing points is shown in Table 1. The center point of the reactor is

chosen as the origin of the coordinate system. X and Y axis are the directions perpendicular and parallel to the lamp, respectively.

Table 2.1 Actinometer measurement locations in the transmissivity test reactor

Vessel number	1	2	3	4	5	6	7	8	9
X (cm)	10.55	10.55	9.55	-11.55	-11.55	-11.55	7.35	7.15	6.95
Y (cm)	7.5	2.8	-4.8	8.5	3.8	-3.5	7.1	2.3	-5.4
Vessel number	10	11	12	13	14	15	16	17	18
X (cm)	-7.45	-7.45	-7.35	3.75	3.35	4.05	-4.35	-4.35	-4.05
Y (cm)	6.6	2.8	-4.7	7.6	2.0	-5.5	6.7	2.2	-5.3

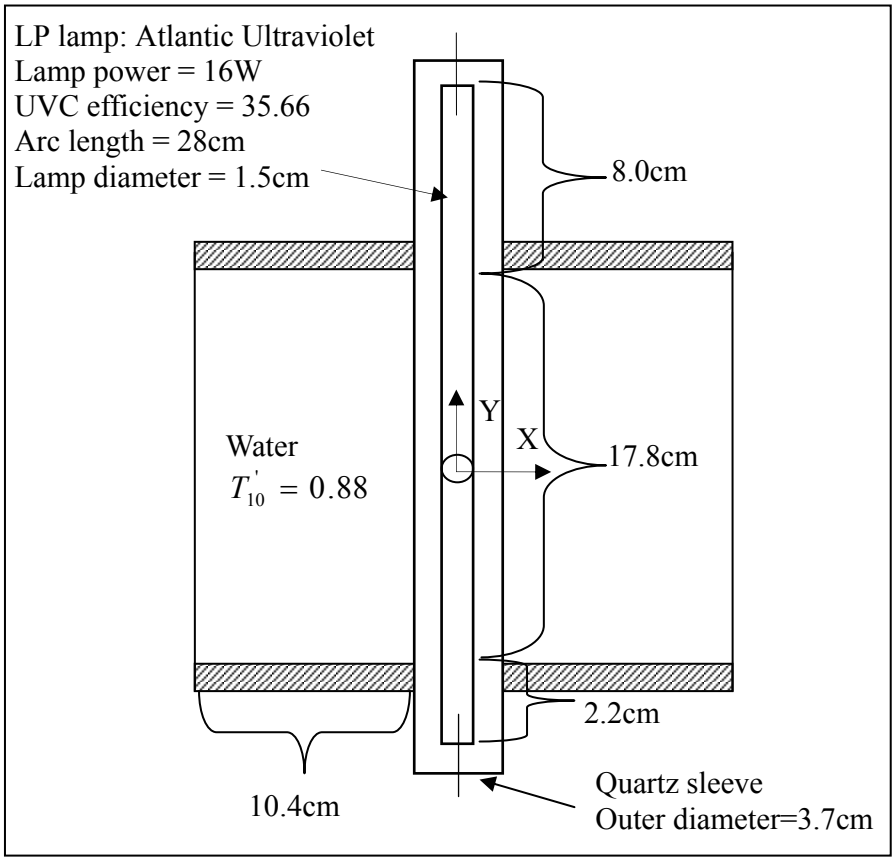

Figure 2.9 Reactor filled with water for transmissivity tests

2.4.2.2 Transmissivity test results and analysis

Figure 2.10 displays the predicted fluence rate distribution at the 18 measurement points in a reactor filled with water. The modeling results were compared with experimental measurements at 77 and 88 UVTs. However, only the 88 UVT results were displayed in the following figures since the trends seen at 88 UVT were also found at 77 UVT. The goodness of fit between the experimental and modeling results was computed as (Tarald 1985):

$$R^2 = 1 - \sum_{i=1}^{18} (I_i - \hat{I}_i)^2 / \sum_{i=1}^{18} (I_i - \bar{I})^2 \quad (2.29)$$

where, I_i represents the experimental results, $\bar{I}$ is the average value of I_i over all of the points, and $\hat{I}_i$ represents the model results. In Figure 2.10 (a), for test points (1-6) far from the lamp, the MSSS model, UVCalc3D as well as RAD-LSI were found to under-predict the experimental fluence rate and yield similar results. This under-prediction is due to the reflection effect of the glazed reactor wall. Since the points 1, 2, 4, 5, and 6 are very close to the wall (nearly 0.5 cm), irradiance reflected from the wall increased the experimental fluence rate value. However, the model simulations at point 3, which was further away from the wall than other points in this group, just slightly under predicted the experimental fluence rate. Therefore, it is reasonable to conclude that the difference between the predicted and experimental fluence rate in this group was predominantly caused by wall reflection.

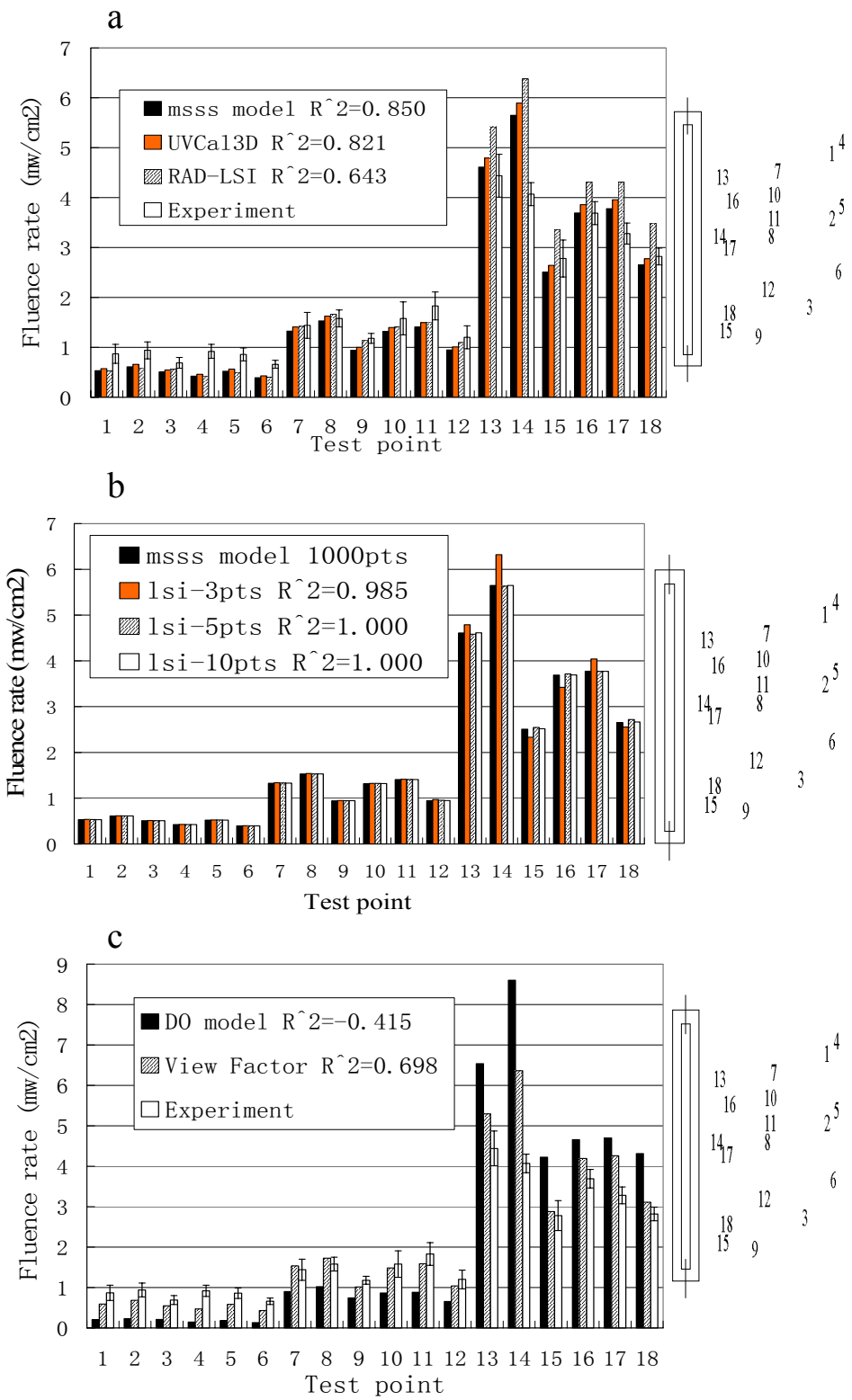

Figure 2.10. Fluence rate value in water at test points a) Comparison between UV Calc3D, RAD-LSI, and MSSS models, b) Determination of appropriate n value for attenuation factor, c) Comparison between DO and View Factor models

At the intermediate measurement points (test points 7-12, Figure 2.10 (a)), all three models exhibited reasonable agreement with the experimental data. In the region close to the lamp (points 13-18), the MSSS and UVCal3D fluence rate predictions were more accurate than RAD-LSI. The difference between calculated and measured results is quite large at test point 14 (Figure 2.10 (a)). However, considering the fluence rate value at point 13, which is located further from the lamp center and yields even higher UV light intensity than point 14 in the actinometer measurement, it is likely that the disagreement between numerical and experimental results was caused by the experimental error at point 14. The MSSS model differs with UVCalc3D only with the inclusion of the quartz sleeve thickness when calculating the refraction angle in the computation of the UV light path length. The results in Figure 2.10 (a) seem to suggest that the inclusion of the quartz sleeve thickness is insignificant and therefore can be approximated by a factor in any future modeling approach as computed in UVCalc3D.

Figure 2.9 (b) compares the MSSS model with the LSI model that incorporates the attenuation factor (Equation 2.22c) using 3, 5, and 10 points approximation. The goal in Figure 2.9 (b) was to determine the number of points needed in the attenuation factor calculation. Each n point approach was compared to the MSSS approach also using Equation 2.29. For this calculation, I_i represents MSSS model results and $\hat{I}_i$ represents the LSI model results using different n values for the attenuation factor. In Figure 2.10 (b) all three n values yield very high R^2 values suggesting that all three could be used to approximate the MSSS approach. Looking at regional differences, the results

show that the 3, 5, and 10 points attenuation factor yield identical results at locations far from the lamp. Near the lamp, the greatest deviation occurred between the 3 point approximation and the MSSS model. The results suggest that the five-points approximation method for attenuation factor calculation is a time efficient and accurate alternative to the MSSS model. As a result, the 5 point approximation was applied to other attenuation factor calculations used in this study.

Figure 2.10 (c) displays a comparison of the DO and VIEW FACTOR models with experimental results. In Figure 2.10 (c), the large difference between DO model and experimental data can be attributed to neglecting both bending and focus effects of refraction at air/quartz/water interfaces. As mentioned earlier, the commercial software, FLUENT, only accounts for absorption and scattering when solving the radiative transport equation (Equation 2.25). The inaccuracy of the DO model demonstrates the significance of refraction effect when dealing with water. Bolton (2000) showed that neglecting refraction will cause large errors for point source summation methods when UVT is greater than 70 percent. Although the DO model is based on a different method versus the point source summation method, ignoring refraction still resulted in large errors. As a result, refraction effects should be incorporated into the DO model in FLUENT to improve its performance. In Figure 2.10 (c), the view factor model combined with 5 points attenuation factor based on Equation (2.22b) predicted comparable results to the RAD-LSI, MSSS, and UVCalc3D. Like the DO model, the view factor model is not derived from the point source summation method. However, due to the introduction

of the attenuation factor, which covers reflection, refraction, and absorption effects, its result agreed well with the actinometer data compared to the DO model.

Figures 2.11 (a) through 2.11d display the longitudinal shape of different fluence rate distribution models along the lamp length at different radial distances (x = 3.35, 4.35, 7.35, 11.35 cm). The MSSS model was omitted from Figure 2.11 since the 5 points LSI model produced results identical with the MSSS approach. In Figure 2.11, the view factor and RAD-LSI yield very similar results in the region near the lamp. However, the agreement between these two models decreases with increasing radial distance. In this study, the view factor and RAD-LSI models utilize the same attenuation factor calculation (Equation 2.22b), which only accounts for the bending of light due to refraction and absorption effects. The only difference between these two models was in their calculation for fluence rate without refraction, reflection, and absorption effects.

In the region close to the lamp, RAD-LSI will automatically select the RADIAL model that considers the lamp as a cylindrical object. Similarly, view factor approach also takes into account the cylindrical geometry of lamp using a more complicated relationship. The inclusion of the cylindrical geometry would explain the similar performance near the lamp surface. However, far from the lamp surface, RAD-LSI will select the LSI model, which treats the lamp as a summation of point sources. As a result, the disagreement between RAD-LSI and view factor model will be more significant in the regions far from the lamp surface.

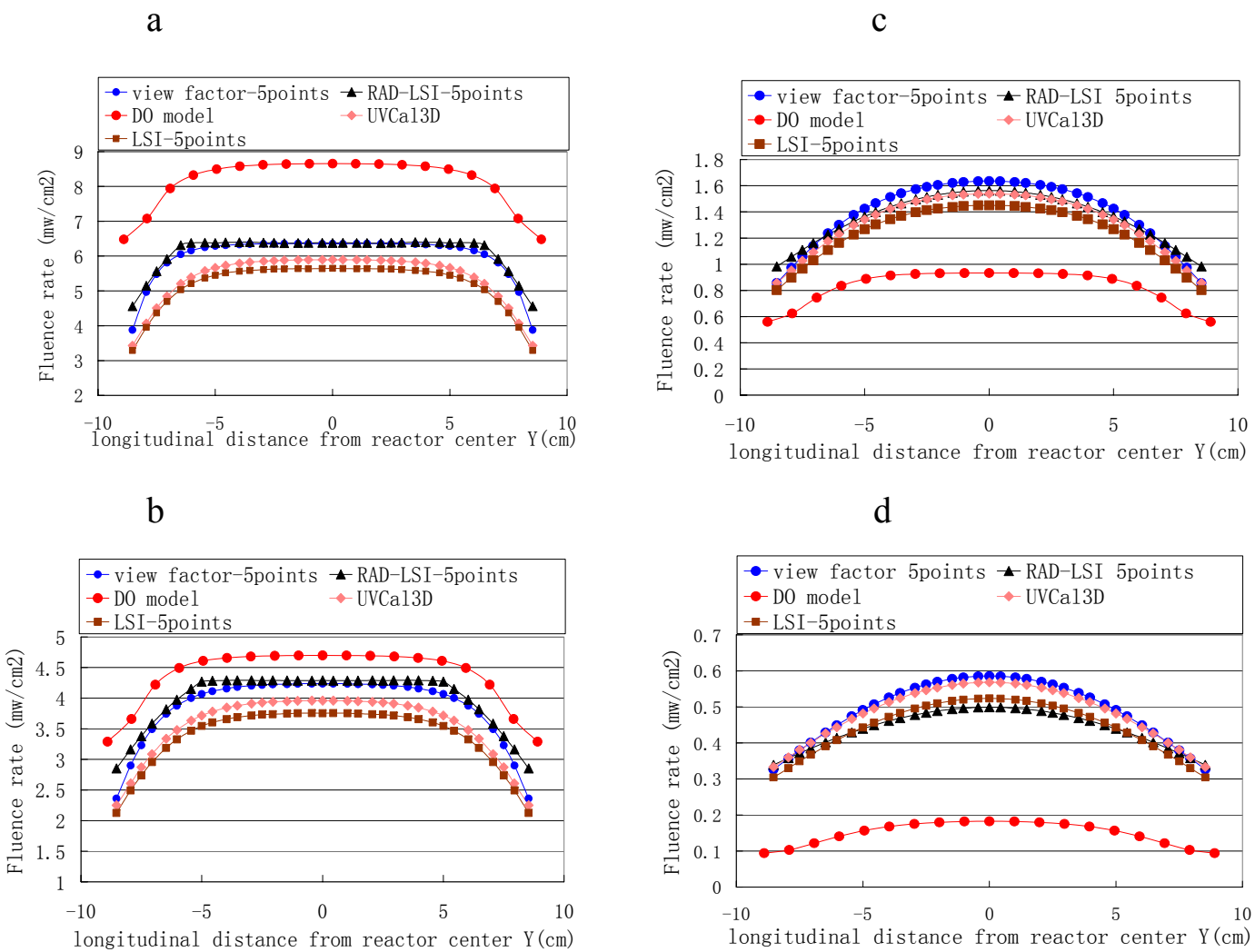

Figure 2.11. Fluence rate longitudinal distribution, perpendicular distance from lamp: a) x = 3.35 cm, b) x = 4.35 cm, c) x = 7.35 cm, d) x = 11.35 cm

While the attenuation factor method seems to be a reasonable approach for modeling the fluence rate with reflection, refraction, and absorption, the user must exercise care in its use. The bending and focus effect of refraction as well as cosine function have their own individual influence on the shape of the fluence rate curve along the lamp length. A basic effect of refraction is light bending, which is caused by the position shift as UV light passes through air/quartz/water interfaces. The bending effect is also a prerequisite for the path length calculation, which is an integral part of the absorption effect in different media. As a result, the attenuation factor with the bending effect should be considered the minimum or basic refraction characterization level.

The focus effect is the second essential part of refraction, which will cause the central region of the longitudinal fluence rate distribution curve to be flatter and cause a sharp reduction in the fluence rate near the lamp ends. As illustrated in Figure 2.11 (a), the RAD-LSI and View Factor models without the focus effect in the attenuation factor calculation already exhibit a flat profile in the central region of the lamp. Consequently, the focus effect should not be included in the attenuation factor when using either RAD-LSI or View Factor models.

The cosine function was introduced to correct for the improper representation of a cylindrical lamp by the point source summation method. The results showed that a cost efficient MSSS approach could be achieved using the LSI with an attenuation factor that includes not only the bending and focusing effects but also the cosine angle effect. The question that still remains is what model should be used in the evaluation of the UV

reactor performance.

In the case of reviewing alternative design or process configurations, a reasonable approach would be to use the RAD-LSI or View Factor model with an attenuation factor that includes absorption and light bending effects (Equation 2.22b). In the case of validating the model performance with biodosimetry tests or when the goal is to develop a numerical online fluence monitoring tool, an MSSS based fluence rate model should be applied to account for all the true physics of UV light. The MSSS fluence rate model could be used without significant cost in computational time and resources for reactors with a low number of lamps (i.e., 6 or less). With larger reactors utilizing more lamps, the LSI with the full attenuation factor (Equation 2.22c) or UVCalc3D could be used since it mimics the accuracy of the MSSS approach with a lower computational time. Moreover, the LSI with the full attenuation factor could further reduce the computational cost of the UVCalc3D model for reactors that contain multiple MP lamps. Overall, the fluence rate model that should be selected for simulations of UV reactor performance will depend on the ultimate use of the numerical data.

2.4.3 Conclusion for evaluation of fluence rate distribution models

A detailed evaluation of several fluence rate distribution models has been performed. These models include the MPSS, MSSS, UVCalc3D, LSI, RAD-LSI, View Factor, and DO. The models were compared with experimental fluence rate measurements using spherical actinometers, which measure the fluence rate at specific points in space.

Experimental fluence rate measurements were performed in air and water at two different transmittances (77 and 88 percent). In addition, an MSSS approach that includes a quartz sleeve thickness when calculating the refraction angle at air/quartz/water interfaces was presented. Moreover, a cost effective approach was developed to simulate the MSSS by combining the LSI model with an attenuation factor that accounts for reflection, refraction, absorption, and cosine angle effects. The results of this study showed that:

- RAD-LSI improved the performance of the original LSI model at the near lamp region. Using a simple minimum function, the RAD-LSI utilizes the RADIAL fluence rate model in regions near the lamp surface and utilizes the LSI model in regions near the lamp ends and far from the lamp surface.
- MSSS model, which includes a quartz sleeve thickness and UVCalc3D, which applies a factor to account for the impact of the quartz sleeve on the fluence rate, produced similar results. This indicates that inclusion of the quartz sleeve thickness in determining the UV light path length was insignificant and that the effect of the quartz sleeve can be approximated by a factor as calculated in UVCalc3D.
- Attenuation Factor method combined with LSI model was shown to be a reasonable compromise between computing time and accuracy with respect to the MSSS model. In addition, the attenuation factor can be incorporated into the View Factor and RAD-LSI model to account for reflection, the bending effects of refraction, and absorption effects.
- RAD-LSI and View Factor predicted similar fluence rate distribution profiles near the

lamp surface. However, the RAD-LSI model tends to predict a lower fluence rate than the View Factor model with increasing radial distance.

- The DO model was found to significantly over predict the fluence rate near the lamp surface and under-predict the fluence rate in regions far from the lamp surface due to the exclusion of the refraction effects.

The selection of bending and focus effect as well as the cosine angle in the Attenuation Factor calculation depends on the different models used. The bending effect is crucial for all models. However, the focus effect and cosine angle correction is only suggested with use in the LSI model.

3. Evaluation of alternative turbulence models

3.1 Introduction

Turbulent flow takes place at large Reynolds numbers, when the viscous stresses are overcome by the fluid's inertia and laminar motion becomes unstable. As a comparison with laminar flow, in which the equations of motion for a viscous fluid are well characterized, turbulent flow involves rapid velocity and pressure fluctuations. In addition, turbulent motion is inherently more complicated, three dimensional, and unsteady. Virtually all flows of practical engineering interest are turbulent, including the flow field inside the UV reactor.

Before turbulence models were utilized in UV system simulations, the UV disinfection modeling was originally performed in batch reactors or perfect plug flow

reactors. For example, Severin et al. (1983), used a series event model to simulate microbial inactivation in a UV batch reactor. In later studies, Scheible (1987) and Loge et al. (1996) combined batch microbial kinetic models with traditional residence time distribution (RTD) models to better predict UV disinfection in flow through reactors. However, these models would not correctly predict the extent of disinfection in UV reactors. While experimental tracer studies could be done to ascertain the hydraulic characteristics of UV reactors and more sophisticated RTD models (Levenspiel, 1972) could be used with a batch microbial kinetic model, the nonuniformity of the fluence rate spatial distribution still could not be incorporated into the RTD approach. Therefore, when an averaged fluence rate value was used with a RTD model, the predicted effluent microbial inactivation level did not match the experimental results (Chiu et al., 1999a).

In an effort to better characterize the actual dose seen by microorganisms, researchers combined sophisticated fluid mechanics measurement techniques (Laser Doppler Velocimetry, LDV) with Lagrangian particle tracking models (random walk model). Chiu et al. (1999a, 1999b) used LDV and a random walk model in an open channel vertical lamp UV system. In Chiu et al., only 2D measurements of the flow field was performed, which limited its applicability to describe the 3 dimensional turbulent nature of the flow field. Furthermore, methods that combine experimental fluid mechanics measurement with random-walk models are difficult to use in evaluating large full-scale UV systems or closed conduit reactors (Buffle et al., 2000). Because the flow patterns in closed-conduit systems with intricate inlet/outlet hydraulic configurations can

be quite complex requiring extensive experimental measurements, Chiu et al.'s approach for analyzing UV systems may be too costly for practical assessment of full-scale in-line UV systems.

The most promising technique for analyzing the mixing behavior inside UV system is using turbulence models to simulate the flow field. Several researchers have used turbulence models for analyzing and improving the hydraulics through UV systems. Baas (1996) developed a 3D CFD model to compare the performance of two in-line UV systems. Baas combined particle tracking with the turbulent flow field predictions to determine the overall dose distribution curve for each design. Downey et al. (1998) used CFD to simulate the flow through an in-line UV system. The 3D-turbulence model was combined with a particle-tracking program to predict the particle exit times and was compared with experimental tracer studies. Lyn et al. (1999) developed a 2D CFD model of an open channel flow UV system. The CFD model combined the MPSS model for fluence rate and the series event kinetic model for disinfection process. Lyn et al. (1999) only modeled the central region of the channel (i.e. no channel walls were modeled) and their results showed a severe over-prediction of the effluent microbial inactivation level.

The advancements in computing technology have allowed other researchers to simulate UV processes using CFD and have shown reasonable agreement with bioassay experiments for the specific reactor analyzed (Baas 1996; Rokjer et al. 2002; Neofotistos et al. 2002; DoQuang et al. 2002; Petri and Olson 2002; Ducoste et al., 2005). Using turbulence models to simulate the flow field inside the UV system could elimilate the

need for using expensive fluid mechanics measurements to determine the fluence distribution. However, the two equation k-ε model was widely used by researchers to capture the characteristic of turbulent flow field. Very little research has been done to investigate the impact of turbulence model selection on the predicted fluence distribution and effluent microbial inactivation. Although, the two equation k-ε model is by far the most commonly used and fully tested turbulence model in practical engineering calculations, it typically has problems in predicting the turbulent flow in shear layers as well as near wall boundary layers (Wilcox, 1998). Lyn et al. (1999) showed that the standard k-ε poorly described the turbulence in the lamp's wake within the UV system.

In this study, five alternative turbulence models, including Renormalized Group (RNG) k-ε, k-ω(88), revised k-ω(98), Reynolds Stress Transport Model (RSTM), and Two-Fluid Model (TFM) have been used to investigate the impact of the selected turbulence model on disinfection process simulation. The k-ε RNG model, a two-equation turbulence model, was developed by Yakhot and Orszag (1986) and revised by Yakhot et al. (1992). Compared with standard k-ε model, k-ε RNG model has a revised dissipation rate production term and modified empirical constants derived from the RNG approach. Speziale et al. (1991) and Smith et al. (1993) showed that the k-ε RNG model improved the prediction of the evolution of the kinetic energy (k) in homogeneous shear flows. Choudhury et al. (1993) reported that k-ε RNG model has superior performance for separated flows and flows involving vortex shedding. However, the k-ε RNG model has been found to poorly predict the velocity profile for the plane

jet flow and round jet flow due to its overestimation of the flow spreading rates (Wilcox 1998).

Like standard k-ε and k-ε RNG, k-ω model is also a two-equation turbulence model. First developed by Wilcox (1988), k-ω model uses transport equations for k and the Reynolds Mean Stress (RMS) fluctuating vorticity, ω. Wilcox (1993) compared the performance of k-ε model and k-ω (88) model in predicting the flow field for boundary layers. The results indicated that the k-ω model is superior both in its treatment of the viscous near-wall region and in its accounting for the effect of streamwise pressure gradients. However, for free shear flow simulations, k-ω (88) model was found to significantly overestimate spreading rates, and consequently under-predict the velocity profile. Menter (1994) proposed a two-equation model designed to yield the best behavior of the k-ε and k-ω models. It utilizes the original k-ω model in the inner region of boundary layers, and switch to standard k-ε model in the outer region and free shear flows. To improve the performance of original k-ω (88) model, Wilcox (1998) incorporated two functions into the coefficients of the dissipation terms and calibrated them to fit for the simulation of free shear flows. This new version of k-ω model is referred as k-ω (98) model in later context. Wilcox (1998) applied the k-ω (98) model along with standard k-ε and k-ε RNG model to compute the free shear flow spreading rates. The k-ω (98) model was found to predict the experimental spreading rates reasonably well for all free shear flows, including far wake, mixing layer, and jet flows. In addition, Speziale et al. (1990) and Menter (1992) have shown that the k-ω model is

numerically very stable, as it tends to produce converged solutions more rapidly than the standard k-ε model. However, both versions of k-ω models have drawbacks on their sensitivities to the ambient turbulent kinetic energy and energy dissipation rate (Wilcox 1998). This drawback could still lead to poor performance when using the k-ω model in the turbulent shear flow with significant impact from the ambient kinetic energy and energy dissipation rate.

The turbulence models previously discussed are all based on the Boussinesq eddy-viscosity concepts, which assumes the principal axes of the Reynolds stress tensor is coincident with those of the mean strain rate tensor at all points of a turbulent flow (Wilcox, 1998). While models based on the Boussinesq approximation provide reasonable predictions for many engineering flows, there are some applications for which predicted flow properties differ greatly from corresponding measurements. These failed applications include flows with sudden changes in mean strain rate, flows over curved surfaces, as well as flows in ducts with secondary motions (Wilcox, 1998). For these types of flows, the eddy-viscosity concept may be too simple and can not describe the complex strain rate field, in which non-isotropic turbulent characteristics play a very important role.

Reynolds Stress Transport Model (RSTM) allows for both the transport and development of individual Reynolds stresses. Launder (1989a, 1989b) and Leschziner (1990) have demonstrated the superiority of RSTMs over eddy-viscosity models for curved flows, swirling flows, buoyant flows, and recirculating flows. However, a full

RSTM closure consists, in general, of 6 transport equations for the Reynolds stresses, 3 transport equations for the turbulent fluxes of each scalar property and one transport equation for the dissipation rate of turbulence energy, ε. The solution of all these complex equations together with those of the mean flow is not an insignificant task. In addition, there is a considerable numerical disadvantage in using RSTM approach since the eddy viscosity provides a stabilizing effect in the mean flow equations (So and Yuan, 1998). Although RSTM's approach can provide a more realistic representation of complex engineering flows, their applications are very expensive in terms of storage and execution time particularly for three dimensional flows.

One possible alternative to the eddy viscosity and RSTM approaches is the Two Fluid Model (TFM). The basic premise of the TFM approach is that a turbulent flow can be approximated as a mixture of two fluids, each moving semi-independently in the same space. Spalding (1983) first proposed the TFM approach with an equation system comprising of two sets of velocities and two volume fractions from the analogy between intermittent turbulent flow and two-phase flow. Malin and Spalding (1984) used the TFM to predict flow field and heat transfer of the plane jet and wake flow. In their study, the standard k-ε model was used to calculate the turbulent component of the fluid. Malin and Spalding's results showed reasonable agreement with the experimental data for the spreading rate, turbulent energy, and maximum value of the turbulent shear stress. However, the TFM was unable to predict the experimental intermittency due to a lack of source terms describing the level of entrainment of the surrounding fluid into the plane jet

or wake flow region.

In a later study, Ilegbusi and Spalding (1987a, 1987b, 1989) investigated the performance of the TFM for near wall boundary layer flows, close conduit flows, and free shear layer flows. Although the model constants were calibrated in their study to fit the flat wall boundary layer flow and free shear layer flow very well, substantial adjustment to the exchange constant coefficient was still required for pipe and channel flows. Ilegbusi (1994) also employed the TFM and standard k-ε model to simulate the flow inside a tundish, which comprises of jet and wall boundary layer flows. The TFM was found to better simulate the physics of the system than standard k-ε model and predicted a highly turbulent region near the inlet and an essentially laminar region in the remainder of the system.

In this study, standard k-ε, k-ε RNG, k-ω (88), k-ω (98), RSTM, and TFM models were applied to simulate the turbulent flow field inside a polychromatic UV disinfection reactor with four UV lamps perpendicular to the flow direction. To evaluate the performance of these turbulence models, the predicted flow field, turbulent kinetic energy and energy dissipation rate were compared with the Particle Image Velocimetry (PIV) measurement data at four sites close to UV lamps. The predicted flow fields have been combined with a Multiple Segment Source Summation (MSSS) based fluence rate model and three different microbial inactivation kinetic models to investigate the impact of turbulence model selection on the fluence distribution and effluent microbial inactivation simulations. All simulations were performed at two UV lamp power conditions. The

equations of these turbulence models, fluence rate model, microbial inactivation models, as well as the numerical simulation details are discussed in the following section.

3.2 Turbulence models

The simulation of turbulence flow field requires the solution of the conservation of mass (Equation 3.1) and momentum (Equation 3.2) equations.

Continuity:

$$\frac{\partial \overline{U}_i}{\partial x_i} = 0 \tag{3.1}$$

Navier Stokes:

$$\frac{\partial \overline{U}_i}{\partial t} + \frac{\partial (\overline{U_i}\,\overline{U_j})}{\partial x_j} = -\frac{1}{\rho}\frac{\partial P}{\partial x_i} + \frac{\partial}{\partial x_j}\left[\nu\left(\frac{\partial \overline{U_i}}{\partial x_j} + \frac{\partial \overline{U_j}}{\partial x_i}\right) - \overline{u_i u_j}\right] \tag{3.2}$$

Equations (3.1) and (3.2) are not complete and suffer a closure problem due to the existence of turbulence stress term $-\overline{u_i u_j}$. The section below describe the different closure relationships for the Reynolds stresses.

3.2.1 Standard k-ε model

Launder and Spalding (1974) developed the standard two equation k-ε model to solve this closure problem with the following equations:

Kinematic eddy viscosity:

$$\nu_t = C_\mu k^2 / \varepsilon \tag{3.3}$$

Turbulence kinetic energy:

$$\frac{\partial k}{\partial t} + \overline{U_j}\frac{\partial k}{\partial x_j} = \nu_t\left(\frac{\partial \overline{U_i}}{\partial x_j} + \frac{\partial \overline{U_j}}{\partial x_i}\right)\frac{\partial \overline{U_i}}{\partial x_j} + \frac{\partial}{\partial x_j}\left[\left(\nu + \frac{\nu_t}{\sigma_k}\right)\frac{\partial k}{\partial x_j}\right] - \varepsilon \tag{3.4}$$

Dissipation rate:

$$\frac{\partial \varepsilon}{\partial t} + \overline{U_j}\frac{\partial \varepsilon}{\partial x_j} = C_{\varepsilon 1}\frac{\varepsilon}{k}\nu_t\left(\frac{\partial \overline{U_i}}{\partial x_j} + \frac{\partial \overline{U_j}}{\partial x_i}\right)\frac{\partial \overline{U_i}}{\partial x_j} - C_{\varepsilon 2}\frac{\varepsilon^2}{k} + \frac{\partial}{\partial x_j}\left[(\nu + \nu_t/\sigma_\varepsilon)\frac{\partial \varepsilon}{\partial x_j}\right] \qquad (3.5)$$

Reynolds stresses:

$$-\overline{u_i u_j} = \nu_t\left(\frac{\partial \overline{U_i}}{\partial x_j} + \frac{\partial \overline{U_j}}{\partial x_i}\right) - \frac{2}{3}k\delta_{ij} \qquad (3.6)$$

The empirical constants used in this model are shown below:

$C_{\varepsilon 1} = 1.44,\ C_{\varepsilon 2} = 1.92,\ C_\mu = 0.09,\ \sigma_k = 1.0,\ \sigma_\varepsilon = 1.3$

3.2.2 k-ε RNG model

k-ε RNG model was developed by Yakhot and Orszag (1986) from techniques of the renormalization group theory. In this model, the eddy viscosity, k, and ε are still given by Equations (3.3), (3.4) and (3.5). However, the model uses a modified coefficient, $C_{\varepsilon 2}$, defined as:

$$C_{\varepsilon 2} = \widetilde{C}_{\varepsilon 2} + \frac{C_\mu \lambda^3 (1 - \lambda/\lambda_0)}{1 + \beta\lambda^3} \qquad (3.7)$$

where, $\lambda = \frac{k}{\varepsilon}\sqrt{2S_{ij}S_{ji}}$ and $S_{ij} = \frac{1}{2}\left(\frac{\partial \overline{U_i}}{\partial x_j} + \frac{\partial \overline{U_j}}{\partial x_i}\right)$

The empirical constants for the RNG k-ε model are:

$C_{\varepsilon 1} = 1.42,\ \widetilde{C}_{\varepsilon 2} = 1.68,\ C_\mu = 0.085,\ \sigma_k = 0.72,\ \sigma_\varepsilon = 0.72,\ \beta = 0.012,\ \lambda_0 = 4.38$

3.2.3 k-ω (88) model

k-ω model (88) also uses the Boussinesq assumption as shown in Equation (3.6).

Other equations used in the k-ω model are defined as follows:

Kinematic eddy viscosity:

$$\nu_t = k/\omega \tag{3.8}$$

Turbulence kinetic energy:

$$\frac{\partial k}{\partial t} + \overline{U_j}\frac{\partial k}{\partial x_j} = \nu_t\left(\frac{\partial \overline{U_i}}{\partial x_j} + \frac{\partial \overline{U_j}}{\partial x_i}\right)\frac{\partial \overline{U_i}}{\partial x_j} + \frac{\partial}{\partial x_j}\left[(\nu + \sigma^*\nu_t)\frac{\partial k}{\partial x_j}\right] - \beta^* k\omega \tag{3.9}$$

Specific dissipation rate:

$$\frac{\partial \omega}{\partial t} + \overline{U_j}\frac{\partial \omega}{\partial x_j} = \alpha\frac{\omega}{k}\nu_t\left(\frac{\partial \overline{U_i}}{\partial x_j} + \frac{\partial \overline{U_j}}{\partial x_i}\right)\frac{\partial \overline{U_i}}{\partial x_j} + \frac{\partial}{\partial x_j}\left[(\nu + \sigma\nu_t)\frac{\partial \omega}{\partial x_j}\right] - \beta\omega^2 \tag{3.10}$$

Empirical constants and auxiliary relations are defined as:

$$\beta^* = 0.09,\ \sigma = 0.5,\ \sigma^* = 0.5,\ \alpha = 5/9,\ \beta = 3/40$$

3.2.4 k-ω (98) model

The k-ω (98) model also uses the same k and ω equations as shown in Equation (3.9) and (3.10). However, the empirical constants are revised as (Wilcox, 1998):

$$\beta^* = \beta_0^* f_{\beta^*},\ \sigma = 0.5,\ \sigma^* = 0.5,\ \alpha = 13/25,\ \beta = \beta_0 f_\beta$$

$$\beta_0^* = 0.09, \quad f_{\beta^*} = \begin{cases} 1, & \chi_k \le 0 \\ \dfrac{1+680\chi_k^{\,2}}{1+400\chi_k^{\,2}}, & \chi_k > 0 \end{cases}, \quad \chi_k = \frac{1}{\omega^3}\frac{\partial k}{\partial x_j}\frac{\partial \omega}{\partial x_j} \tag{3.11}$$

$$\beta_0 = 9/125, \quad f_\beta = \frac{1+70\chi_\omega}{1+80\chi_\omega}, \qquad \chi_\omega = \left|\frac{\Omega_{ij}\Omega_{jk}S_{ki}}{(\beta_0^*\omega)^3}\right| \tag{3.12}$$

$$\Omega_{ij} = \frac{1}{2}\left(\frac{\partial U_i}{\partial x_j} - \frac{\partial U_j}{\partial x_i}\right), \qquad S_{ij} = \frac{1}{2}\left(\frac{\partial U_i}{\partial x_j} + \frac{\partial U_j}{\partial x_i}\right) \tag{3.13}$$

3.2.5 Reynolds Stress Transport model

RSTM provides closure to the Reynolds stresses using Reynolds stress transport equations together with the dissipation rate equation. In the RSTM approach, the Reynolds stress transport equation is defined as (Wilcox, 1998):

$$\frac{\partial \overline{u_i u_j}}{\partial t} + \overline{U_k} \frac{\partial \overline{u_i u_j}}{\partial x_k} = \text{Diff}(\overline{u_i u_j}) + P_{ij} + R_{ij} - E_{ij} \tag{3.14}$$

In Equation 3.14, $\text{Diff}(\overline{u_i u_j})$ represents the diffusive transport, which is modeled by a simplified form of the Daly-Harlow (1970) model:

$$\text{Diff}(\overline{u_i u_j}) = C_s \frac{\partial}{\partial x_k}\left(\frac{k}{\varepsilon} \overline{u_k u_k} \frac{\partial \overline{u_i u_j}}{\partial x_k} \right) \tag{3.15}$$

The stress production term, P_{ij}, is defined as:

$$P_{ij} = -\left(\overline{u_i u_k} \frac{\partial \overline{U_j}}{\partial x_k} + \overline{u_j u_k} \frac{\partial \overline{U_i}}{\partial x_k} \right) \tag{3.16}$$

E_{ij}, defined by Equation 3.17, represents the viscous destruction of Reynolds stresses and is modeled by assuming local isotropy.

$$E_{ij} = \frac{2}{3} \varepsilon \delta_{ij} \tag{3.17}$$

The pressure-strain term, R_{ij}, acts to redistribute energy among the normal stresses and to reduce the shear stresses. This term, which tends to make the turbulence more isotropic, is modeled as (Speziale, Sarkar and Gatski, 1991):

$$\begin{aligned} R_{ij} = &-(C_1 \varepsilon + C_{1s} P_{kk}) b_{ij} + C_2 \varepsilon \left(b_{ik} b_{ij} - b_{mn} b_{mn} \delta_{ij} / 3 \right) + \left(C_3 - C_{3s} \sqrt{b_{mn} b_{mn}} \right) k S_{ij} \\ &+ C_4 k \left(b_{ik} S_{jk} + b_{jk} S_{ik} - 2 b_{mn} S_{mn} \delta_{ij} / 3 \right) + C_5 k \left(b_{ik} \omega_{jk} + b_{jk} \omega_{ik} \right) \end{aligned} \tag{3.18}$$

where, b_{ij}, S_{ij} and ω_{ij} are the anisotropic Reynolds-stress, the mean rate of strain, and the mean vorticity tensors, respectively. They are defined as:

$$b_{ij} = \frac{1}{2}\frac{\overline{u_i u_j}}{k} - \frac{\delta_{ij}}{3} \tag{3.19}$$

$$S_{ij} = \frac{1}{2}\left(\frac{\partial \overline{U_i}}{\partial x_j} + \frac{\partial \overline{U_j}}{\partial x_i}\right) \tag{3.20}$$

$$\omega_{ij} = \frac{1}{2}\left(\frac{\partial \overline{U_i}}{\partial x_j} - \frac{\partial \overline{U_j}}{\partial x_i}\right) \tag{3.21}$$

The dissipation rate equation is finally defined as:

$$\frac{\partial \varepsilon}{\partial t} + \overline{U_j}\frac{\partial \varepsilon}{\partial x_j} = C_\varepsilon \frac{\partial}{\partial x_k}\left(\frac{k}{\varepsilon}\overline{u_k u_m}\frac{\partial \varepsilon}{\partial x_m}\right) + C_{\varepsilon 1}\frac{\varepsilon}{k}\overline{u_i u_j}\frac{\partial \overline{U_i}}{\partial x_j} - C_{\varepsilon 2}\frac{\varepsilon^2}{k} \tag{3.22}$$

The empirical constants used in the RSTM approach are defined below:

$C_\varepsilon = 0.183,\ C_{\varepsilon 1} = 1.44,\ C_{\varepsilon 2} = 1.83,\ C_s = 0.21,\ C_1 = 3.4,\ C_2 = 4.2$

$C_{1s} = 1.8,\ C_3 = 0.8,\ C_{3s} = 1.3,\ C_4 = 1.25,\ C_5 = 0.4$

3.2.6 Two-Fluid model

In the TFM approach, the two fluids occupy a portion of space that is proportional to their volume fractions, r_1 and r_2. r_1 and r_2 are related through mass conservation as:

$$r_1 + r_2 = 1 \tag{3.23}$$

The governing equations for all dependent variables for fluid i can be written as (Ilegbusi and Spalding, 1987):

$$\frac{\partial}{\partial t}\rho_i r_i \phi_i + \nabla \cdot (r_i \rho_i U_i \phi_i - \Gamma_{\phi i} r_i \nabla \phi_i) = S_{\phi i}^{ii} + S_{\phi i}^{ij} \tag{3.24}$$

where

$\phi =$ the dependent variable

$\Gamma_{\phi i} =$ a form of exchange coefficient

$S_{\phi i}^{ii}$ = intra-fluid source terms

$S_{\phi i}^{ij}$ = inter-fluid source terms

The equation for r_i results from setting $\phi_i = 1$ in Equation (3.24). $\Gamma_{\phi i}, S_{\phi i}^{ii}$ and $S_{\phi i}^{ij}$ in Equation (3.24) are given in Table 3.1,

Table 3.1 diffusion flux coefficients and source terms

Equation	$\Gamma_{\phi i}$	$S_{\phi i}^{ii}$	$S_{\phi i}^{ij}$
Mass balance	0	0	E_{ij}
Momentum	$C_t l r_i r_j \lvert U_i - U_j \rvert$	$-r_i \nabla p$	$F_{ij} + U_j E_{ij}$

l represents the length scale of the energy containing eddies, E_{ij} is the rate of volumetric entrainment of fluid j by fluid i, and F_{ij} is the volumetric inter-fluid friction. Along with source terms $S_{\phi i}^{ii}$ and $S_{\phi i}^{ij}$, an additional source term, $SHSO$, is included in the cross-stream momentum equations. It is used to describe the tendency of a shear layer to break up into a succession of eddies. The source term, $SHSO$, is defined by Equation 3.25.

$$SHSO_v = C_V \rho \lvert U_1 - U_2 \rvert \left| \frac{\partial uu}{\partial y} \right| \tag{3.25a}$$

$$SHSO_w = C_V \rho \lvert U_1 - U_2 \rvert \left| \frac{\partial uu}{\partial z} \right| \tag{3.25b}$$

In Equations (3.25), the main stream velocity is assumed along the x direction. $SHSO_v$ and $SHSO_w$ represent the additional source term in y and z direction, respectively. uu is the mean main stream velocity, defined as: $uu = u_1 r_1 + u_2 r_2$. In this study, $SHSO$ is chosen arbitrarily as positive for fluid two, and negative for fluid one (Norberto Fueyo, 1989).

The entrainment rate, E_{ij}, and the inter-fluid friction, F_{ij}, are defined as:

$$E_{ij} = C_m \rho_i l^{-1} (r_j - 0.5) r_i r_j \left| U_i - U_j \right| \tag{3.26}$$

$$F_{ij} = C_f \rho_i l^{-1} r_i r_j (U_j - U_i) \left| U_i - U_j \right| \tag{3.27}$$

The length scale l is defined by (Norberto, 1989):

$l = \min(l_1, l_2)$

l_1, l_2 are calculated by solving the differential equations:

$$\frac{Dl_i}{Dt} = C_a \left| U_1 - U_2 \right| - C_b l_i \sqrt{(\frac{\partial u_i}{\partial y})^2 + (\frac{\partial u_i}{\partial z})^2} \qquad i = 1,2 \tag{3.28}$$

The empirical constants used in the TFM approach are:

$C_m = 10.0$, $C_v = 0.3$, $C_f = 0.05$, $C_t = 10.0$, $C_a = 0.03$, $C_b = 0.01$

3.3 Lagrangian approach for disinfection simulation

When CFD is combined with information on the UV fluence rate (defined as "the radiant power passing from all directions through an infinitesimally small sphere of cross-sectional area dA, divided by dA", Bolton 2000) distribution, specific predictions of the fluence that individual microbes may experience based on their unique path through a UV reactor can be made. Some researchers have combined particle-tracking

models with CFD to predict the fluence distribution (Baas 1996; Rokjer et al. 2002; Neofotistos et al. 2002; DoQuang et al. 2002; Petri and Olson 2002; Ducoste et al., 2005). These CFD numerical particle-tracking models are considered Lagrangian type models where the fluence is determined from the time-history of each particle (i.e., pathogen) released in the reactor influent during the numerical simulation.

In this study, CFD particle tracking models use a Lagrangian approach to describe the motion of particles within a flow field (Crowe et al. 1977). The particle position is simply determined from the solution to the equation $dX_p/dt = U_p$, where X_p is the particle position vector and U_p is the particle velocity, which is equal to a time averaged mean velocity plus a turbulent fluctuating velocity. The particle velocity was determined from the particle momentum equation:

$$m_p \frac{du_{p,i}}{dt} = D_{p,i}(u_i - u_{p,i}) + m_p g_i \qquad i = 1,2,3 \tag{3.29}$$

where subscript i represents the projection values of variable in dimensional axis i, m_p is the particle mass, $D_{p,i}$ is a drag function, u_i is the carrier phase instantaneous velocity, $u_{p,i}$ is the particle velocity, and g is the gravitational acceleration. The source terms on the right hand side of Equation 3.29 are drag force and gravitational force. The drag function used in Equation 3.29 was described as follows (Fueyo et al. 1997):

$$D_{p,i} = 0.5\ \rho\ A_p\ C_D\ \left|u_i - u_{p,i}\right| \tag{3.30}$$

where A_p = particle projected area = $\frac{\pi d_p^2}{4}$, the drag coefficient C_D is given by (Clift et al. 1978): $C_D = \frac{24}{\mathrm{Re}}\left(1 + 0.15\,\mathrm{Re}^{0.687}\right) + \frac{0.42}{1 + 4.25x10^4\,\mathrm{Re}^{-1.16}}$, and Re = particle Reynolds number.

In Equation 3.30, the carrier phase instantaneous velocity, u_i , is equal to the local mean velocity plus a turbulent fluctuating velocity. The turbulent fluctuating velocity is calculated assuming each velocity component follows a Gaussian distribution with a mean of zero and a standard deviation (σ) that can be calculated as $\sigma = \sqrt{2k/3}$. In the σ equation, k is the local turbulent kinetic energy that is determined from the CFD turbulent flow solution of the carrier phase. The final determination of the fluctuating velocity component is done through random sampling of the normal distribution and adding it to the local mean velocity (Faeth 1983).

In the Lagrangian particle tracking method, the random fluctuations seen by the particles are caused by particle interactions with turbulent eddies in the flow field (Shirolkar et al. 1996). This interaction time scale is important in determining how often a new random number will be generated. The interaction time between a particle and a turbulent eddy was determined by one of the following conditions: 1) the particle moves sufficiently slow relative to the carrier phase to remain within the eddy throughout the eddy's lifetime (t_{eddy}), or 2) the velocity difference between the carrier phase and particle is sufficient to traverse the eddy in a transit time (t_{tr}) that is shorter than the eddy lifetime. The overall interaction time scale was determined as follows (Fueyo et al. 1997):

$$t_{in} = \min\left(t_{eddy}, t_{tr}, t_{user}\right) \tag{3.31}$$

where. $t_{eddy} = \sqrt{\frac{3}{2}} C_{\mu}^{3/4} \frac{k}{\varepsilon}$, $t_{tr} = C_{\mu}^{3/4} \frac{k^{3/2}}{\varepsilon} \Big/ \left|u - u_p\right|$.

t_{user} is a user defined time scale, which is the minimum computational cell crossing time. t_{user} is calculated as the product of the minimum number of time steps per computational cell, which is determined by the user, and the minimum cell dimension divided by the maximum velocity component through that cell. A new random number was generated only when the particle has traversed the eddy or has spent more time than the eddy lifetime. In this study, a spatial homogeneous concentration of 1500 particles was released at the UV system influent. Each particle was tracked until it exited the reactor.

The fluence is calculated by computing the time integral of the fluence rate values over the particle track time history (Chiu et al. 1999). The fluence distribution is then computed by organizing the fluence from all the particle track information into discrete bin sizes of different fluence values. Using the particle tracking method, the overall microbial inactivation can then be computed as:

$$\left(N / N_0\right)_{effluent} = \int_0^{\infty} f(H^{'}) E(H^{'}) dH^{'} \tag{3.32}$$

where $H^{'}$ is the fluence, $f(H^{'})$ represents the collimated-beam fluence-response inactivation function (defined as the function of normalized concentration of the

surviving microorganism, N/N_0 , with respect to the fluence received by the microorganism), $\left(N/N_0\right)_{effluent}$ represents the effluent normalized concentration of surviving organisms, and $E(H^{'})$ represents the particle number fraction.

In Equation 3.32, the collimated-beam fluence-response inactivation function may change significantly depending on the type of microorganisms and the test conditions. To investigate the impact of different turbulence models on disinfection simulation with diverse inactivation functions, two different microorganisms, MS2 coliphage (MS2) and *Bacillus subtilis* (*B.subtilis*) bacterial spores, were used for the collimated-beam fluence-response test. In Table 3.2 and Figure 3.1, the Chick-Watson model was used to simulate the fluence response of MS2, and Cabaj-Sommer models (1) and (2) (Cabaj and Sommer, 2000) correspond to the fluence response of two different strains of *B.subtilis*.

The local fluence rates in the UV reactor were computed using a commercially available Multiple Segment Source Summation (MSSS) model, known as UVCalc3D (Bolton Photosciences Inc., Edmonton, Canada). An evaluation of the different fluence rate models was performed in Chapter 2 by comparing the predicted fluence rate distribution with spherical actinometer measurements. As indicated in Chapter 2, the MSSS approach or models that incorporated the MSSS concept best predicted the fluence rate distribution. In addition, UVCalc3D accounts for lamp-to-lamp shadowing that was not included in other fluence rate models. Moreover, for polychromatic lamp modeling, a multi-wavelength approach encompassing 20 wavelengths at 5 nm intervals between

200-300 nm was utilized. For each wavelength band, model inputs included water and quartz sleeve transmissivities, fraction of lamp power, and germicidal efficiency for the challenge microorganism as shown in Table 3.3. In this study, a generic DNA germicidal efficiency (Bolton 2000) was used.

Table 3.2 Fluence-response inactivation functions

Chick-Watson model MS2	N/N_o = 10^(-$k_1 E^{'} t$+k_2) k_1=0.064 cm^2/(mJ·Sec), k_2=0.361
Cabaj-Sommer model (1) *B.Subtilis*	$N/N_o = (1-(1-(10\text{^}(-k_1 E^{'} t)))\text{^}(10k_3) + a10\text{^}(-k_2 E^{'} t))/(1+a)$ k_1=0.117cm^2/(mJ·Sec), k_2=0.0002169cm^2/(mJ·Sec) k_3=0.54265, a=0.000286
Cabaj-Sommer model (2) *B.Subtilis*	$N/N_o = (1-(1-(10\text{^}(-k_1 E^{'} t)))\text{^}(10k_3) + a10\text{^}(-k_2 E^{'} t))/(1+a)$ k_1=0.2128cm^2/(mJ·Sec) , k_2=0.009262cm^2/(mJ·Sec) k_3=0.95475, a=0.00311

Table 3.3 Description of water UVT, power factor, germicidal efficiency factor, quartz sleeve absorption factor for the multi-wavelength simulation.

Wave length	Water UVT	Lamp power factor	Quartz sleeve absorption	Germicidal factor
200-204nm	37	0.0232	0.67	1.52
205-209nm	45	0.0306	0.72	1.31
210-214nm	53	0.0404	0.78	1.07
215-219nm	63	0.0486	0.85	0.8
220-224nm	73	0.0529	0.9	0.57
225-229nm	81	0.049	0.92	0.47
230-234nm	86	0.0431	0.92	0.46
235-239nm	89	0.0375	0.91	0.53
240-244nm	90	0.0194	0.91	0.67
245-249nm	91	0.0439	0.92	0.83
250-254nm	92	0.0726	0.94	0.97
255-259nm	92	0.1489	0.96	1.02
260-264nm	93	0.0762	0.98	1.01
265-269nm	93	0.0732	0.98	0.93
270-274nm	94	0.0287	0.99	0.81
275-279nm	94	0.0349	0.99	0.67
280-284nm	95	0.0446	0.99	0.51
285-289nm	95	0.0216	0.99	0.34
290-294nm	95	0.027	0.99	0.21
295-299nm	96	0.0837	0.99	0.11

(a)

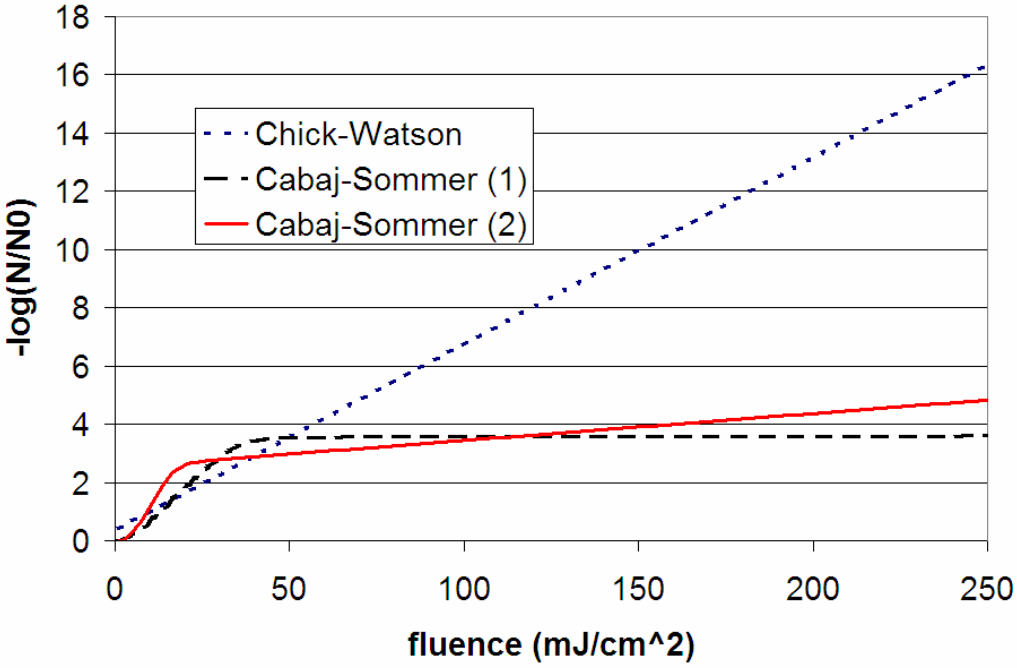

(b)

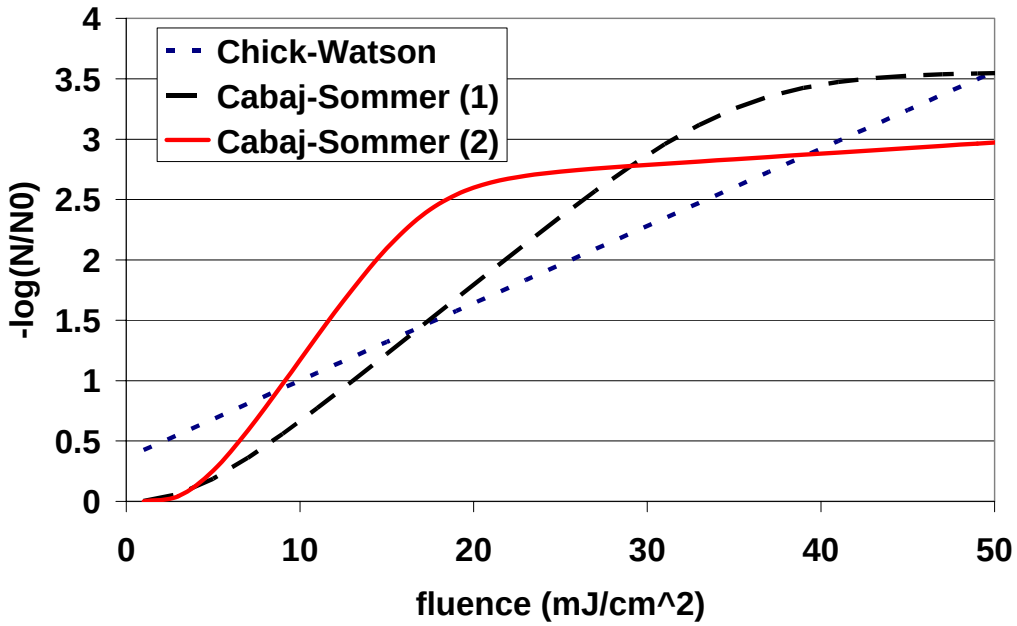

Figure 3.1 Fluence response curves for three inactivation function

(a) overall range (b) close up of low fluence range

3.4 Experimental measurement of turbulent flow field

In this study, the fluid flow patterns and turbulence within the closed conduit UV reactor was quantified using the Particle Image Velocimetry (PIV) method. PIV is a laser based non-intrusive fluid measurement technique that is based on illuminating a seeded flow field with a planar laser sheet (Raffel, 1998). The laser sheet is pulsed twice, forming two images of each seed particle. This double image is recorded by a camera and subsequently interrogated to find image displacements at successive points in the flow.

The PIV photographs are analyzed by computing a two-dimensional cross-correlation of the illuminated spot (Raffel, 1998). The cross-correlation then gives the most likely distance for the original particle images. Thousands of these photographs are taken over time to extract information such as mean velocity, velocity standard deviation, vorticity, and strain rate. PIV generated images was used to describe some of the unique turbulence structures in the UV reactor as well as the mean velocity field. The whole-field images of turbulent structures generated by PIV can help better explain the behavior of mixing and microbial transport within the UV reactor.

To obtain significant mean and turbulence statistics, a duration of 10, 20, and 30 seconds ensemble average were used. The mean velocity was estimated as

$$\overline{\vec{V}(x,z)} = \frac{1}{N}\sum_{i=1}^{N}\vec{V}(x,z,t_i)\,, \tag{3.33}$$

where the overbar represents the ensemble average; x and z are the coordinate system as shown in Figure 3.2 (a) and N = 300, 600, and 900 are the total frame number (Wu et al.

2004). The instantaneous velocity is decomposed into the mean velocity and turbulent fluctuating velocity as

$$\vec{V}(x,z,t_i) = \overline{\vec{V}(x,z)} + \vec{V}'(x,z,t_i) \tag{3.34}$$

where the superscript prime represents the turbulent fluctuation. The turbulence kinetic energy was defined as

$$k \approx \frac{1.4}{2}(\overline{u'u'} + \overline{w'w'}) \quad . \tag{3.35}$$

The local two-dimensional turbulence energy dissipation (Hinze 1975) was estimated by

$$\varepsilon = \overline{2\nu\left(\frac{\partial u'}{\partial x}\right)^2 + \nu\left(\frac{\partial u'}{\partial z}\right)^2 + 2\nu\left(\frac{\partial u'}{\partial z}\right)\left(\frac{\partial w'}{\partial x}\right) + \nu\left(\frac{\partial w'}{\partial x}\right)^2 + 2\nu\left(\frac{\partial w'}{\partial z}\right)^2} \tag{3.36}$$

where $\nu = 10^{-6} m^2 / s$ is the kinematic viscosity.

The PIV measurements conducted in this study focused on near wall regions and in the UV lamp wake to properly quantify boundary layer structures and velocity flow field. These tests were performed at the University of Wisconsin at Madison by Dr. Chin Wu's research group.

3.5 Numerical details

Figure 3.2 displays the reactor configuration used in this study. This reactor is a modified version of a commercially available polychromatic drinking water UV system. The lamps have been replaced with equivalent size cylinders with a diameter 0.039 meter. The wiper assembly has been removed with the guide rods still in place. The 3 guide rods have diameters of 0.023m, 0.016m and 0.023m, respectively. The inlet flow velocity is

0.86 m/s and the flow direction is from right to left as shown in Figure 3.2(a). The coordinate system that was used for the modeling and the experimental fluid mechanics measurement is also shown in Figure 3.2 (a).

All turbulence models used the same grid system, inlet and outlet conditions, as well as the log law wall boundary conditions. A finite volume commercial CFD code PHOENICS (CHAM, England) was used to perform the simulation. PHOENICS utilizes the Semi Implicit Method for Pressure Link Equation (SIMPLE) numerical scheme to take care of the pressure velocity couple. A sharp monotonic algorithm for realistic transport (SMART) scheme (Gaskell and Lau 1988) was used to discretize the convection portion of the transport equations. Convergence of the numerical solution was based on two parts: a) the sum of the absolute residual sources over the whole solution domain must be less than 2 percent of the total inflow quantity and b) the values of the monitored dependent variables at several locations must not change by more than 0.1 percent between successive iterations. These convergence criteria represent an upper bound with actual simulations achieving less than 0.001 percent.

For the disinfection simulation, two lamp power conditions, 1000 watts and 3900 watts, were used to predict the inactivation of two organisms, MS2 and *B.subtilis*, with three different inactivation functions as shown in Table 3.2. The UVC efficiency of the lamp was set to 20 percent for all calculations and the water transmissivity was arbitrarily chosen as 92 percent per 10mm distance for the 254nm wavelength. The refractive index of air and water were set to 1.0 and 1.38, respectively.

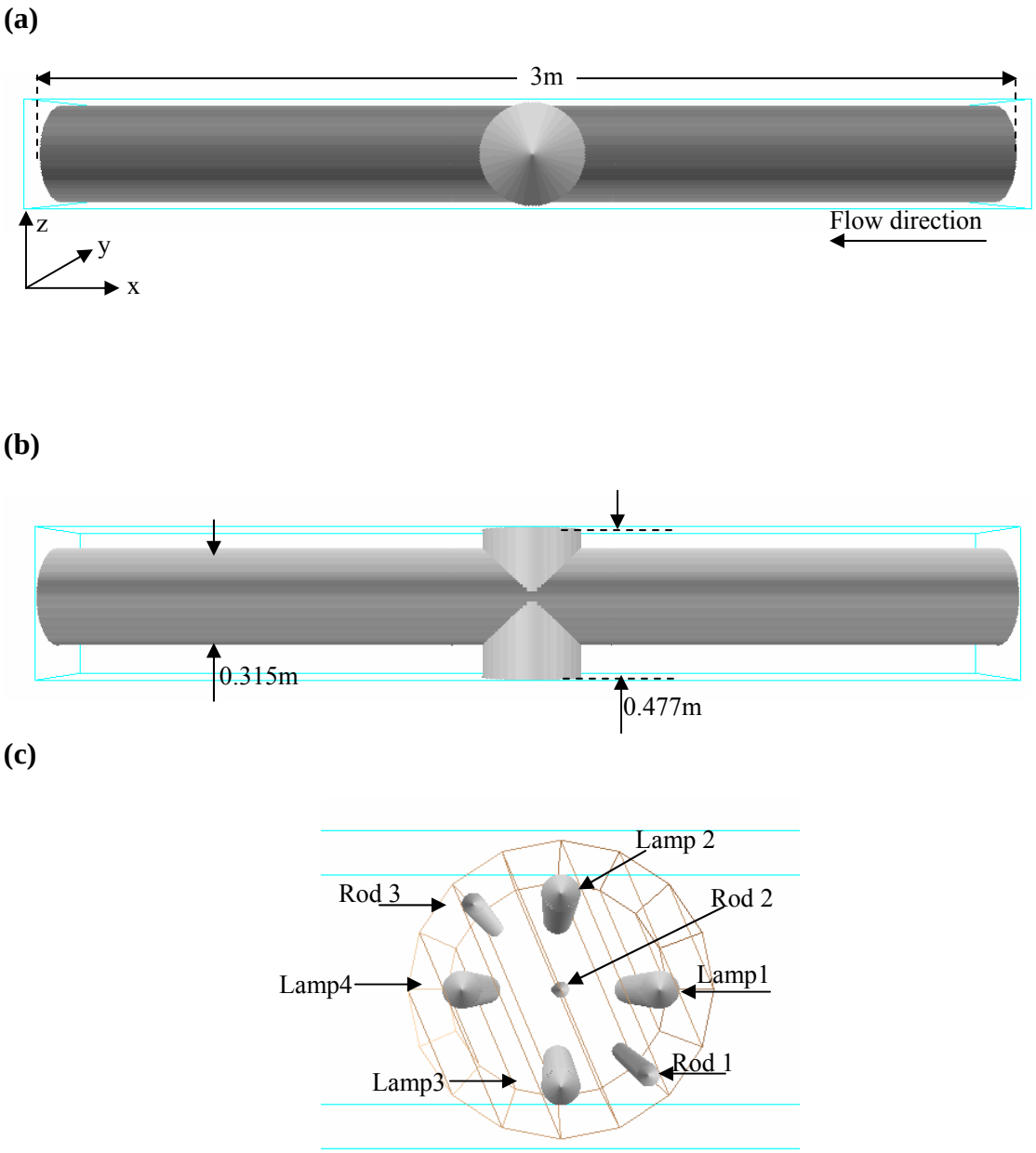

Figure 3.2 reactor configuration: (a) side view (b) top view (c) reactor interior

3.6 Simulation results and analysis

In this section, the first part will compare and analyze the predicted x direction velocity (i.e., direction of the main flow), turbulent kinetic energy, and energy dissipation rate produced using STD k-ε, k-ε RNG, k-ω (88), k-ω (98), RSTM, and TFM turbulence models with the PIV measurement at four locations as shown in Figure 3.3. The simulated fluence distribution and effluent microbial inactivation predicted with these turbulence models at the two different lamp power conditions and three fluence response functions will be presented in the second part.

3.6.1 Comparison of flow field results

The goodness of fit between the experimental and the predicted main stream velocity was computed as (Tarald 1985):

$$R^2 = 1 - \sum_i (I_i - \hat{I}_i)^2 / \sum_i (I_i - \bar{I})^2 \qquad (3.37)$$

where, I_i represents the experimental results, $\bar{I}$ is the average value of I_i over all of the points, and $\hat{I}_i$ represents the model results. The R^2 of the main stream velocities predicted using the different turbulence models are shown in Table 3.4.

Figure 3.4 displays the comparison of the predicted x direction velocity by the STD k-ε, k-ε RNG, and k-ω (88) models with the PIV measurement at four locations close to the UV lamps inside the reactor. The flow direction and the locations of these four sites are shown in Figure 3.3. The perpendicular distance from the lamp center to the vertical lines in Figure 3.3 is about 5 cm.

Figure 3.4 (a) indicates that the STD k-ε and k-ε RNG models better predict the x direction flow profile at site 1 than k-ω(88) model, although, there is still some minor disagreement between the measurement and the simulated velocity profiles by k-ε and k-ε RNG models. Comparison of the velocity profiles simulated by these three turbulence models at site 1 clearly demonstrate their performance in predicting the spreading rate for far wake free shear flow. The spreading rate is determined as the distance where the velocity defect is half its maximum value. Based on the data shown in Figure 3.4 (a), k-ω(88) model predicted a much higher spreading rate than the STD k-ε and k-ε RNG models as well as the experimental measurement. k-ε RNG yielded a little higher spreading rate value than the STD k-ε model, which explains its closer prediction of the velocity profile to PIV measurement. The results shown in Figure 3.4 (a) is consistent with results reported by Wilcox (98) for the performance of these three turbulence models in two dimensional far wake flows. The relatively small lamp diameter (around 4cm) compared with the length of the lamp (about 50 cm) makes the flow pattern in this study closely resemble a two dimensional flow field.

Figure 3.4 (b) displays a similar pattern as in Figure 3.4 (a), however, the disagreement between the experimental measurement and the predicted results by k-ε and k-ε RNG models is more significant. The difference between the k-ε and k-ε RNG models at site 2 may be due to the flow field interaction with the reactor wall, which is close to site 2. The k-ω(88) model still largely over predicts the spreading rate value than the experimental measurement at site 2. The poorer performance of the

k-ω(88) model compared to the k-ε and k-ε RNG models could be contributed to neglecting cross diffusion term, $\frac{1}{\omega}\frac{\partial k}{\partial x_j}\frac{\partial \omega}{\partial x_j}$. This cross diffusion term can be derived from transforming the ε equation (Equation 5) to the ω equation (Equation 10) by setting the $\varepsilon = C_u k\omega$ (Speziale et al. 1990, Menter 1992, Wilcox 1993, Wilcox 1998). Since the cross-diffusion term is positive in both free shear flows and boundary layers for most of the flows, its primary role is to increase ω and hence reduce the kinetic energy, k. The inclusion of the cross diffusion term can lead to improving the model's performance for predicting free shear flows and reduce the model's performance for predicting boundary layer flows. For the wake flow at sites 1 and 2, the lack of the cross diffusion term in the k-ω(88) model caused it to poorly predict the velocity profile.

Figures 3.4 (c) and (d) present a completely different result of model performance than Figures 3.4 (a) and (b). The velocity profiles predicted by k-ω(88) model agreed well with measurement at the central region of sites 3 and 4 while both the STD k-ε and k-ε RNG models deviated significantly with the PIV data at these locations. As mentioned earlier, the cross diffusion term can cause undesirable effects on the boundary layer, which may impact the results at the central regions of sites 3 and cause undesirable effects due to the upstream flow disturbance at site 4. The disagreement between the simulated velocity profile by k-ε and k-ε RNG models and the experimental measurement is much more significant at the central region of site 4 than at sites 1 and 2. At sites 3 and 4, the omission of the cross diffusion term allowed the k-ω(88) model to

reasonably predict the experimental data, complicating the importance of universally including the cross diffusion term for any model simulation.

It should be noted in Figures 3.4 (c) and (d), that the improved performance of the k-ω(88) model only occurs where the flow field had multiple upstream obstructions. Outside these regions, the flow pattern behaved more like free shear flows. Consequently, the k-ω(88) model deviated significantly from the experimental data in these free shear flow regions and the STD k-ε and k-ε RNG models agreed well with the experimental data.

Figure 3.5 displays a comparison of predicted x direction velocity using the k-ω(98), RSTM, and TFM turbulence models with the experimental measurement at sites (1), (2), (3), and (4). In Figure 3.5 (a), the RSTM agreed well with the experimental velocity data. Comparisons between the RSTM model in Figure 3.5 (a) and the k-ε and k-ε RNG models in Figure 3.4 (a) indicate that RSTM largely improved the predicted velocity profile at the central region, and also maintained a high accuracy at the regions farther away from the lamp center. The better performance of RSTM could be contributed to its ability for predicting the anisotropic Reynolds stress, which might be significant at the central wake regions of the lamp or downstream regions with adverse pressure gradients.

In Figure 3.5 (a), the inclusion of the cross diffusion term allowed the k-ω(98) model to reasonably predict the velocity profile at site 1. However, the disagreement between the k-ω(98) model and the measurement at site 1 is slightly larger than the k-ε

and k-ε RNG models in Figure 3.4 (a). The poorer performance of the k-ω(98) model than the k-ε and k-ε RNG models at site 1 was also shown in Table 3.4. One possible reason for the poorer performance compared to the STD k-ε and k-ε RNG models is that the k-ω(98) uses the revised coefficient f_{β^*} to provide the impact of cross diffusion term on the k equation (Equation 9). The action provided by f_{β^*} does not completely emulate the action of diffusion term described in the ε equation (Equation 5). Consequently, the performance of k-ω(98) model is different with the STD k-ε and k-ε RNG models which have the cross diffusion term directly in their ε equations.

TFM also predicted a reasonable velocity profile at site 1, however, the results at the central regions deviated from the measurement significantly. The velocity profile predicted by TFM at site 1 indicates that TFM slightly over predicted the spreading rate for the far wake flow. The over prediction of the spreading rate by TFM may be due to its empirical constant, C_t , in the momentum exchange term in Table 3.1. This constant was originally calibrated to best fit the velocity profiles for the boundary layer and jet flows (Ilegbusi and Spalding, 1987a, 1987b), however, for the far wake flow, it may be too high, and further investigation is still needed.

In Figure 3.5 (b), the k-ω(98) and RSTM predicted nearly the same velocity profile and agreed well with the experimental data except in the central region. RSTM only showed a slight improvement over the k-ω(98) model as shown in Figure 3.5 (b) as well as the k-ε and k-ε RNG models in Figure 3.4 (b). TFM still slightly over predicted the spreading rate and deviated significantly from the measurement in the

central region.

In Figure 3.5 (c), k-ω(98) and RSTM turbulence models deviated from the measurement at the central region of site 3. As discussed earlier, the central region of site 3 is the location where the flow field is impacted by several upstream obstructions. The poor performance of the k-ω(98) model compared to the k-ω(88) model in this region indicates that the cross diffusion still negatively impacts the k-ω(98) model's velocity prediction.

In Figure 3.5 (d), the TFM model better predicts the velocity profile than both k-ω(98) and RSTM turbulence models. However, RSTM better predicted the flow field than k-ω(98) model at the outer region beyond the cylinder wake (vertical distance > 0.02m). Both the TFM and k-ω(98) displayed a higher spreading rate than the RSTM approach.

Figure 6 displays a comparison of predicted turbulence kinetic energy distributions by k-ε, k-ε RNG, and k-ω(88) models with the experimental data at sites (1), (2), (3), and (4). In Figure 6 (a) and (b), the k-ω(88) model significantly over predicts the experimental kinetic energy value, while the k-ε and k-ε RNG models had closer agreement with the experimental measurement. The poor performance of the k-ω(88) model at site (1) and (2) may be caused by the omission of the cross diffusion term, which can increase the value of ω at the shear flow region, and reduce the results of the kinetic energy (k) by increasing dissipation source term. In Figure 3.6 (c), k-ω(88) model agreed well with the experimental data in the central region due to the lack of the

cross diffusion term. In addition, the lack of cross diffusion term caused the k-ω(88) model to significantly over predict the experimental kinetic energy outside the wake region. Also, at site (3), the disagreement between the STD k-ε and k-ε RNG models and the experiment kinetic energy is larger at the central region than at the outer area. This deviation also confirms the undesirable effect of the cross diffusion term to the complex flow field with several upstream obstruction in the flow. In Figure 3.6 (d), both k-ε and k-ε RNG models under predicted the experimental data while the k-ω(88) model over predicted the experimental data.

Figures 3.7 displays a comparison of the simulation results with the k-ω(98), RSTM, and TFM turbulence models and the experimental kinetic energy at the four sites. The results of k-ω(98) model in Figure 3.7 (a) and (b) clearly indicate the improvement of the kinetic energy compared with the k-ω(88) in Figure 3.6 (a) and (b). However, in Figure 3.7 (c), the disagreement between k-ω(98) model and the measurement are much more significant than k-ω(88) model in Figure 3.6 (c) because of the impact of cross diffusion and the upstream lamp boundary layer. In addition, the RSTM model slightly improved the calculation of kinetic energy at all four sites in Figure 3.7 and predicted better results than the k-ε and k-ε RNG models in Figure 3.6. All three models in Figure 3.7 (d) still had similar problems in predicting the kinetic energy at site 4 as with the models in Figure 3.6 (d).

Figures 3.8 and 3.9 display the comparison of predicted energy dissipation rate by all the turbulence models with the measurement at all four sites. All models were found to

over predict the energy dissipation values. The over prediction of the all turbulence models in this study could be due to the limitation of the PIV measurement in computing the energy dissipation rate. Since the experimental test in this study only measured the flow field in x and z direction, the turbulence energy dissipation rate only included the two dimensional data and neglected the impact from the y direction turbulence characteristics. Data from the missing y direction may have contributed to the lower experimental dissipation rate values.

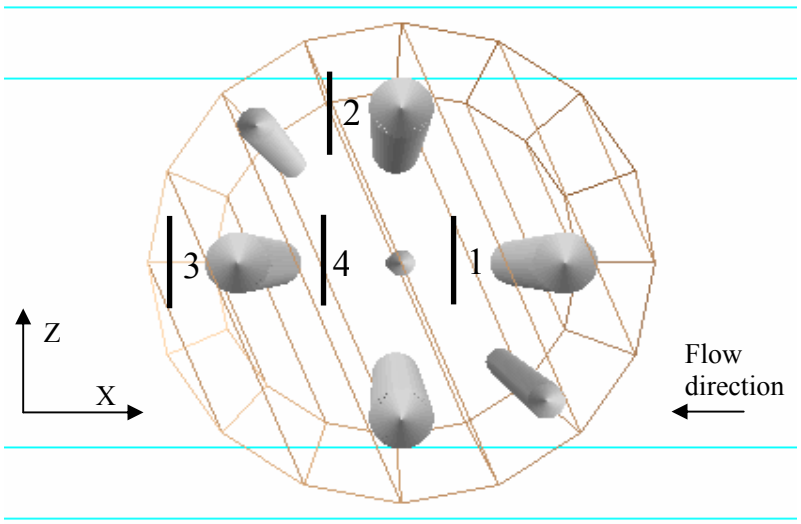

Figure 3.3 the schematic of site locations for flow field comparison

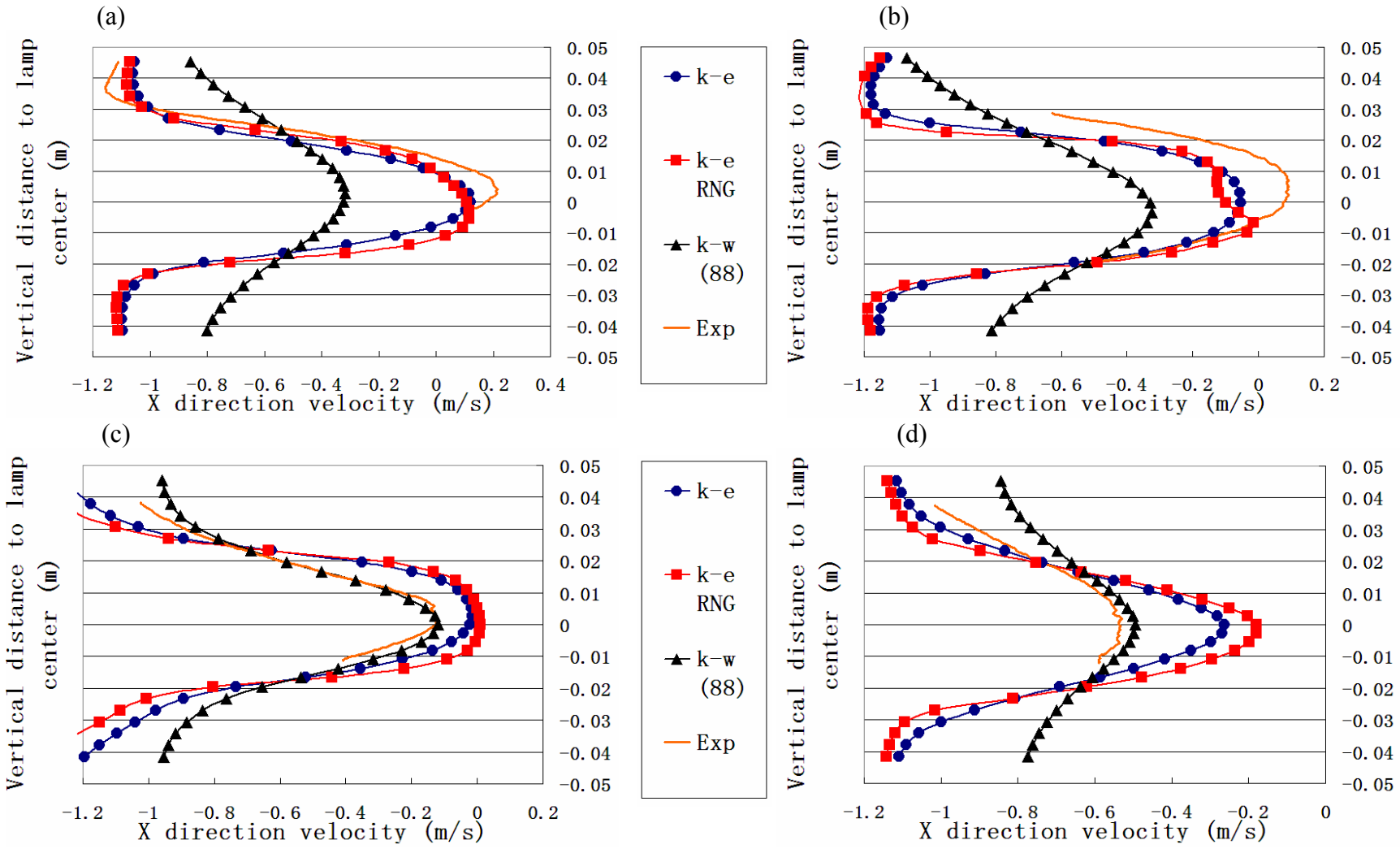

Figure 3.4 Comparison of velocity profile at four sites: (a) site 1, (b) site 2, (c) site 3, (d) site 4

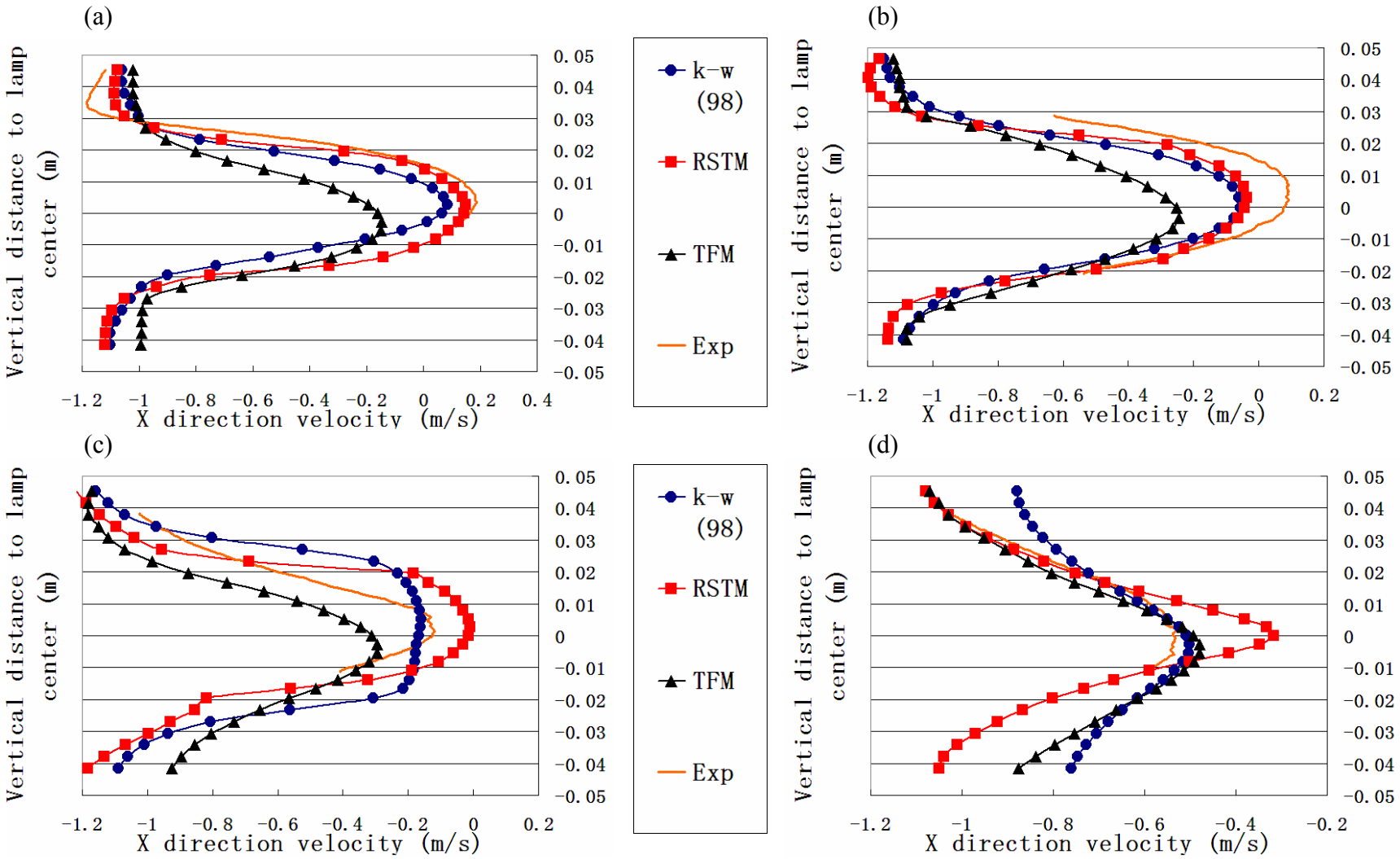

Figure 3.5 Comparison of velocity profile at four sites: (a) site 1, (b) site 2, (c) site 3, (d) site 4

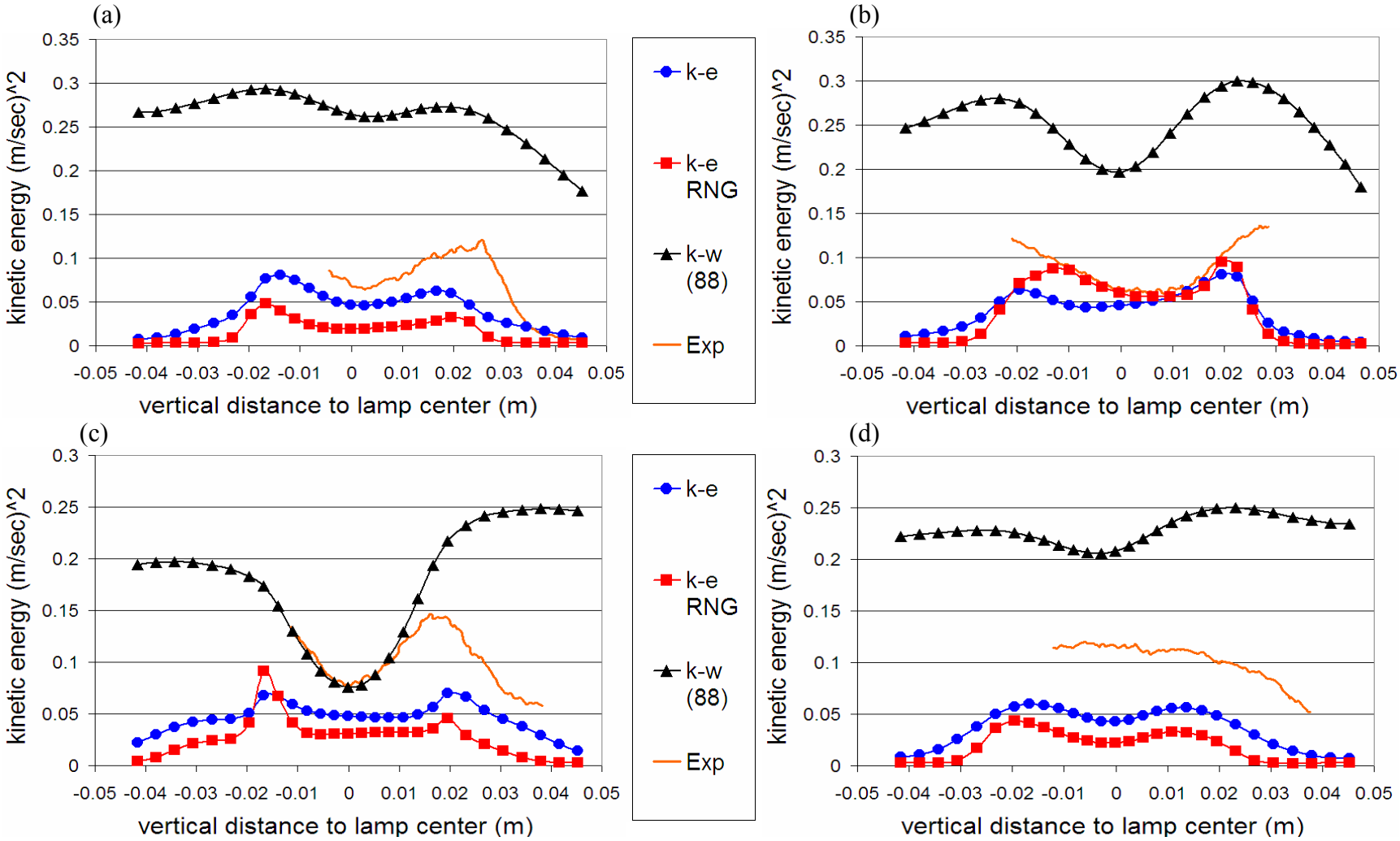

Figure 3.6 Comparison of turbulence kinetic energy at four sites: (a) site 1, (b) site 2, (c) site 3, (d) site 4

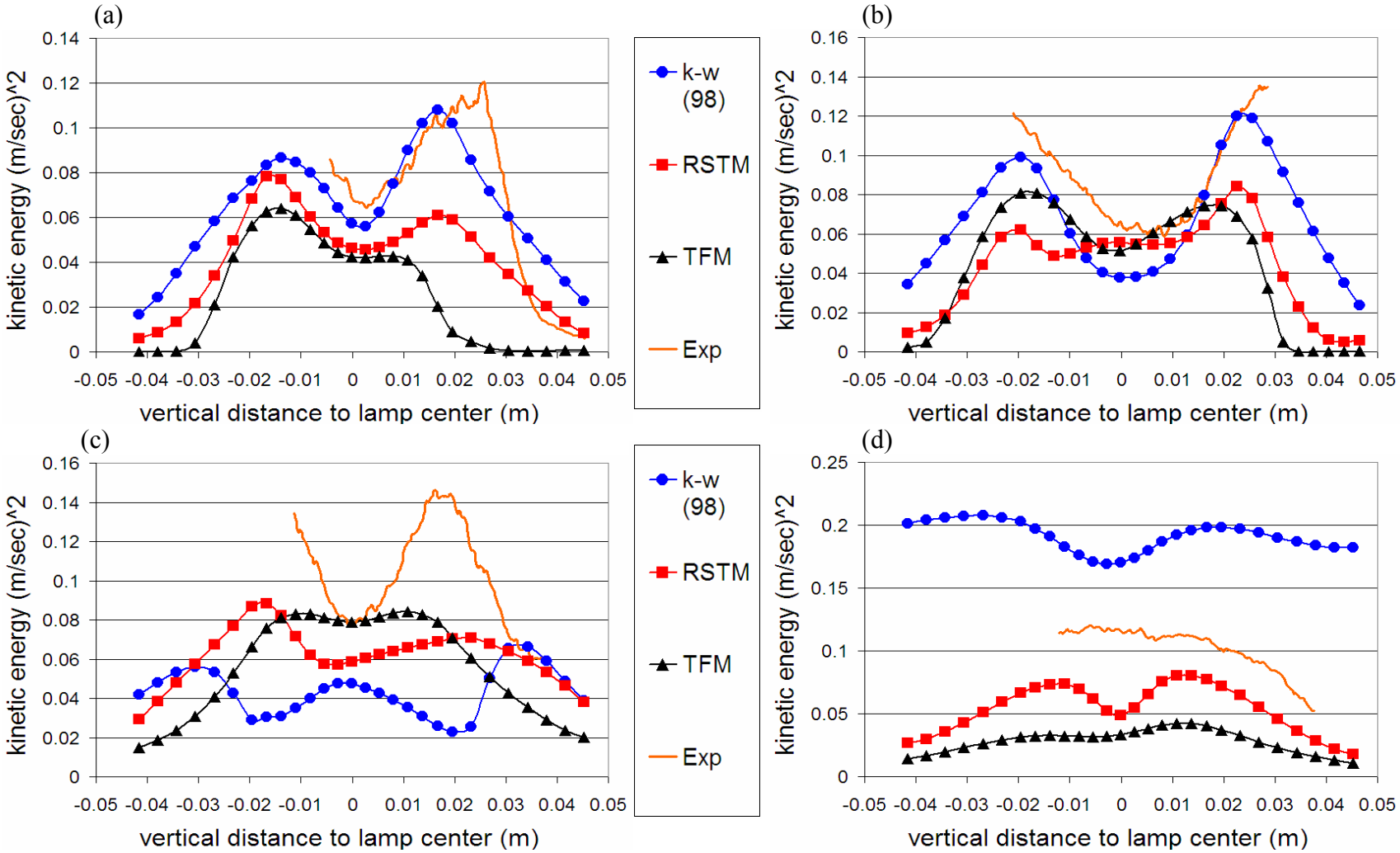

Figure 3.7 Comparison of turbulence kinetic energy at four sites: (a) site 1, (b) site 2, (c) site 3, (d) site 4

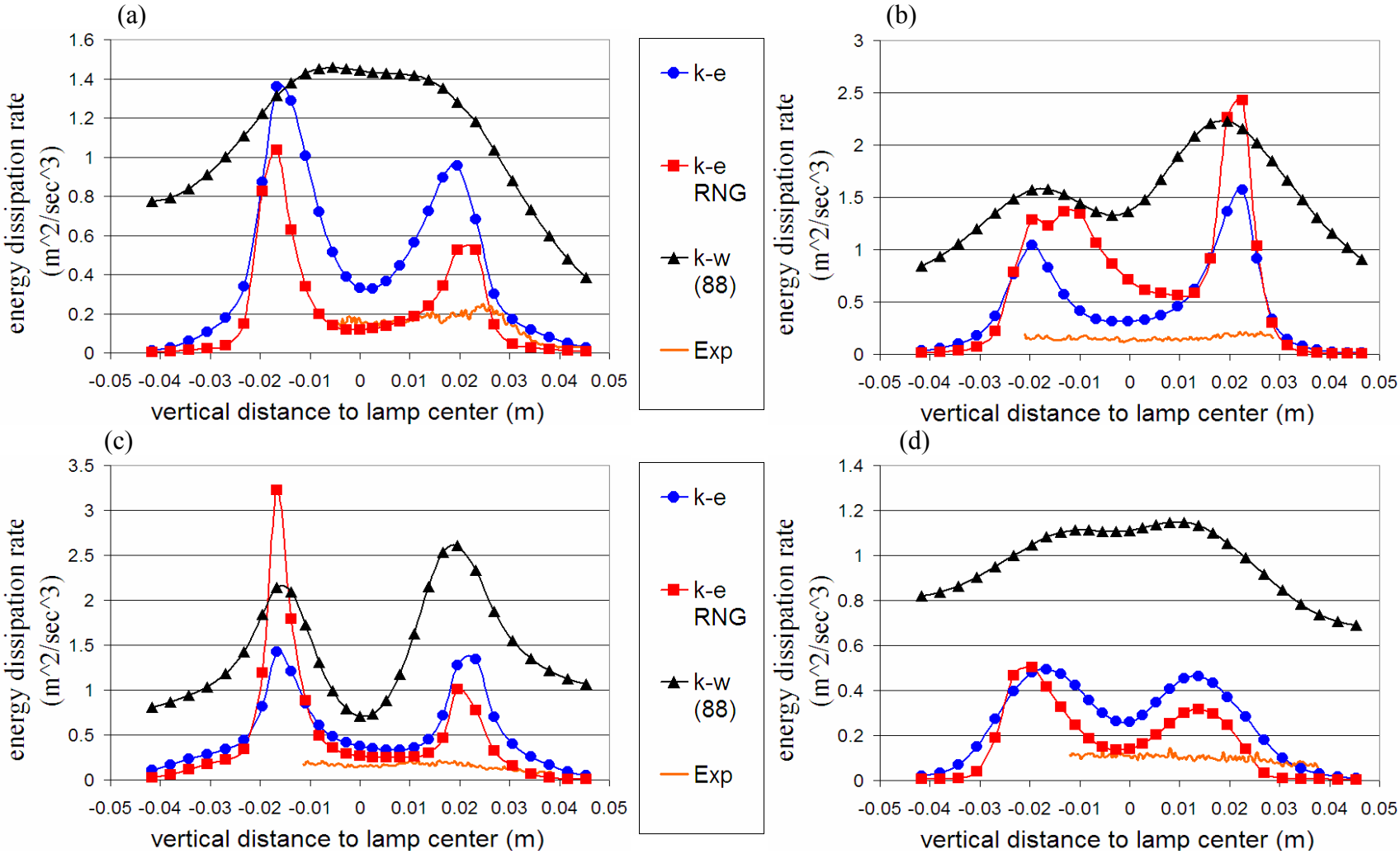

Figure 3.8 Comparison of kinetic energy dissipation rate at four sites: (a) site 1, (b) site 2, (c) site 3, (d) site 4

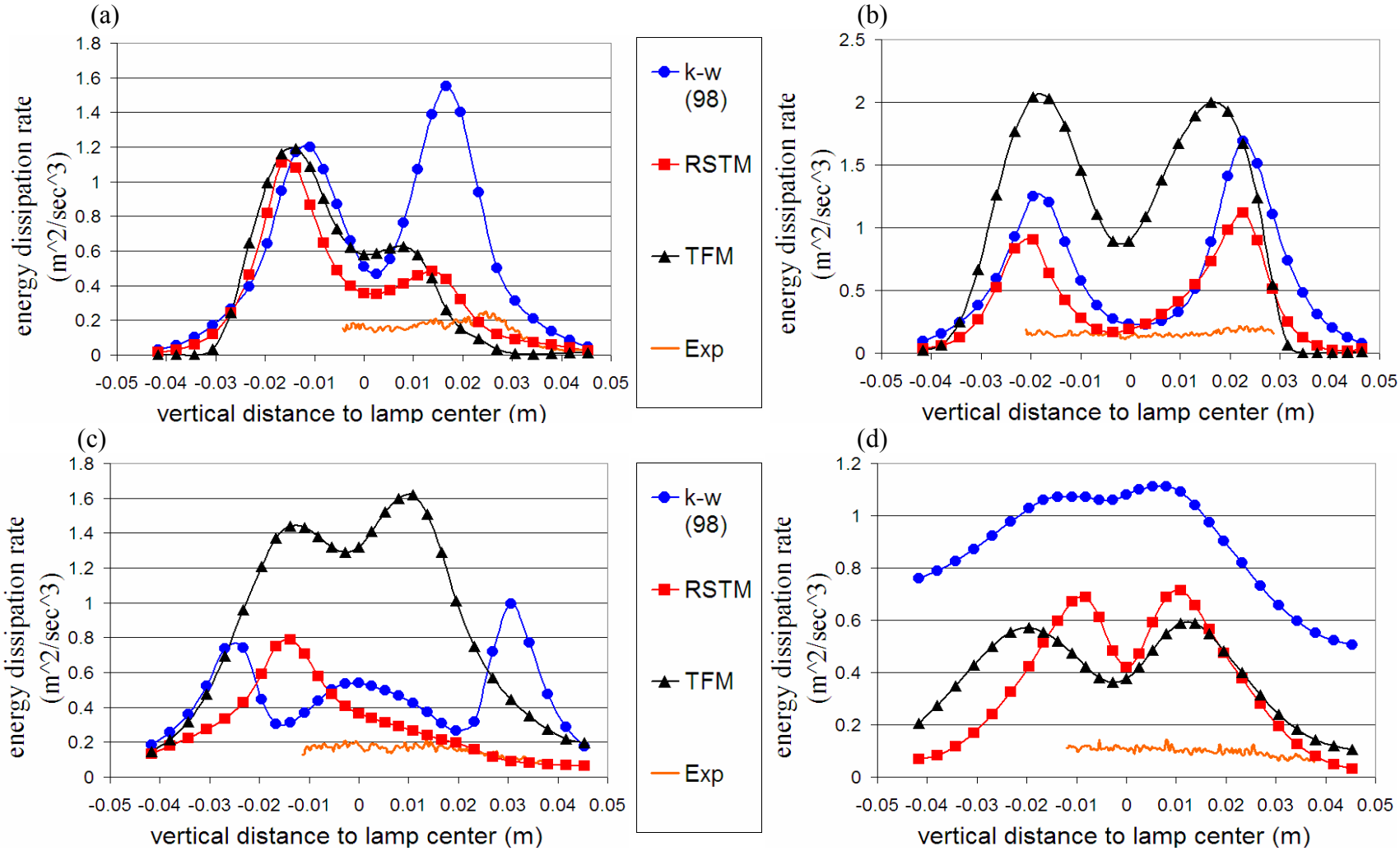

Figure 3.9 Comparison of kinetic energy dissipation rate at four sites: (a) site 1, (b) site 2, (c) site 3, (d) site 4

Table 3.4 R^2 value of the main stream velocity

	k-e	k-e RNG	k-w (88)	k-w (98)	RSTM	TFM
site 1	0.9439	0.9671	0.6402	0.9002	0.9717	0.5098
site 2	< 0	< 0	< 0	0.0942	0.3220	< 0
site 3	0.7079	0.4595	0.9760	0.6465	0.5903	0.4901
site 4	< 0	< 0	0.6875	0.8745	0.4108	0.8693

3.6.2 Impact of turbulence model selection on fluence distribution and microbial inactivation

Figure 3.10 displays the predicted fluence distribution using the different turbulence models with the Lagrangian approach at the lower lamp power condition. To evaluate these figures, the analysis was conducted in three separate fluence ranges, 0 to 20, 20 to 50, and greater than 50 (mJ/cm^2). The first fluence range, 0 to 20, is likely due to transport in regions inside the reactor far from the UV lamps; the second fluence range, 20-50, may represent the transport in regions located around or between UV lamps but not significantly close to the lamp surface; the third fluence range, greater than 50, represents transport in regions significantly close to the UV lamps. In addition, the average fluence and variance about the average fluence were computed and displayed in Figure 3.10. The average fluence and variance were computed as $H'_{avg} = \int_0^\infty E(H')H'dH'$ and $Variance = \int_0^\infty (H' - H'_{avg})^2 H'dH'$, respectively. For the lower lamp power condition, the transport in regions that correspond to the fluence range greater than 50 made up a very small fraction of the total particles released at the reactor inlet.

In Figure 3.10 (a), k-ε and k-ε RNG models exhibit almost the same fluence distribution at all three fluence ranges. The main difference between the STD k-ε and k-ε RNG models is in the magnitude of the peak value located at a fluence value around 40 mJ/cm^2. The STD k-ε and k-ε RNG results in Figure 3.10 (a) indicates that both models predicted similar microbial transport within the UV reactor, which is largely

consistent with the similar flow field and turbulence found in this study. The slightly higher peak value predicted by the k-ε RNG model is caused by the higher main steam (x direction in this study) velocity of the k-ε RNG model as can be seen in Figure 3.4. The higher main stream velocity will reduce the fluence received by the microorganisms and consequently increase the low and medium fluence range in Figure 3.10.

k-ω(88) model also yielded similar fluence distribution with the STD k-ε and k-ε RNG models in the 0 to 20 mJ/cm^2 fluence range. However, the k-ω(88) model predicted a significantly different fluence distribution shape in the 20-50 mJ/cm^2 fluence range, and a higher distribution in the 50-70 mJ/cm^2 fluence range. The lower peak value or the flatter shape of the fluence distribution predicted by k-ω(88) model is related to its much lower main stream velocity comparing with the k-ε and k-ε RNG models as can be seen in Figure 3.4. According to the x direction velocity profile discussion in the earlier section, the k-ω(88) model poorly predicted the flow field in the shear flow region. As discussed earlier, the k-ω(88) displays a higher spreading rate leading to more mixing within the UV reactor and a greater chance for microorganism to receive a higher fluence. This higher fluence level was demonstrated in Figure 3.10 (a) with a lower fraction of microorganisms receiving fluence in the 20 to 50 mJ/cm^2 range, a higher fraction receiving fluences in the range above 50 mJ/cm^2, and a higher variance about the average fluence compared to the STD k-ε and k-ε RNG models.

In Figure 3.10 (b), the k-ω(98), RSTM, and TFM also exhibit similar distribution pattern at the lower and higher fluence region. RSTM predicted a much higher peak value

than the k-ω(98) and TFM around 40 mJ/cm^2. The k-ω(98) was found to predict a significant second peak at the fluence value close to 25 mJ/cm^2. The similarity of the fluence distribution pattern in the lower and higher fluence region is related to the similar flow field predicted by these three models at locations far from and very close to the UV lamps. The difference in the peak values predicted by these three models is associated with their difference in the main stream velocity as shown in Figure 3.5, in which RSTM exhibited a higher main stream velocity than k-ω(98) and TFM, especially in Figure 3.5 (d). The significant second peak predicted by the k-ω(98) model may be caused by higher main stream velocities at other locations in the UV reactor that was not depicted in Figure 3.5, causing an increase in the low fluence range fraction. Compared with the fluence distribution in Figure 3.10 (a), where the fluence distribution was flatter between 20 and 50 mJ/cm^2 for the k-ω(88) model, the improvement in the k-ω(98) is significant as the inclusion of the cross diffusion term allowed the model to resemble the fluence distribution produced by the STD k-ε and k-ε RNG models.

Figure 3.11 displays the fluence distribution predicted by all the different turbulence models at the higher lamp power condition. Compared with the lower lamp power output condition, Figure 3.11 exhibits a broader range of fluences with the peak values shifted to the higher fluence region due to an overall increase of the UV reactor fluence rate. In Figure 3.11 (a), the k-ε RNG model predicted a higher peak value at 150 mJ/cm^2 than both k-ε and k-ω(88) models. Although, the STD k-ε model also predicted a peak at 150 mJ/cm^2, the peak was slightly lower than k-ε RNG. The k-ω(88)

model showed no dominant peak fluence and was essentially flat over a broad fluence range between 90 and 175 mJ/cm^2. The STD k-ε and k-ε RNG models both simulated a more significant second peak at 90 mJ/cm^2 compared with the k-ω(88) model. The prediction of the second peak at 90 mJ/cm^2 is associated with the higher main stream velocity outside the wake region as shown in Figure 3.4. As discussed earlier, the broader and flatter fluence distribution for the k-ω(88) model is due to the greater mixing associated with the high spreading rate.

In Figure 3.11 (b), RSTM still predicted the highest peak value in the fluence distribution, followed by the TFM and the k-ω(98) models. As discussed earlier, k-ω(98) model is still partly impacted by the cross diffusion term that can be seen in Figure 3.5 (c), which displays a higher spreading rate than the experimental results as well as the TFM and RSTM results. However, the k-ω(98) fluence distribution results were similar to the STD k-ε and k-ε RNG results in Figure 3.11 (a). The fluence peak predicted with the TFM approach was slightly shifted to a higher fluence value compared to the RSTM and k-ω(98) model. This shift is likely due to a lower main stream velocity at some locations in the UV reactor.

The predicted microbial inactivation results using the different turbulence models at the low and high lamp power conditions with the three inactivation kinetics are displayed in Table 3.5. For the lower lamp power condition, the microbial inactivation predicted by all the turbulence models increased with the following inactivation kinetic model sequence: 1) Chick-Watson, 2) Cabaj-Sommer (1), 3) Cabaj-Sommer (2). However,

for the higher power output condition, the microbial inactivation increased with the following inactivation kinetic model sequence: 1) Cabaj-Sommer (1), 2) Cabaj-Sommer (2), 3) Chick-Watson. This difference in the order of the inactivation kinetics model can be explained by analyzing the fluence response curve and the fluence distribution curve in Figures 3.1 and 3.10.

In Figure 3.1, the Chick-Watson inactivation kinetics displays a linear response while the Cabaj-Sommer (1) and (2) inactivation kinetics display a higher UV sensitivity at the lower fluence range and a lower UV sensitivity at the higher fluence range. Therefore, the order in the microbial inactivation level seen in Table 3.5 will be determined by the magnitude of the low fluence fraction relative to the high UV response region or the low UV response region of the Cabaj-Sommer model.

In Table 3.5, for low power condition, the microbial inactivation predicted by all the turbulence models have the same sequence for the Chick-Watson and Cabaj-Sommer (1) response kinetics from low to high inactivation as follows: k-ω (88), STD k-ε, k-ε RNG, k- ω (98), TFM, RSTM. However, the inactivation level predicted with Cabaj-Sommer (2) response kinetics exhibited a different sequence, in which k-ω (98) was higher than TFM and STD k-ε was higher than k-ε RNG. As discussed earlier, the different order in the microbial inactivation with Cabaj-Sommer (2) response kinetics is due to the shape of the fluence distribution in Figure 3.10 as it relates to the non-linear UV response kinetics.

Table 3.5 displays the average of the microbial inactivation as well as the 95%

confidence, minimum, and maximum values for the low and high lamp power condition using the three UV response kinetics. For the low power condition, the biggest difference between the minimum and maximum log inactivation from the different turbulence models was found with the Cabaj-Sommer (2) kinetic response model, while the Chick-Watson UV response kinetic model displayed the least difference between the minimum and maximum log inactivation. For the high power condition, the results showed that larger variations in the microbial inactivation due to turbulence model selection was found with the Chick-Watson response kinetic model while both Cabaj-Sommer (1) and (2) yielded nearly the same result for all the turbulence models.

The results in Table 3.5 indicate that the sensitivity of the microbial inactivation due to the turbulence model selection may be influenced not only by the lamp power conditions (or water quality condition since both would influence the fluence distribution) but also significantly affected by the UV response kinetics (or the different microorganisms). Operating conditions or water quality conditions that produce a high log inactivation level may not be sensitive to turbulence model selection if the target microorganisms display significant tailing in the UV response kinetics. However, microorganisms that have linear UV response kinetics (i.e., Chick-Watson), the predicted log inactivation may be sensitive to the turbulence model selection under conditions that produces a high log inactivation. The microbial inactivation sensitivity to the turbulence model selection may increase with increasing slope of the linear UV response kinetics (i.e. microorganisms that are more sensitive to UV).

Under operating conditions that achieve a low effluent inactivation level, the sensitivity of the UV numerical model to the turbulence model selection is also a function of the microbial kinetics response. As can be seen in Table 3.5, a higher sensitivity to the turbulence model selection was found with the Cabaj-Sommer UV kinetic response than the Chick-Watson kinetics. A closer examination of Figure 1 (b) shows that in the fluence region between 10 and 40 mJ/cm^2, the microorganisms with the Cabaj-Sommer UV response kinetics has a greater sensitivity to UV than the microorganism with the Chick-Watson kinetics. Consequently, the difference found in the fluence distribution with the different turbulence models have a greater impact with the higher UV sensitive non-linear kinetics of the Cabaj-Sommer model.

This reverse trend in turbulence model selection sensitivity between the Cabaj-Sommer models and the Chick-Watson with the low lamp power condition compared to the high lamp power condition clearly demonstrates the complexity in determining the importance of selecting the appropriate turbulence model in UV disinfection simulations. The selection of the turbulence model may be further complicated by the reactor geometry and flow rate, both of which were not explored in this study. While other simulations with other reactor geometries have also indicated a slight sensitivity to turbulence model selection (Ducoste and Linden, 2005), simulations with these other reactors were limited in scope and did not involve the range of turbulence models or multiple UV response kinetics over a wide range of log inactivation. The results of this study further suggests the need for model validation with experimental

bioassay data to increase the confidence of the model's ability to predict the UV process performance.

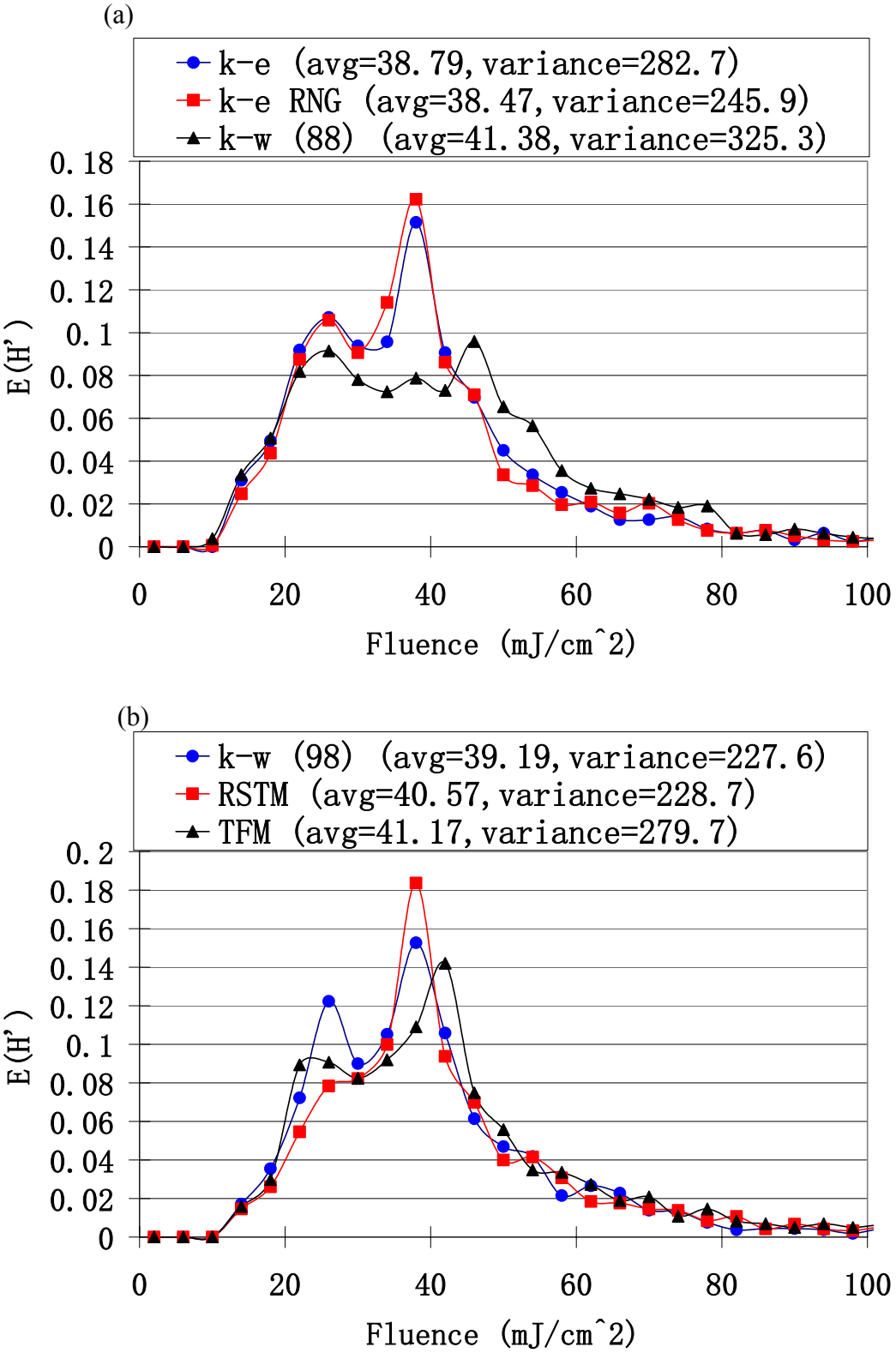

Figure 3.10 Comparison of fluence distribution for low lamp power output condition:
(a) k-e, k-e RNG, and k-w (88) turbulence models
(b) k-w (98), RSTM, and TFM turbulence models

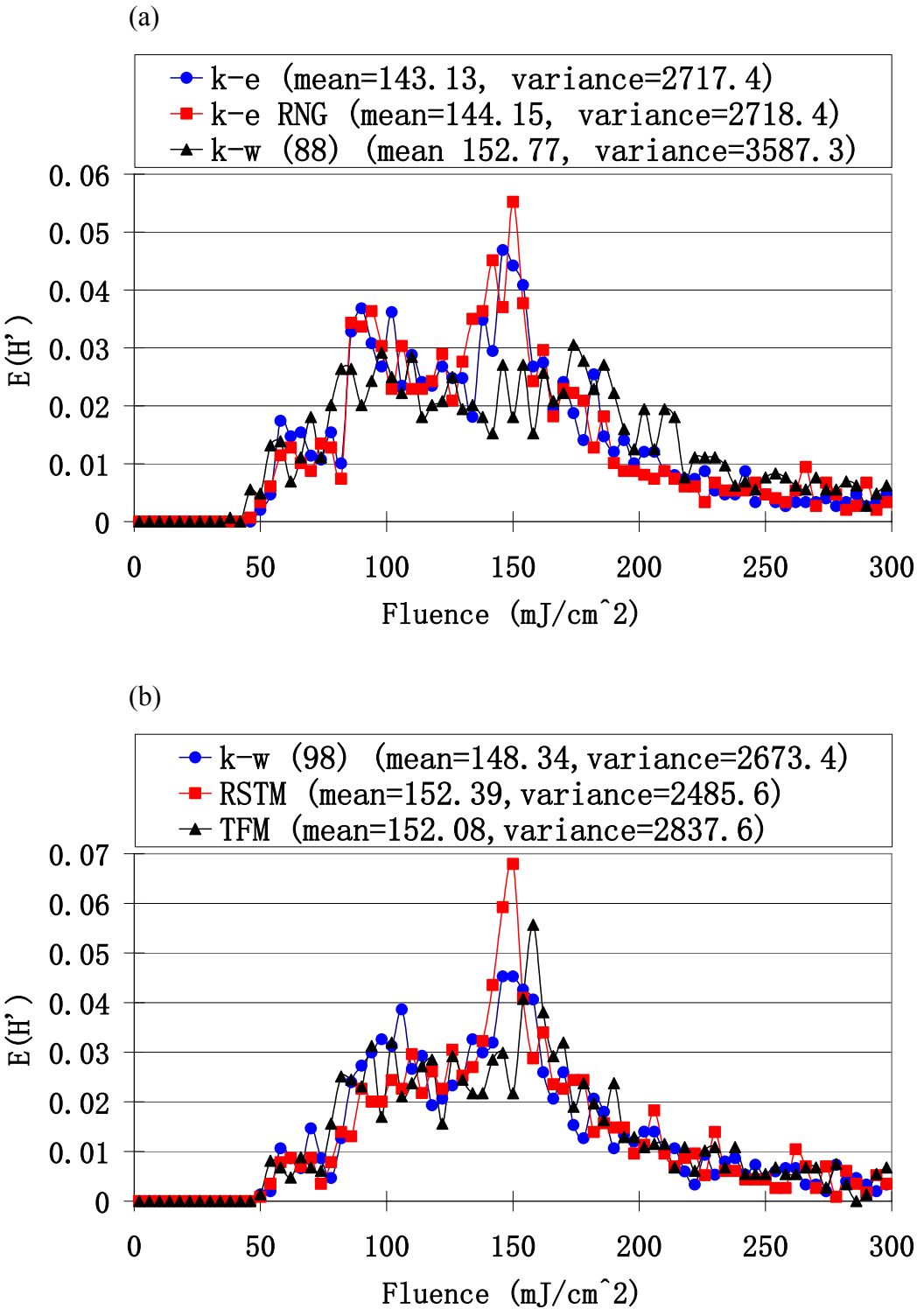

Figure 3.11 Comparison of fluence distribution for high lamp power output condition:
(a) k-e, k-e RNG, and k-w (88) turbulence models
(b) k-w (98), RSTM, and TFM turbulence models

Table 3.5 Results of inactivation reduction (-log(N/N0))

	Lower lamp power			Higher lamp power		
	Chick-Watson	Cabaj-Sommer(1)	Cabaj-Sommer(2)	Chick-Watson	Cabaj-Sommer(1)	Cabaj-Sommer(2)
STD k-e	2.171	2.302	3.348	5.398	3.578	4.648
k-e RNG	2.199	2.334	3.344	5.362	3.579	4.664
k-w (88)	2.162	2.217	3.161	5.065	3.581	4.677
k-w (98)	2.263	2.446	3.483	5.613	3.579	4.698
RSTM	2.317	2.487	3.508	5.631	3.587	4.746
TFM	2.281	2.450	3.476	5.583	3.579	4.710
average	**2.232**	**2.372**	**3.387**	**5.442**	**3.581**	**4.691**
95% confidence	**0.1238**	**0.2041**	**0.2552**	**0.4215**	**0.0065**	**0.0685**
Low	**2.162**	**2.217**	**3.161**	**5.065**	**3.578**	**4.648**
High	**2.317**	**2.487**	**3.508**	**5.631**	**3.587**	**4.746**

3.7 Summary and conclusion for evaluation of turbulence models

This study applied six turbulence models, including STD k-ε, k-ε RNG, k-ω(88), k-ω(98), RSTM, and TFM, to simulate the fluence distribution and the microbial inactivation in a UV disinfection reactor. The simulated fluence distributions produced using the different turbulence models were evaluated at two lamp power conditions (1000 and 3900 Watt). The simulations were also performed with three different UV response kinetics: Chick-Watson simulating MS2 linear inactivation kinetics and two Cabaj-Sommer simulating *B. subtilis* non linear kinetics. The transport of the simulated microorganisms was performed using the Lagrangian based particle tracking approach. The predicted velocity profiles, the turbulent kinetic energy, and the energy dissipation rate at four locations within the reactor were compared with PIV experimental fluid mechanics data. The following conclusions were drawn based on the comparisons and analysis performed in this study.

1. The STD k-ε and k-ε RNG models reasonably predicted the flow field at the far wake flow region. However, the simulated results in wake region near the lamp significantly deviated from the experimental results due to the undesirable effects of the cross diffusion term. The velocity profile predicted by the k-ω(88) model displayed good agreement with the PIV measurement in the wake region near the lamp boundary layer, however, the performance of k-ω(88) model in the far wake region was unacceptable due to the omission of the cross diffusion term.

2. The improvement of k-ω(98) model in the far wake region was significant

compared with the k-ω(88) model. However, the adverse effect of the cross diffusion term in the wake region near the boundary layer was still a factor in limiting its performance. RSTM displayed a slight improvement over the STD k-ε and k-ε RNG models in predicting the far wake flow region. However, the RSTM better predicted the flow field in the wake region near the boundary layer than both the STD k-ε and k-ε RNG models. The TFM had similar results with the STD k-ε, k-ε RNG, k-ω(98) and RSTM in predicting the velocity field outside the wake region. However, inside the wake region near the lamps, the TFM approach deviated from the experimental velocity measurements.

3. The fluence distribution shape was sensitive to the turbulence model selection. Differences in the fluence distribution due to the turbulence model selection included the location and presence of a dominant peak, the spread of the fluence distribution, and the presence of an additional second peak. The presence of a dominant peak and an additional second peak were found with turbulence models that had a tighter wake region with a high main stream velocity (i.e., STD k-ε, k-ε RNG, k-ω(98), TFM). The RSTM also predicted a dominant peak but no secondary peak. The absence of the secondary peak predicted in the low fluence range may be due to better characterization of the anisotropic nature of the turbulent flow field near the wall boundary. The k-ω(88) displayed no dominant or secondary peak and predicted a broad fluence distribution range. The broad fluence distribution range with the k-ω(88) is due to the wider predicted wake region and the lower main stream velocity that enhanced mixing.

4. The sensitivity of effluent microbial inactivation to the turbulence model selection is a function of the UV operating condition and the UV response kinetics of the target microorganisms. The microbial inactivation sensitivity to the turbulence model selection will increase with increasing UV response kinetics and will increase with conditions that promote high log inactivation.

4. Future work

This study investigated two important parts in the numerical simulation of UV disinfection reactors: fluence rate distribution and turbulence models. In the first part, a detailed evaluation of several fluence rate distribution models has been performed. These models include the MPSS, MSSS, UVCalc3D, LSI, RAD-LSI, View Factor, and DO. The models were compared with experimental fluence rate measurements using spherical actinometers, which measure the fluence rate at specific points in space.

In the second part, six turbulence models, including STD k-ε, k-ε RNG, k-ω(88), k-ω(98), RSTM, and TFM, were applied to simulate the fluence distribution and the microbial inactivation in a UV disinfection reactor. The turbulence models were performed with three inactivation kinetic functions and at two lamp power output condition. The predicted main stream velocity profiles, the turbulent kinetic energy, and the energy dissipation rate at four locations within the reactor were compared with the PIV experimental fluid mechanics data. In addition, the simulated fluence distributions produced using the different turbulence models were evaluated at two lamp power output

conditions. The simulation were also performed with three different UV response kinetics: Chick-Watson simulating MS2 linear inactivation kinetics and two Cabaj-Sommer simulating *B. subtilis* non linear kinetics.

While the results of this study will be helpful to the drinking water community who are interested in using numerical models to understand and design the disinfection process, there are several research topics that still need to be performed. First, the particle scattering was neglected in this study. Part of the future work should focus on the inclusion of particle scattering into the MSSS based fluence rate distribution model since particle scattering may be significant in the UV disinfection process for wastewater treatment or for unfiltered water sources. Second, this study also neglected the shadowing effects of internal walls and reflection of the reactor walls. These effects may impact the simulation results significantly under conditions of high water quality or high lamp power. In addition, the predicted fluence distribution and effluent inactivation using the different turbulence models were not compared with the bioassay experimental measurement in this study. This comparison can directly and more precisely determine the performance of different turbulence models. Further more, this study only investigated one reactor geometry and flow rate. Different reactor geometries and flow rates could affect the sensitivity of the effluent inactivation and fluence distribution to the turbulence model selection.

Reference:

Baas, M.M., 1996, Latest Advances in UV Disinfection Hydrodynamic Simulation and Relation to Practical Experiences, *Proceedings AQUATECH*, Amsterdam.

Blatchley, III E. R., 1997, Numerical modeling of UV intensity: application to collimated-beam reactors and continuous-flow systems. *Water Res.* 31, 2205-2218.

Bolton, J. R., B. Dussert, Z. Bukhari, T. Hargy, and J. L. Clancy, 1998, Inactivation of *Cryptosporidium Parvum* by Medium-Pressure Ultraviolet Light in Finished Drinking Water, *Proc*. *AWWA 1998 Annual Conference*, Dallas, TX, Vol. A, pp 389-403.

Bolton, J. R., 2000, Calculation of ultraviolet fluence rate distribution in an annular reactor: significance of refraction and reflection, *Water Res.* Vol. 34, No.13, pp. 3315-3324.

Bolton, J. R., 2002, *Personal Communication.*

Bolton, J. R., 2003, *Personal Communication.*

Bukhari, Z., T. M. Hargy, J. R. Bolton, B. Dussert and J. L. Clancy, 1999, Medium Pressure UV Light for Oocyst Inactivation, *J. AWWA*, 91, 86-94

Buffle, M.O., Chiu, K., Taghipour, F., 2000, Reactor conceptualization and performance optimization with computational modeling, *Proceedings WEF Specialty Conference on Disinfection*, New Orleans, LA

Cabaj, A., Sommer, R., 2000, Measurement of Ultraviolet Radiation with Biological Dosemeters, *Radiation Protection Dosimetry*, Vol. 91, Nos 1-3, pp. 139-142.

Chia-Jung, HSU, 1967, Shape factor equations for radiant heat transfer between two arbitrary sizes of rectangular planes, *The Canadian Journal of Chemical Engineering,* Vol. 45, Feb.,1967.

Chiu, K., Lyn, D.A., Savoye, P., Blatchley III, E.R., 1999a, Integrated UV Disinfection Model Based on Particle Tracking, *Journal of Environmental Engineering ASCE*, Vol.125, No.1, pp.7-16

Chiu, K., Lyn, D.A., Savoye, P., Blatchley III, E.R., 1999b, Effect of UV System Modifications on Disinfection Performance, *Journal of Environmental Engineering ASCE*, Vol.125, No.5, pp.459-469

Choudhury, D., Kim, S.E., Flannery, W.S., 1993, Calculation of turbulent separated flows using a renormalization group based k-ε turbulence model. *Flows ASME FED,* Vol. 149, pp. 77-87

Craik, S. A., Weldon, D., Finch, G. R., Bolton, J. R. and Belosevic, M., 2001, Inactivation of *Cryptosporidium Parvum* oocysts using medium-and low-pressure ultraviolet radiation, *Wat. Res*. 35(6), 1387-1398.

Daley, B.J. and Harlow, F.H., 1970, Transport equations of turbulence, *Phys.Fluids*, Vol.13, p2634.

Do-Quang, Z., Janex, M.L., Perrin, D., 2002, Predictive tool for UV dose distribution

assessment: Validation of CFD models by bioassays, *Proceedings AWWA National Convention*, New Orleans, LA

Downey, D., Giles, D.K., Delwiche, M.J., 1998, Finite element analysis of particle and liquid flow through an ultraviolet reactor, *Computers and Electronics in Agriculture*, Vol.21, pg 81

Ducoste, J.J., D., Liu, K., Linden, 2005, Alternative Approaches to Modeling Dose Distribution and Microbial Inactivation in Ultraviolet Reactors: Lagrangian vs Eulerian, Submitted to *Journal Environmental Engineering, ASCE.*

Fiveland, W. A. (1984) Discrete-Ordinates solutions of the radiative transport equation for rectangular enclosures, *Journal of Heat Transfer,* Nov. 1984, Vol.106, pp.699-705.

Gyurek, L. L., and Finch, G. R., 1998, Modeling water treatment chemical disinfection kinetics, *Journal of environmental engineering-ASCE,* Vol. 124 No.9, pp. 783-793

Ilegbusi, O. J., and Spalding, D. B., 1987a, A Two-Fluid model of turbulence and its application to near-wall flows, *PhysicoChemical Hydrodynamics*, Vol.9, No.1/2, pp.127-160.

Ilegbusi, O. J., and Spalding, D. B., 1987b, Application of a two-fluid model of turbulence to turbulent flows in conduits and free shear-layers, *PhysicoChemical Hydrodynamics*, Vol.9, No.1/2, pp.161-181.

Ilegbusi, O.J., and Spalding, D.B., 1989, Prediction of fluid flow and heat transfer characteristics of turbulent shear flows with a two-fluid model of turbulence, *Int. J. Heat Mass Transfer.* Vol.32, No.4, pp. 767-774.

Ilegbusi, O.J., 1994, Application of the two-fluid model of turbulence to tundish problems, ISI J International, Vol. 34, No.9., pp.732-738

Jacob, S. M. and Dranoff, J. S., 1970, Light intensity profiles in a perfectly mixed photoreactor. *A.I.C.H.E. J.* Vol.16, pp.359-363.

Knut Stamnes, S-Chee Tsay, Warren Wiscombe, and Kolf Jayaweera, 1988, Numerically stable algorithm for discrete-ordinate-method radiative transfer in multiple scattering and emitting layered media, *Applied Optics*, Vol.27, No.12, pp. 2502-2509.

Kowalski, W. J., Bahnfleth, W. P., 2000, Effective UVGI system design through improved modeling, ASHRAE Transactions, 106(2), pp 4-15.

Launder B.E. and Spalding D.B., 1974, The numerical computation of turbulent flows, *Comp. Math. in Appl. Mech. & Eng*, Vol.3, pp269.

Launder, B.E., 1989a, Second-moment closure: present and future?, *Int.J.Heat Fluid Flow*, Vol.10, No.4, p282.

Launder, B.E., 1989b, Second-moment closure and its use in modelling turbulent industrial flows, *Int.J.Num.Methods in Fluids*, Vol.9, p963.

Leschziner, M.A., 1990, Modelling engineering flows with Reynolds stress turbulence closure, *J.Wind Engng & Industrial Aerodynamics*, Vol.35, p21.

Linden, K.G. and A.A. Mofidi., 1999, Measurement of UV irradiance: tools and considerations, Proceedings, Water Quality Technology Conference, AWWA, Tampa Bay, FL. Nov. 1-3.

Linden, K. G., Shin, G., Faubert, G., Cairns, W., Sobsey, M. D., 2002, UV Disinfection of Giardia lamblia Cysts in Water, *Environ. Sci. Technol*., 36(11), 2519-2522.

Linden, Karl, 2004, personal communication.

Liou B. T. and Wu C. Y., 1996, Radiative transfer in a multi-layer medium with fresnel interfaces, *Heat and Mass Transfer,* Vol.32, pp.103-107.

Liu, D., Ducoste, J.J., Jin, S.S., Linden, K., 2004, Evaluation of Alternative Fluence Rate Distribution Models, *Journal of Water Supply: Research and Technology AQUA*, Vol.53, pp. 391-408.

Lyn, D.A., Chiu, K., Blatchley, E.R., 1999, Numerical Modeling of Flow and Disinfection in UV Disinfection Channels, *Journal Env. Eng*. ASCE, 125(1), pg 17.

Malin, M.R. and Spalding, D.B., 1984, A two-fluid model of turbulence and its application to heated plane jets and wakes, *PhysicoChemical Hydrodynamics*, Vol.5, No.5/6, pp.339-362

Menter F. R., 1992, Improved two-equation k-omega turbulence model for aerodynamic flows, NASA TM-103975

Menter, F.R., 1994, Two-Equation eddy-viscosity turbulence models for engineering applications. *AIAA J.*, Vol.32, pp.1598-1605.

Meyer-Arendt J. R., 1984, *Introduction to Classical and Modern Optics,* 2nd ed. Prentice-Hall, Englewood cliffs, NJ, pp.300-302.

Modest, M. F., 1993, *Radiative Heat Transfer.* McGraw-Hill, New York.

Neofotistos, P., Do-Quang, Z., Perrin, D., 2002, Ultraviolet Light: CFD Modeling Overlay with Fluence Rate Modeling as a Predictor of Reactor Performance for Drinking Water UV systems, *Proceedings AWWA National Convention*, New Orleans, LA

Norberto Fueyo, 1989, Two fluid models of turbulence for axi-symmetrical jets and sprays, PhD thesis, Imperial College, London

Petri, B.M., Olson, D.A., 2002, Bioassay Validation of Computational Disinfection Models Used for UV Reactor Design and Scaleup, *Proceedings Disinfection: Health and Safety Achieved Through Disinfection WEF*, Orlando, FL.

Raffel, M., Christian, E. W., Kompenhans, J., 1998, Particle image velocimetry: a practical guide, Berlin, New York, Springer.

Rahn, R.O., 1997, Potassium Iodide as a Chemical Actinometer for 254 nm Radiation: Use of Iodate as an Electron Scavenger, *Photochemistry and Photobiology*, 66(4), pg 450.

Rahn, R. O., Xu, P. and Miller, S. L. (1999). Dosimetry of room – air germicidal (254 nm) radiation using spherical actinometry. *Photochem. Photobiol*. **70**(3)**,** 314 – 318.

Rahn, R. O., Stefan, M. I. and Bolton, J. R., 2000, The Iodide/Iodate Actinometer in UV Disinfection: Characteristics and Use in the Determination of the Fluence Rate Distribution in UV Reactors, in *Proc.* Water Quality Technology Conference, Nov. 2000, Salt Lake City, UT. CD/ROM published by the American Water Works Association, 6666 West Quincy Ave., Denver, CO 80235

Rahn, R. O. (2003) Measurement of germicidal UV fluence rates by means of longitudinal actinometry: application to upper – room UV disinfection. Personal communication.

Rokjer, D., Valade, M., Keesler, D., Borsykowsky M., 2002, Computer modeling of UV reactors for validation purposes, *Proceedings AWWA WQTC*, seattle, WA

Rudnick, S. (2001). Predicting the ultraviolet radiation distribution in a room with multilouvered germicidal fixtures. *AIHA J*. **62**, 434 –445

Smith, L.M., Yakhot, V., 1993, Short and long time behavior of eddy-viscosity models, *Theoretical Computer Fluid Dynamics*, Vol.4, pp. 197-207

Sommer, R., Cabaj, A., Sandu, T. and Lhotsky, M. (1999) Measurement of UV radiation using suspensions of micororganisms, *J. Photochem. Photobiol. B: Biol.* **53**, 1 –6.

Spalding, D. B., 1983, Chemical reaction in turbulent fluids, *International Journal of Physicochemical Hydrodynamics*, Vol.4. No.4. pp.323-336

Speziale C.G., Abid R. and Anderson E.C., 1990, A critical evaluation of two-equation turbulence models for near-wall turbulence, AIAA Paper 90-1481.

Speziale, C.G., Gatski, T.B., Fitzmaurice, N., 1991, An analysis of RNG based turbulence models for homogeneous shear flows. *Phys. Fluids A*, 3:2278-80

Speziale, C. G., Sarkar, S. and Gatski, T. B.,1991, Modeling the pressure-strain correlation of turbulence, *Journal of Fluid Mechanics*, Vol.227, pp.245-272.

Stefan, M. I., Rahn, R. O. and Bolton, J. R., 2001, Use of the iodide/iodate actinometer together with spherical cells for determination of the fluence rate distribution in UV reactors: validation of the mathematical model. *Proc. 1st Intnl. Congr. Ultraviolet Technol.,* CDROM, International Ultraviolet Association, Washington DC, June.

Tarald, O. Kvalseth, 1985, Cautionary Note About R^2, *The American Statistician,* Nov. 1985, Vol.39, No.4 (Pt.1), pg 279-285.

Wilcox, D.C., 1988, Reassessment of the scale determining equation for advanced turbulence models, *AIAA J.*, Vol. 26, No.11, pp.1299-1310

Wilcox, D.C., 1993, Comparison of two-equation turbulence models for boundary layers with pressure gradient, *AIAA J.*, Vol. 32, No.8, pp.1414-1421

Wilcox, D.C., 1998, Turbulence modeling for CFD, DCW industries.

Wu, C.H., Yao, A., and Chang, K.A., DPIV measurements of unsteady deep-water wave

breaking on following currents, PIV and Modeling Water Wave Phenomena, World Scientific Publication Co., Advances in Coastal and Ocean Engineering, Vol.9, ISBN:9812389148, 2004.

Yakhot, V. and Orszag, S. A. (1986), Renormalization Group Analysis of turbulence: 1. Basic theory, *Journal of Scientific Computing*, Vol.1, pp.3-51.

Yakhot, V., Orszag, S. A., Thangam, S., Gatski, T. B. and Speziale, C. G. (1992), Development of Turbulence Models for Shear Flows by a Double Expansion Technique, *Physics of Fluids A*, Vol.4, pp.1510-1520.

Appendices A
The Q1 file for the MSSS fluence rate distribution model.

```
TALK=T;RUN( 1, 1)
*************************************************************
    Q1 created by VDI menu, Version 3.4, Date 10/08/01
 CPVNAM=VDI;SPPNAM=Core
*************************************************************
  Echo DISPLAY / USE settings
 *************************************************************
 IRUNN     =            1 ;LIBREF =            0
 *************************************************************
  Group 1. Run Title
 TEXT(UVMAX STRAIGHT 14.5GPM    UVT776                )
 *************************************************************
  Group 2. Transience
 STEADY    =       T
 *************************************************************
  Groups 3, 4, 5    Grid Information
     * Overall number of cells, RSET(M,NX,NY,NZ,tolerance)
 RSET(M,91,91,25)
     * Set overall domain extent:
     *              xulast    yvlast    zwlast
                  name
 XSI= 6.350000E-01; YSI= 4.200000E-01; ZSI= 5.080000E-01
 RSET(D,CHAM       )
 *************************************************************
  Group 6. Body-Fitted coordinates
 *************************************************************
  Group 7. Variables: STOREd,SOLVEd,NAMEd
 ONEPHS    =       T
     * Non-default variable names
 NAME(148) =PRPS ; NAME(149) =HH1
 NAME(150) =RR1
     * Solved variables list
 SOLVE(C1    )
     * Stored variables list
 STORE(RR1 ,HH1 ,PRPS)
     * Additional solver options
 SOLUTN(C1    ,Y,Y,Y,N,N,Y)
```

```
************************************************************
 Group 8. Terms & Devices
TERMS (C1    ,Y,N,N,N,Y,N)
************************************************************
 Group 9. Properties
SETPRPS(1,111)
RHO1        = 7.800000E+03
PRESS0    = 1.000000E+05
TEMP0      = 2.730000E+02
CP1          = 4.730000E+02
ENUL        = 0.000000E+00 ;ENUT      = 0.000000E+00
DRH1DP    = 2.000000E+11
DVO1DT    = 3.700000E-06
************************************************************
 Group 10.Inter-Phase Transfer Processes
************************************************************
 Echo PLANT settings
  PLANTBEGIN
  <SC0901> RR1=((XG2D-RG(1))**2.+(YG2D-RG(2))**2.)**0.5         +TINY
  REGION(1,NX,1,NY,1,NZ)

  <SC0905> HH1=-(ZGNZ-RG(9)+TINY)
  REGION(1,NX,1,NY,1,NZ)

 PATCH(IRR1,VOLUME,1,NX,1,NY,1,NZ,1,LSTEP)
  <SORC45> VAL=RG(14)*RG(18)/(4.*RG(81)*RG(10)*RR1)*(ATAN((RG(10)/$
2.+HH1)/RR1)+ATAN((RG(10)/2.-HH1)/RR1))
 COVAL(IRR1,C1,FIXVAL,GRND)

  PLANTEND
************************************************************
 Group 11.Initialise Var/Porosity Fields
  No PATCHes used for this Group
INIADD   =       F
************************************************************
 Group 12. Convection and diffusion adjustments
  No PATCHes used for this Group
************************************************************
 Group 13. Boundary & Special Sources
  No PATCHes used for this Group
```

```
************************************************************
 Group 14. Downstream Pressure For PARAB
************************************************************
 Group 15. Terminate Sweeps
LSWEEP   =          10
RESREF(C1    ) =    1.000000E-02
SELREF   =       F
************************************************************
 Group 16. Terminate Iterations
ENDIT (C1    ) =    1.000000E-10
************************************************************
 Group 17. Relaxation
RELAX(C1    ,FALSDT, 1.000000E+03)
************************************************************
 Group 18. Limits
VARMAX(C1    ) = 1.000000E+05 ;VARMIN(C1    ) = 1.000000E-20
************************************************************
 Group 19. EARTH Calls To GROUND Station
USEGRD   =       T    ;USEGRX =       T
NAMSAT   =MOSG
ASAP       =       T
RADIA      = 0.000000E+00 ;RADIB    = 0.000000E+00
EMISS      = 0.000000E+00
RG(    1) = 3.175000E-01
RG(    2) = 2.100000E-01
RG(    9) = 2.250000E-01
RG( 10) = 1.780000E-01
RG( 11) = 1.850000E-02
RG( 12) = 1.372000E+00
RG( 13) = 1.516000E+00
RG( 14) = 1.017000E+01
RG( 18) = 3.281000E-01
RG( 19) = 1.000000E-04
RG( 20) = 1.196000E-02
RG( 21) = 8.800000E-01
RG( 41) = 1.000000E+00
RG( 61) = 1.000000E+00
RG( 81) = 3.141593E+00
RG( 82) = 1.000000E+00
RG( 83) = 1.500000E-03
RG( 84) = 1.000000E+00
```

```
 RG( 85) = 8.500000E-01
 ************************************************************
  Group 20. Preliminary Printout
 ECHO       =       T
 ************************************************************
  Group 21. Print-out of Variables
 ************************************************************
  Group 22. Monitor Print-Out
 IXMON     =          40 ;IYMON    =          50 ;IZMON    =           1
 NPRMON    =    100000
 NPRMNT    =           1
 TSTSWP    =          -1
 ************************************************************
  Group 23.Field Print-Out & Plot Control
 NPRINT    =    100000
 ISWPRF    =           1 ;ISWPRL =    100000
    No PATCHes used for this Group
 ************************************************************
  Group 24. Dumps For Restarts
 NOWIPE    =       T

 GVIEW(P,0.000000E+00,-1.000000E+00,0.000000E+00)
 GVIEW(UP,0.000000E+00,0.000000E+00,1.000000E+00)

> DOM,       SIZE,            6.350000E-01, 4.200000E-01, 5.080000E-01
> DOM,       MONIT,            3.105770E-01, 2.146150E-01, 5.700000E-02
> DOM,       SCALE,            1.000000E+00, 1.000000E+00, 1.000000E+00
> DOM,       SNAPSIZE,         1.000000E-02
> GRID,      RSET_X_2,        -29, 1.200000E+00
> GRID,      RSET_X_3,          9, 1.000000E+00
> GRID,      RSET_X_4,         13, 1.000000E+00
> GRID,      RSET_X_5,          9, 1.000000E+00
> GRID,      RSET_X_6,        -29, 1.200000E+00
> GRID,      RSET_Y_2,        -29, 1.200000E+00
> GRID,      RSET_Y_3,          9, 1.000000E+00
> GRID,      RSET_Y_4,         13, 1.000000E+00
> GRID,      RSET_Y_5,          9, 1.000000E+00
> GRID,      RSET_Y_6,        -29, 1.200000E+00
> GRID,      RSET_Z_3,         21, 1.000000E+00
> DOM,        RELAX,            5.000000E-01
```

```
> OBJ1,     NAME,             DOMBLK
> OBJ1,     POSITION,       0.000000E+00, 0.000000E+00, 0.000000E+00
> OBJ1,     SIZE,             6.350000E-01, 4.200000E-01, 5.080000E-01
> OBJ1,     CLIPART,        cube14
> OBJ1,     ROTATION24,           1
> OBJ1,     VISIBLE,      -1.000000E+00
> OBJ1,     TYPE,             BLOCKAGE
> OBJ1,     MATERIAL,          198
> OBJ1,     ADIABATIC_W,     0.000000E+00, 0.000000E+00
> OBJ1,     ADIABATIC_E,     0.000000E+00, 0.000000E+00
> OBJ1,     ADIABATIC_S,     0.000000E+00, 0.000000E+00
> OBJ1,     ADIABATIC_N,     0.000000E+00, 0.000000E+00
> OBJ1,     ADIABATIC_L,     0.000000E+00, 0.000000E+00
> OBJ1,     ADIABATIC_H,     0.000000E+00, 0.000000E+00

> OBJ2,     NAME,             REACTOR
> OBJ2,     POSITION,       1.950000E-01, 8.750000E-02, 1.360000E-01
> OBJ2,     SIZE,             2.450000E-01, 2.450000E-01, 1.780000E-01
> OBJ2,     CLIPART,        cylinder
> OBJ2,     ROTATION24,           1
> OBJ2,     TYPE,             BLOCKAGE
> OBJ2,     MATERIAL,          67
> OBJ2,     ADIABATIC,       0.000000E+00, 0.000000E+00
> OBJ2,     SCAL_FIXF,       1.000000E+00

> OBJ3,     NAME,             SLEEVE
> OBJ3,     POSITION,       2.990000E-01, 1.915000E-01, 1.360000E-01
> OBJ3,     SIZE,             3.700000E-02, 3.700000E-02, 1.780000E-01
> OBJ3,     CLIPART,        cylinder
> OBJ3,     ROTATION24,           1
> OBJ3,     TYPE,             BLOCKAGE
> OBJ3,     MATERIAL,          198
> OBJ3,     ADIABATIC_W,     0.000000E+00, 0.000000E+00
> OBJ3,     ADIABATIC_E,     0.000000E+00, 0.000000E+00
> OBJ3,     ADIABATIC_S,     0.000000E+00, 0.000000E+00
> OBJ3,     ADIABATIC_N,     0.000000E+00, 0.000000E+00
> OBJ3,     ADIABATIC_L,     0.000000E+00, 0.000000E+00
> OBJ3,     ADIABATIC_H,     0.000000E+00, 0.000000E+00

> OBJ4,     NAME,             LPLAMP
> OBJ4,     POSITION,       3.100000E-01, 2.025000E-01, 1.140000E-01
```

```
> OBJ4,     SIZE,              1.500000E-02, 1.500000E-02, 2.800000E-01
> OBJ4,     CLIPART,           cylinder
> OBJ4,     ROTATION24,              1
> OBJ4,     TYPE,              BLOCKAGE
> OBJ4,     MATERIAL,          198
> OBJ4,     ADIABATIC_W,       0.000000E+00, 0.000000E+00
> OBJ4,     ADIABATIC_E,       0.000000E+00, 0.000000E+00
> OBJ4,     ADIABATIC_S,       0.000000E+00, 0.000000E+00
> OBJ4,     ADIABATIC_N,       0.000000E+00, 0.000000E+00
> OBJ4,     ADIABATIC_L,       0.000000E+00, 0.000000E+00
> OBJ4,     ADIABATIC_H,       0.000000E+00, 0.000000E+00
STOP
```

Appendices B
The Ground code for the MSSS fluence rate distribution model.

```
c<html><body><pre><strong><!-- -->
C.... FILE NAME GROUND.FTN--------------------------------070201
      SUBROUTINE GROUND
      INCLUDE '/phoenics/d_includ/satear'
      INCLUDE '/phoenics/d_includ/grdloc'
      INCLUDE '/phoenics/d_includ/satgrd'
      INCLUDE '/phoenics/d_includ/grdear'
      INCLUDE '/phoenics/d_includ/grdbfc'

COMMON/GENI/NXNY,IGFIL1(8),NFM,IGF(21),IPRL,IBTAU,ILTLS,IGFIL(15),
     1
ITEM1,ITEM2,ISPH1,ISPH2,ICON1,ICON2,IPRPS,IRADX,IRADY,IRADZ,IVFOL
      COMMON/DRHODP/ITEMP,IDEN/DVMOD/IDVCGR
CXXXXXXXXXXXXXXXXXXXXXXXXXXXXXXXXXXXXXXXX              USER
SECTION STARTS:
C
C 1   Set dimensions of data-for-GROUND arrays here. WARNING: the
C      corresponding arrays in the MAIN program of the satellite
C      and EARTH must have the same dimensions.
      PARAMETER (NLG=100, NIG=200, NRG=200, NCG=100)
C

COMMON/LGRND/LG(NLG)/IGRND/IG(NIG)/RGRND/RG(NRG)/CGRND/CG(NCG
)
      LOGICAL LG
      CHARACTER*4 CG
C
C 2   User dimensions own arrays here, for example:
C      DIMENSION GUH(10,10),GUC(10,10),GUX(10,10),GUZ(10)
C
C 3   User places his data statements here, for example:
C      DATA NXDIM,NYDIM/10,10/
C
C 4   Insert own coding below as desired, guided by GREX examples.
C      Note that the satellite-to-GREX special data in the labelled
C      COMMONs /RSG/, /ISG/, /LSG/ and /CSG/ can be included and
C      used below but the user must check GREX for any conflicting
C      uses. The same comment applies to the EARTH-spare working
```

```
C         arrays EASP1, EASP2,....EASP20. In addition to the EASPs,
C         there are 10 GRound-earth SPare arrays, GRSP1,...,GRSP10,
C         supplied solely for the user, which are not used by GREX. If
C         the call to GREX has been deactivated then all of the arrays
C         may be used without reservation.
C
c*******************************************************************
c
          IXL=IABS(IXL)
          IF(IGR.EQ.13) GO TO 13
          IF(IGR.EQ.19) GO TO 19
          GO TO (1,2,3,4,5,6,25,8,9,10,11,12,13,14,25,25,25,25,19,20,25,
         121,23,24),IGR
     25 CONTINUE
          RETURN
C*******************************************************************
C
C--- GROUP 1. Run title and other preliminaries
C
       1 GO TO (1001,1002,1003),ISC
C
  1001 CONTINUE
            CALL MAKE(XG2D    )
            CALL MAKE(YG2D    )
C
C     * -----------GROUP 1    SECTION    3 --------------------------
C---- Use this group to create storage via MAKE, GXMAKE etc which it is
C         essential to dump to PHI (or PHIDA) for restarts
C         User may here change message transmitted to the VDU screen
          IF(.NOT.NULLPR.AND.IDVCGR.EQ.0)
         1    CALL WRYT40('GROUND file is GROUND.F      of:       070201 ')
C
          RETURN
C     * -----------GROUP 1    SECTION    3 --------------------------
C---- Use this group to create storage via GXMAKE which it is not
C         necessary to dump to PHI (or PHIDA) for restarts
C
  1003 CONTINUE
          GO TO 25
  1002 CONTINUE
          RETURN
```

```
C***********************************************************************
C
C--- GROUP 2. Transience; time-step specification
C
      2 CONTINUE
        RETURN
C***********************************************************************
C
C--- GROUP 3. X-direction grid specification
C
      3 CONTINUE
        RETURN
C***********************************************************************
C
C--- GROUP 4. Y-direction grid specification
C
      4 CONTINUE
        RETURN
C***********************************************************************
C
C--- GROUP 5. Z-direction grid specification
C
      5 CONTINUE
        RETURN
C***********************************************************************
C
C--- GROUP 6. Body-fitted coordinates or grid distortion
C
      6 CONTINUE
        RETURN
C***********************************************************************
C     * Make changes for this group only in group 19.
C--- GROUP 7. Variables stored, solved & named
C***********************************************************************
C
C--- GROUP 8. Terms (in differential equations) & devices
C
      8 GO TO (81,82,83,84,85,86,87,88,89,810,811,812,813,814,815,816)
        1,ISC
     81 CONTINUE
C     * ------------------ SECTION    1 -------------------------
```

```
C       For U1AD.LE.GRND--- phase 1 additional velocity. Index VELAD
          RETURN
     82 CONTINUE
C     * ------------------- SECTION    2 --------------------------
C       For U2AD.LE.GRND--- phase 2 additional velocity. Index VELAD
          RETURN
     83 CONTINUE
C     * ------------------- SECTION    3 --------------------------
C       For V1AD.LE.GRND--- phase 1 additional velocity. Index VELAD
          RETURN
     84 CONTINUE
C     * ------------------- SECTION    4 --------------------------
C       For V2AD.LE.GRND--- phase 2 additional velocity. Index VELAD
          RETURN
     85 CONTINUE
C     * ------------------- SECTION    5 --------------------------
C       For W1AD.LE.GRND--- phase 1 additional velocity. Index VELAD
          RETURN
     86 CONTINUE
C     * ------------------- SECTION    6 --------------------------
C       For W2AD.LE.GRND--- phase 2 additional velocity. Index VELAD
          RETURN
     87 CONTINUE
C     * ------------------- SECTION 7 ---- Volumetric source for gala
          RETURN
     88 CONTINUE
C     * ------------------- SECTION 8 ---- Convection fluxes
C--- Entered when UCONV =.TRUE.; block-location indices are:
C       LD11 for east and north (accessible at the same time),
C       LD12 for west and south (accessible at the same time),
C       LD2    for high (which becomes low for the next slab).
C       User should provide INDVAR and NDIREC IF's as appropriate.
          RETURN
     89 CONTINUE
C     * ------------------- SECTION 9 ---- Diffusion coefficients
C--- Entered when UDIFF =.TRUE.; block-location indices are LAE
C       for east, LAW for west, LAN for north, LAS for
C       south, LD11 for high, and LD11 for low.
C       User should provide INDVAR and NDIREC IF's as above.
C       EARTH will apply the DIFCUT and GP12 modifications after the user
C       has made his settings.
```

```
C
         RETURN
  810 CONTINUE
C     * ------------------- SECTION 10 --- Convection neighbours
         RETURN
  811 CONTINUE
C     * ------------------- SECTION 11 --- Diffusion neighbours
         RETURN
  812 CONTINUE
C     * ------------------- SECTION 12 --- Linearised sources
         RETURN
  813 CONTINUE
C     * ------------------- SECTION 13 --- Correction coefficients
         RETURN
  814 CONTINUE
C     * ------------------- SECTION 14 --- User's own solver
         RETURN
  815 CONTINUE
C     * ------------------- SECTION 15 --- Change solution
         RETURN
  816 CONTINUE
C     * ------------------- SECTION 16 --- Change DVEL/DPs
         RETURN
C
C     * See the equivalent section in GREX for the indices to be
C       used in sections 7 - 16
C
C     * Make all other group-8 changes in GROUP 19.
C*************************************************************
C
C--- GROUP 9. Properties of the medium (or media)
C
C     The sections in this group are arranged sequentially in their
C     order of calling from EARTH. Thus, as can be seen from below,
C     the temperature sections (10 and 11) precede the density
C     sections (1 and 3); so, density formulae can refer to
C     temperature stores already set.
      9 GO TO (91,92,93,94,95,96,97,98,99,900,901,902,903,904,905),ISC
C*************************************************************
  900 CONTINUE
C     * ------------------- SECTION 10 --------------------------
```

```
C       For TMP1.LE.GRND--------- phase-1 temperature Index TEMP1
        RETURN
  901 CONTINUE
C     * ------------------- SECTION 11 --------------------------
C       For TMP2.LE.GRND--------- phase-2 temperature Index TEMP2
        RETURN
  902 CONTINUE
C     * ------------------- SECTION 12 --------------------------
C       For EL1.LE.GRND---------- phase-1 length scale Index LEN1
        RETURN
  903 CONTINUE
C     * ------------------- SECTION 13 --------------------------
C       For EL2.LE.GRND---------- phase-2 length scale Index LEN2
        RETURN
  904 CONTINUE
C     * ------------------- SECTION 14 --------------------------
C       For SOLVE(TEM1)-------- phase-1 specific heat
        RETURN
  905 CONTINUE
C     * ------------------- SECTION 15 --------------------------
C       For SOLVE(TEM2)-------- phase-2 specific heat
        RETURN
   91 CONTINUE
C     * ------------------- SECTION    1 --------------------------
C       For RHO1.LE.GRND--- density for phase 1            Index DEN1
        RETURN
   92 CONTINUE
C     * ------------------- SECTION    2 --------------------------
C       For DRH1DP.LE.GRND--- D(LN(DEN))/DP for phase 1
C                                                          Index D1DP
        RETURN
   93 CONTINUE
C     * ------------------- SECTION    3 --------------------------
C       For RHO2.LE.GRND--- density for phase 2            Index DEN2
        RETURN
   94 CONTINUE
C     * ------------------- SECTION    4 --------------------------
C       For DRH2DP.LE.GRND--- D(LN(DEN))/DP for phase 2
C                                                          Index D2DP
        RETURN
   95 CONTINUE
```

```
C     * ------------------- SECTION    5 --------------------------
C       For ENUT.LE.GRND--- reference turbulent kinematic viscosity
C                                                                Index VIST
         RETURN
     96 CONTINUE
C     * ------------------- SECTION    6 --------------------------
C       For ENUL.LE.GRND--- reference laminar kinematic viscosity
C                                                                Index VISL
         RETURN
     97 CONTINUE
C     * ------------------- SECTION    7 --------------------------
C       For PRNDTL( ).LE.GRND--- laminar PRANDTL nos., or diffusivity
C                                                                Index LAMPR
         RETURN
     98 CONTINUE
C     * ------------------- SECTION    8 --------------------------
C       For PHINT( ).LE.GRND--- interface value of first phase
C                                                                Index FII1
         RETURN
     99 CONTINUE
C     * ------------------- SECTION    9 --------------------------
C       For PHINT( ).LE.GRND--- interface value of second phase
C                                                                Index FII2
         RETURN
C***********************************************************************
C
C--- GROUP 10. Inter-phase-transfer processes and properties
C
     10 GO TO (101,102,103,104,105),ISC
    101 CONTINUE
C     * ------------------- SECTION    1 --------------------------
C       For CFIPS.LE.GRND--- inter-phase friction coeff.
C                                                                Index INTFRC
         RETURN
    102 CONTINUE
C     * ------------------- SECTION    2 --------------------------
C       For CMDOT.EQ.GRND- inter-phase mass transfer    Index INTMDT
         RETURN
    103 CONTINUE
C     * ------------------- SECTION    3 --------------------------
C       For CINT( ).EQ.GRND--- phase1-to-interface transfer coefficients
```

```
C                                                       Index COI1
        RETURN
  104 CONTINUE
C     * ------------------- SECTION    4 --------------------------
C       For CINT( ).EQ.GRND--- phase2-to-interface transfer coefficients
C                                                       Index COI2
        RETURN
  105 CONTINUE
C     * ------------------- SECTION    5 --------------------------
C       For CVM.EQ.GRND--- virtual mass coefficient
C                                                       Index LD12
        RETURN
C*****************************************************************
C
C--- GROUP 11. Initialization of variable or porosity fields
C                                                       Index VAL
    11 CONTINUE
        RETURN
C*****************************************************************
C
C--- GROUP 12. Convection and diffusion adjustments
C
    12 CONTINUE
        RETURN
C*****************************************************************
C
C--- GROUP 13. Boundary conditions and special sources
C                                           Index for Coefficient - CO
C                                           Index for Value           - VAL
    13 CONTINUE
        GO TO (130,131,132,133,134,135,136,137,138,139,1310,
       11311,1312,1313,1314,1315,1316,1317,1318,1319,1320,1321),ISC
  130 CONTINUE
C------------------- SECTION    1 ------------ coefficient = GRND
        RETURN
  131 CONTINUE
C------------------- SECTION    2 ------------ coefficient = GRND1
        RETURN
  132 CONTINUE
C------------------- SECTION    3 ------------ coefficient = GRND2
        RETURN
```

```
   133 CONTINUE
C------------------- SECTION    4 ------------ coefficient = GRND3
          RETURN
   134 CONTINUE
C------------------- SECTION    5 ------------ coefficient = GRND4
          RETURN
   135 CONTINUE
C------------------- SECTION    6 ------------ coefficient = GRND5
          RETURN
   136 CONTINUE
C------------------- SECTION    7 ------------ coefficient = GRND6
          RETURN
   137 CONTINUE
C------------------- SECTION    8 ------------ coefficient = GRND7
          RETURN
   138 CONTINUE
C------------------- SECTION    9 ------------ coefficient = GRND8
          RETURN
   139 CONTINUE
C------------------- SECTION 10 ------------ coefficient = GRND9
          RETURN
  1310 CONTINUE
C------------------- SECTION 11 ------------ coefficient = GRND10
          RETURN
  1311 CONTINUE
C------------------- SECTION 12 ------------------- value = GRND
C           Source name: SORC45
          IF(INDVAR.EQ.INAME('C1        ').AND.NPATCH.EQ.'IRR1        ') THEN
            LFVAL =L0F(VAL)
            LFRR1 =L0F(INAME('RR1      '))
            LFHH1 =L0F(INAME('HH1      '))
            DO 13845 IX=IXF         ,IXL
              IADD=NY*(IX-1)
            DO 13845 IY=IYF         ,IYL
              I=IY+IADD
            L0RR1 =LFRR1 +I
            L0HH1 =LFHH1 +I
            F(LFVAL+I)=0.0
            DO 39907 J=1,1000
      AN1=RG(12)
      AN2=RG(13)
```

```
      AN3=RG(82)
      AD1=ABS(F(L0RR1)-RG(11))
      AD2=RG(83)
      AD3=RG(11)-RG(83)
      AD=ABS(RG(10)/2.-F(L0HH1)-(2*J-1)*RG(10)/2000.)
      ACF=RG(19)
         ANG2=CALANG(AN1,AN2,AN3,AD1,AD2,AD3,AD,ACF)
      ANG1=ASIN(SIN(ANG2)*AN2/AN1)
      ANG3=ASIN(SIN(ANG2)*AN2/AN3)
            AH1P=ABS(AD1*TAN(ASIN(AN3/AN1*SIN(ANG3+0.01))))
            AH2P=ABS(AD2*TAN(ASIN(AN3/AN2*SIN(ANG3+0.01))))
            AH3P=ABS(AD3*TAN(ANG3+0.01))
            AH1=ABS(AD1*TAN(ANG1))
            AH2=ABS(AD2*TAN(ANG2))
            AH3=ABS(AD3*TAN(ANG3))

FOCF=(0.01*(AD1/COS(ANG1)+AD2/COS(ANG2)+AD3/COS(ANG3))/(AH1P+AH2
P
        l+AH3P-AH1-AH2-AH3)/COS(ANG1))**2.
      DO 49907 K=1,1
      ATR1=RG(K+20)
      ATR2=RG(K+84)
      APF=RG(K+40)
      AGF=RG(K+60)
         ARAD=CALRAD(AD1,AD2,AD3,ANG1,ANG2,ANG3,ATR1,ATR2,APF,AGF)
         F(LFVAL+I)=F(LFVAL+I)+cos(ang3)*ARAD*RG(14)*RG(18)/1000./4./3.1416
        l*FOCF

49907 CONTINUE
39907 CONTINUE
13845 CONTINUE
            ENDIF
            RETURN
  1312 CONTINUE
C------------------- SECTION 13 ------------------- value = GRND1
            RETURN
  1313 CONTINUE
C------------------- SECTION 14 ------------------- value = GRND2
            RETURN
  1314 CONTINUE
C------------------- SECTION 15 ------------------- value = GRND3
```

```
          RETURN
 1315 CONTINUE
C------------------- SECTION 16 ------------------- value = GRND4
          RETURN
 1316 CONTINUE
C------------------- SECTION 17 ------------------- value = GRND5
          RETURN
 1317 CONTINUE
C------------------- SECTION 18 ------------------- value = GRND6
          RETURN
 1318 CONTINUE
C------------------- SECTION 19 ------------------- value = GRND7
          RETURN
 1319 CONTINUE
C------------------- SECTION 20 ------------------- value = GRND8
          RETURN
 1320 CONTINUE
C------------------- SECTION 21 ------------------- value = GRND9
          RETURN
 1321 CONTINUE
C------------------- SECTION 22 ------------------- value = GRND10
          RETURN
C*************************************************************
C
C--- GROUP 14. Downstream pressure for PARAB=.TRUE.
C
    14 CONTINUE
          RETURN
C*************************************************************
C* Make changes to data for GROUPS 15, 16, 17, 18    GROUP 19.
C*************************************************************
C
C--- GROUP 19. Special calls to GROUND from EARTH
C
    19 GO TO (191,192,193,194,195,196,197,198,199,1910,1911),ISC
  191 CONTINUE
C     * ------------------- SECTION 1 ---- Start of time step.
          RETURN
  192 CONTINUE
C     * ------------------- SECTION 2 ---- Start of sweep.
          RETURN
```

```
  193 CONTINUE
C     * -------------------- SECTION 3 ---- Start of iz slab.
        RETURN
  194 CONTINUE
C     * -------------------- SECTION 4 ---- Start of iterations over slab.
        RETURN
 1911 CONTINUE
C     * -------------------- SECTION 11---- After calculation of convection
C                                          fluxes for scalars, and of volume
C                                          fractions, but before calculation of
C                                          scalars or velocities
        RETURN
  199 CONTINUE
C     * -------------------- SECTION 9 ---- Start of solution sequence for
C                                                                    a variable
C         Special calls name: SC10
C         Special calls name: SC1001
        IF(ISTEP.GE.1            .AND.ISTEP.LE.LSTEP     ) THEN
        IF(IZ.GE.1             .AND.IZ.LE.NZ           ) THEN
         LFRR1    =L0F(INAME('RR1     '))
         LFXG2D=L0F(XG2D    )
         LFYG2D=L0F(YG2D    )
         DO 19901 IX=1            ,NX
          IADD=NY*(IX-1)
         DO 19901 IY=1            ,NY
          I=IY+IADD
         L0RR1 =LFRR1 +I
         L0XG2D=LFXG2D+I
         L0YG2D=LFYG2D+I
19901 F(L0RR1     )=((F(L0XG2D)-RG(1))**2.+(F(L0YG2D)-RG(2))**2
       1.)**0.5+TINY
        ENDIF
        ENDIF
C         Special calls name: SC10
C         Special calls name: SC1005
        IF(ISTEP.GE.1            .AND.ISTEP.LE.LSTEP     ) THEN
        IF(IZ.GE.1             .AND.IZ.LE.NZ           ) THEN
         LFHH1    =L0F(INAME('HH1     '))
         L0ZGNZ=L0F(ZGNZ    )+IZ
         DO 19905 IX=1            ,NX
          IADD=NY*(IX-1)
```

```
            DO 19905 IY=1             ,NY
              I=IY+IADD
            L0HH1 =LFHH1 +I
19905 F(L0HH1      )=-(F(L0ZGNZ)-RG(9)+TINY)
          ENDIF
          ENDIF
          RETURN
  1910 CONTINUE
C     * ------------------- SECTION 10---- Finish of solution sequence for
C                                                                        a variable
          RETURN
   195 CONTINUE
C     * ------------------- SECTION 5 ---- Finish of iterations over slab.
          RETURN
   196 CONTINUE
C     * ------------------- SECTION 6 ---- Finish of iz slab.
          RETURN
   197 CONTINUE
C     * ------------------- SECTION 7 ---- Finish of sweep.
          RETURN
   198 CONTINUE
C     * ------------------- SECTION 8 ---- Finish of time step.
C
          RETURN
C*************************************************************
C
C--- GROUP 20. Preliminary print-out
C
     20 CONTINUE
          RETURN
C*************************************************************
C--- GROUP 21. Special print-out to screen
     21 CONTINUE
          GO TO 25
C*************************************************************
C* Make changes to data for GROUP 22 only in GROUP 19.
C*************************************************************
C
C--- GROUP 23. Field print-out and plot control
     23 CONTINUE
          RETURN
```

```
C*************************************************************
C
C--- GROUP 24. Dumps for restarts
C
     24 CONTINUE
          CONTAINS
      FUNCTION CALANG(N1,N2,N3,D1,D2,D3,D,CF) RESULT(CALANG_RESULT)
          REAL N1,N2,N3,D1,D2,D3,D,CF,CALANG_RESULT
      REAL ANG1,ANG2,ANG3
      ANG1=0.0
      ANG2=ASIN(N3/N2)
      ANG3=(ANG1+ANG2)/2.0
30650 IF (D1*TAN(ASIN(SIN(ANG3)*N2/N1))+D2*TAN(ANG3)+D3*TAN(ASIN(
        C SIN(ANG3)*N2/N3))-D.GT.CF) THEN
        ANG2=ANG3
        ANG3=(ANG1+ANG2)/2.0
      GOTO 30650
        ELSE
IF(D1*TAN(ASIN(SIN(ANG3)*N2/N1))+D2*TAN(ANG3)+D3*TAN(ASIN(
        C SIN(ANG3)*N2/N3))-D.LT.-CF) THEN
        ANG1=ANG3
        ANG3=(ANG1+ANG2)/2.0
      GOTO 30650
      END IF
      CALANG_RESULT=ANG3
      END FUNCTION CALANG

      FUNCTION CALRAD(D1,D2,D3,ANG1,ANG2,ANG3,TR1,TR2,PF,GF)
        C RESULT(CALRAD_RESULT)
      REAL D1,D2,D3,ANG1,ANG2,ANG3,TR1,TR2,PF,GF
      REAL CALRAD_RESULT
      CALRAD_RESULT=TR1**(100*D1/COS(ANG1))*TR2**(100*D2/COS(ANG2))/
        C (D1/COS(ANG1)+D2/COS(ANG2)+D3/COS(ANG3))**2.*PF*GF
          END FUNCTION CALRAD
          END
c</pre></strong></body></html>
```

Appendices C

Other Q1 files and ground codes for the fluence rate distribution simulation and turbulence modeling

Following Q1 and ground codes were used for the fluence rate distribution and turbulence modeling. They are available upon request.

1. Q1 file and ground code for the LSI combined with the 3 points attenuation factor.

   (3PT-LSI-Focus-Cos-Reflection.Q1)

   (3PT-LSI-Focus-Cos-Reflection-Ground.TXT)

2. Q1 file and ground code for the LSI combined with the 5 points attenuation factor.

   (5PT-LSI-Focus-Cos-Reflection.Q1)

   (5PT-LSI-Focus-Cos-Reflection-Ground.TXT)

3. Q1 file and ground code for the LSI combined with the 10 points attenuation factor.

   (10PT-LSI-Focus-Cos-Reflection.Q1)

   (10PT-LSI-Focus-Cos-Reflection-Ground.TXT)

4. Q1 file and ground code for the RAD-LSI combined with the 5 points attenuation factor.

   (RAD-LSI-5PT.Q1) (RAD-LSI-5PT-Ground.TXT)

5. Q1 file and ground code for the View factor combined with 5 points attenuation factor.

   (View-Factor-5PT.Q1) (View-Factor-5PT-Ground.TXT)

6. Q1 file for the LSI model. (LSI.Q1)

7. Q1 and GHIS files for the STD k-ε turbulence model.

(STD-ke.Q1) (STD-ke.GHIS)

8. Q1 and GHIS files for the k-ε RNG turbulence model.

(ke-RNG.Q1) (ke-RNG.GHIS)

9. Q1 and GHIS files for the k-ω (88) turbulence model.

(kw-88.Q1) (kw-88.GHIS)

10. Q1 file, GHIS file, and the ground code for the k-ω (98) turbulence model.

(kw-98.Q1) (kw-98.GHIS) (kw-98-Ground.TXT)

11. Q1 and GHIS files for the RSTM turbulence model.

(RSTM.Q1) (RSTM.GHIS)

12. Q1 file, GHIS file, and the ground code for the TFM.

(TFM.Q1) (TFM.GHIS) (TFM-Ground.TXT)

13. Input files for UVCalc_3D for low and high lamp power conditions.

(Reactor-File-Low-Power.TXT)

(Reactor-File-High-Power.TXT)